

Electronic Thesis and Dissertation Repository

9-7-2018 3:00 PM

Synthesis and Characterization of Alkynyl-Substituted Boron Formazanate Dyes

Alex Van Belois
The University of Western Ontario

Supervisor
Gilroy, Joe B.
The University of Western Ontario Joint Supervisor
Workentin, Mark S.
The University of Western Ontario

Graduate Program in Chemistry
A thesis submitted in partial fulfillment of the requirements for the degree in Master of Science
© Alex Van Belois 2018

Follow this and additional works at: <https://ir.lib.uwo.ca/etd>

 Part of the [Materials Chemistry Commons](#), and the [Organic Chemistry Commons](#)

Recommended Citation

Van Belois, Alex, "Synthesis and Characterization of Alkynyl-Substituted Boron Formazanate Dyes" (2018).
Electronic Thesis and Dissertation Repository. 5658.
<https://ir.lib.uwo.ca/etd/5658>

This Dissertation/Thesis is brought to you for free and open access by Scholarship@Western. It has been accepted for inclusion in Electronic Thesis and Dissertation Repository by an authorized administrator of Scholarship@Western. For more information, please contact wlsadmin@uwo.ca.

Abstract

This thesis outlines the synthesis and characterization of the first alkynyl-substituted boron formazanate complexes and explores the electronic and structural changes that occur in these systems as a result of chemical modification at the boron centre. An alkynyl-substituted complex appended with a redox-active handle is also described, and the chemical reduction and oxidation of this system is explored. Finally, a model reaction is examined as a proof of concept toward the post-synthetic modification of these boron formazanate systems through copper(I)-assisted alkyne-azide cycloaddition chemistry. Exploiting chemistry at the boron centre opens up new possibilities toward incorporating function onto the boron formazanate scaffold.

Keywords

Formazanate Ligands, Copper(I)-Assisted Alkyne-Azide Cycloaddition, Absorption Spectroscopy, Redox Chemistry, Dye Chemistry

Co-Authorship Statement

The work described in this thesis contains contributions from the author as well as Ryan Maar and Profs. Mark S. Workentin and Joe B. Gilroy. The contributions of each are described below.

Chapter 1 was written by the author and edited by Profs. Mark S. Workentin and Joe B. Gilroy.

Chapter 2 describes the synthesis of a family of alkynyl-substituted boron formazanate complexes that were completed by the author. All X-ray crystallographic data described was collected and refined by Ryan Maar. The chapter was written by the author and edited by Profs. Mark S. Workentin and Joe B. Gilroy.

Chapter 3 describes post-synthetic modification of alkynyl-substituted complexes, and a redox-active complex and its radical derivatives that were completed by the author. All X-ray crystallographic data described was collected and refined by Ryan Maar. The chapter was written by the author and edited by Prof. Mark S. Workentin and Prof. Joe B. Gilroy.

Chapter 4 was written by the author and edited by Profs. Mark S. Workentin and Joe B. Gilroy.

Acknowledgements

First and foremost, I would like to thank both Prof. Joe Gilroy and Prof. Mark Workentin for their incredible mentorship and support over the past two years. I learned an incredible amount from you both and truly appreciate the time you spent helping me to become a better presenter, writer and chemist. Your enthusiasm, patience and dedication made this an incredibly enjoyable experience. Thank you both for giving me the opportunity to work as a member of your groups.

Secondly I would like to thank all the past and present graduate students in both the Gilroy and Workentin groups. From the Gilroy group, I want to thank Ryan for his time, knowledge and patience showing me the ropes and giving me advice when things didn't go smoothly. Thanks to Jas and Daniela for the endless entertainment you two provide as you bicker like an old, married couple. Sam and Steph, thanks for always making it fun to come into lab, even when things weren't going well. From the Workentin group, I want to thank Wilson, Praveen, Tommy, Vaish, Raj, Justin, Kyle and honorary member Jeff for always keeping me entertained and having a good time over coffee and cards. I can safely say I wouldn't have made it through grad school without you all. I would also like to thank the rest of the graduate students I had the pleasure of working and spending time with, especially our ultimate Frisbee teams.

I want to express my gratitude to the entire faculty of Chemistry, whom over the course of my undergraduate and graduate studies I've had the pleasure of learning from. Thank you to the support staff – Mat Willans, Doug Hairsine, Yves Rambour, Aneta Borecki, Paul Boyle, Monica Chirigel, Marylou Hart and Darlene McDonald for always being there and willing to help me.

Thank you to my committee – Prof. Mike Kerr, Prof. François Lagugné-Labarthe and Prof. Ilka Heinemann for taking the time to read my thesis.

Finally, I want to thank my family. To my parents, I want to thank you for your immense support over the years and all the sacrifices you've made to get me where I am today. I'm deeply grateful for your encouragement, advice and for always being there when I needed you. I could not have done this without you. To my siblings, thank you for providing me with endless entertainment. To my friends and family, thank you for the friendship and support throughout the years. I love you all.

Table of Contents

| | |
|--|------|
| Abstract | i |
| Keywords | i |
| Co-Authorship Statement..... | ii |
| Acknowledgements..... | iii |
| Table of Contents..... | v |
| List of Tables | vii |
| List of Figures | viii |
| List of Schemes..... | x |
| List of Appendices | xii |
| List of Abbreviations | xiii |
| Chapter 1 | 1 |
| 1.1 Introduction..... | 1 |
| 1.2 Boron complexes of β -diketiminates | 1 |
| 1.3 Boron Complexes of Anilido-imines & Anilido-pyridines | 3 |
| 1.4 Boron dipyrrromethenes (BODIPYs)..... | 7 |
| 1.5 BODIPY Derivatization via Fluorine Displacement | 11 |
| 1.5.1 <i>O</i> -BODIPY | 12 |
| 1.5.2 <i>E</i> -BODIPY..... | 14 |
| 1.6 Formazans & BF_2 Formazanate Complexes | 17 |
| 1.7 Scope of Thesis..... | 22 |
| 1.8 References..... | 23 |
| Chapter 2..... | 26 |
| 2.1 Introduction..... | 26 |
| 2.2 Results & Discussion | 28 |
| 2.2.1 Synthesis of Alkynyl-Substituted Boron Formazanate Complexes | 28 |
| 2.2.2 X-Ray Crystallography..... | 33 |
| 2.2.3 UV-Visible Absorption Spectroscopy | 34 |
| 2.2.4 Electrochemical Properties..... | 36 |
| 2.3 Conclusions..... | 39 |
| 2.4 Experimental | 40 |

| | |
|---|----|
| 2.4.1 General Considerations | 40 |
| 2.4.2 X-ray Crystallography Methods | 40 |
| 2.4.3 Electrochemical Methods | 43 |
| 2.4.4 Synthetic Procedures | 43 |
| 2.5 References..... | 47 |
| Chapter 3..... | 49 |
| 3.1 Introduction..... | 49 |
| 3.2 Results & Discussion..... | 51 |
| 3.2.1 Synthesis of a Redox-Active Alkynyl-Substituted Boron Formazante Complex | 51 |
| 3.2.2 X-ray Crystallography | 53 |
| 3.2.3 Electrochemical Properties..... | 55 |
| 3.2.4 Reduced & Oxidized Forms of Redox-Active Complex 3.5..... | 57 |
| 3.2.5 UV-Visible Absorption Spectroscopy..... | 59 |
| 3.2.6 Post-synthetic Functionalization via Cu(I)-Catalyzed Click Chemistry | 63 |
| 3.2.7 UV-Visible Absorption Spectroscopy..... | 67 |
| 3.3 Conclusions..... | 68 |
| 3.4 Experimental..... | 70 |
| 3.4.1 General Considerations | 70 |
| 3.4.2 X-ray Crystallography Methods | 71 |
| 3.4.3 Electrochemical Methods | 72 |
| 3.4.4 Electron Paramagnetic Resonance Spectroscopy | 73 |
| 3.4.5 Synthetic Procedures | 73 |
| 3.5 References..... | 78 |
| Chapter 4..... | 80 |
| 4.1 Conclusions..... | 80 |
| 4.2 Future Work..... | 84 |
| Appendices..... | 86 |
| Appendix A – Supporting Information for Chapter 2..... | 86 |
| Appendix B – Supporting Information for Chapter 3 | 92 |
| Curriculum Vitae | 97 |

List of Tables

| | |
|---|----|
| Table 2.1. IR stretches for the internal alkyne of compounds 2.8–2.10 | 32 |
| Table 2.2. Selected bond lengths (Å) and bond angles (°) of compounds 2.7 and 2.8 | 34 |
| Table 2.3. Spectroscopic properties of complexes 2.7–2.10 | 36 |
| Table 2.4. Summary of the electrochemical properties of compounds 2.7–2.10 . ^a | 37 |
| Table 2.5. X-ray diffraction data collection and refinement details for compounds 2.7 and 2.8 | 42 |
| Table 3.1. Selected bond lengths (Å) and angles (°) of compounds 2.7 , 2.8 and 3.5 | 55 |
| Table 3.2. Summary of the electrochemical properties of compounds 2.7 , 2.8 and 3.5 . ^a | 56 |
| Table 3.3. Spectroscopic properties of complexes 3.5 , 3.6 and 3.8 | 61 |
| Table 3.4. Spectroscopic properties of complexes 2.8 and 3.7 | 62 |
| Table 3.5. Spectroscopic properties of complexes 3.10 and 3.12 | 68 |
| Table 3.6. X-ray diffraction data collection and refinement details for compound 3.5 | 72 |

List of Figures

| | |
|--|----|
| Figure 2.1. ^1H NMR spectrum of compound 2.6 in CDCl_3 . | 30 |
| Figure 2.2. ^1H NMR spectrum of compound 2.7 in CDCl_3 . | 30 |
| Figure 2.3. ^{19}F (a) and ^{11}B (b) NMR spectra of compound 2.7 recorded in CDCl_3 . | 31 |
| Figure 2.4. IR spectra of compounds 2.8 (red), 2.9 (blue) and 2.10 (green). Black box indicates the internal alkyne stretch. | 32 |
| Figure 2.5. Top-view and side-view of the solid-state structures of a) 2.7 and b) 2.8 . Thermal ellipsoids are shown at 50% probability and hydrogen atoms are removed for clarity. Substituents at the boron centre in the side-view of b) have been converted to wireframe for clarity. | 34 |
| Figure 2.6. UV-Visible absorption spectra of compounds 2.7–2.10 recorded for degassed 10 μM toluene solutions. | 35 |
| Figure 2.7. Cyclic voltammograms of compounds 2.7 (black), 2.8 (red), 2.9 (blue) and 2.10 (green) recorded in dry, degassed CH_2Cl_2 containing ~ 1 mM analyte and 0.1 M $[\text{nBu}_4\text{N}][\text{PF}_6]$ as a supporting electrolyte at a scan rate of 250 mV s^{-1} . Arrow indicates the direction of scan. | 38 |
| Figure 3.1. IR Spectrum of complex 3.5 . Arrow indicates the internal alkyne stretch at 2188 cm^{-1} . | 52 |
| Figure 3.2. Side-view solid state structures of a) 2.7 , b) 2.8 . Top-view and side-view solid-state structures of c) 3.5 . Thermal ellipsoids are shown at 50% probability and hydrogen atoms are removed for clarity. Some substituents in b) and c) have been converted to wireframe for clarity. a) and b) have been reproduced from Chapter 2 for comparison. | 53 |
| Figure 3.3. Cyclic voltammograms of compounds 2.7 (blue), 2.8 (red), and 3.5 (green) recorded in dry, degassed CH_2Cl_2 containing ~ 1 mM analyte and 0.1 M $[\text{nBu}_4\text{N}][\text{PF}_6]$ as a supporting electrolyte at a scan rate of 250 mV s^{-1} . Arrows indicate the direction of scan. | 56 |
| Figure 3.4. UV-Visible absorption spectra of compounds 3.5 , 3.6 , and 3.8 recorded for degassed 10 μM CH_3CN solutions. | 60 |

| | |
|--|----|
| Figure 3.5. UV-Visible absorption spectra of compounds 2.8 and 3.7 recorded for degassed 10 μM CH_3CN solutions..... | 61 |
| Figure 3.6. EPR spectra of a) 3.6 and b) 3.7 in degassed THF at 298 K ($g = 2.0035$)..... | 62 |
| Figure 3.7. IR spectrum of compound 3.10 . Arrows indicate the terminal acetylene functionality at 3281 and 2060 cm^{-1} | 64 |
| Figure 3.8. ^1H NMR spectra of compounds 3.9 (top), 3.10 (middle) and 3.12 (bottom) in CDCl_3 . Red highlights on structures indicate protons of interest..... | 66 |
| Figure 3.9. IR spectra of compounds 3.10 (black), 3.11 (red) and 3.12 (blue)..... | 67 |
| Figure 3.10. UV-Visible absorption spectra of compounds 3.10 and 3.12 recorded for degassed 10 μM toluene solutions..... | 68 |
| Figure 4.1. Formazanate and boron formazanate complexes studied in Chapter 2..... | 81 |
| Figure 4.2. Ferrocene complexes studied in Chapter 3..... | 83 |

List of Schemes

| | |
|---|----|
| Scheme 1.1. Synthesis of functional boron diiminate complexes. Yields are indicated in brackets. ¹² | 2 |
| Scheme 1.2. Synthesis of boron-containing anilido-imine complexes. Yields are indicated in brackets. ¹⁷ | 4 |
| Scheme 1.3. Suzuki-Miyaura coupling for the synthesis of boron-containing anilido-pyridines. ¹⁸ | 5 |
| Scheme 1.4. Synthesis of boron-containing anilido-pyridines via Hartwig-Buchwald amination. ¹⁸ | 6 |
| Scheme 1.5. Synthesis of alkyl-substituted BODIPY complexes. ² | 9 |
| Scheme 1.6. Synthesis of a fluorescent pH-sensing BODIPY complex via Knoevenegal condensation. ² | 9 |
| Scheme 1.7. Synthesis of phenanthrene-fused BODIPY complexes. Yields indicated in brackets. ²³ | 11 |
| Scheme 1.8. Synthesis of O-BODIPYs. Overall yields indicated in brackets. ²⁹ | 12 |
| Scheme 1.9. Synthesis of O-BODIPYs. Overall yields indicated in brackets. ³¹ | 14 |
| Scheme 1.10. Synthesis of E-BODIPYs via lithiated terminal acetylenes. ²⁴ | 15 |
| Scheme 1.11. General synthesis of formazan ligands and resulting BF ₂ complexes. ³⁹ | 18 |
| Scheme 1.12. Synthesis of 3-cyano BF ₂ formazanate complexes. ³⁸ | 20 |
| Scheme 2.1. Synthesis of tri-p-tolyl BF ₂ formazanate complex 2.7 | 29 |
| Scheme 2.2. Synthesis of alkynyl-substituted boron formazanate complexes 2.8–2.10 | 31 |
| Scheme 2.3. Stepwise electrochemical reduction of neutral boron-containing formazanate complexes (2.13) to the corresponding radical anion (2.12) and radical dianion (2.11) oxidation of neutral boron-containing formazanate complexes (2.13) to the corresponding radical cation (2.14). | 37 |
| Scheme 3.1. Synthesis of redox-active boron formazanate complex 3.5 . Yield is indicated in brackets. | 52 |

| | |
|---|----|
| Scheme 3.2. Synthesis of the reduced ferrocene-containing boron formazanate complex 3.6 | 58 |
| Scheme 3.3. Synthesis of the reduced phenylacetylene complex 3.7 | 58 |
| Scheme 3.4. Synthesis of the oxidized ferrocene-containing boron formazanate complex 3.8 | 59 |
| Scheme 3.5. Synthesis of boron acetylene complex 3.10 | 63 |
| Scheme 3.6. CuAAC reaction with benzyl azide..... | 64 |
| Scheme 4.1. CuAAC chemistry studied in Chapter 3..... | 84 |
| Scheme 4.2. Proposed Knoevenegal condensation and CuAAC toward the synthesis of multifunctional ethynyl-substituted boron formazanate complexes..... | 85 |

List of Appendices

| | |
|--|----|
| Appendix A – Supporting Information for Chapter 2..... | 86 |
| Appendix B – Supporting Information for Chapter 3..... | 92 |

List of Abbreviations

| | |
|-------------------------|--|
| ° | degree |
| °C | degrees Celsius |
| A | absorbance |
| Å | angstrom |
| a.u. | arbitrary units |
| Ar | aryl |
| ATR | attenuated total reflectance |
| AlCl ₃ | aluminum chloride |
| BASi | Bioanalytical Systems Inc. |
| BODIPY | boron dipyrromethene |
| CCDC | Cambridge crystallographic data centre |
| CIEE | crystallization-induced emission enhancement |
| cm ⁻¹ | wavenumber |
| CuAAC | copper (I)-assisted alkyne-azide cycloaddition |
| CV | cyclic voltammogram |
| d | doublet |
| DME | dimethoxyethane |
| DMF | dimethylformamide |
| dppf | bis(diphenylphosphino)ferrocene |
| E°_{Fc} | ferrocene oxidation potential |
| EI | electron-impact ionization |

| | |
|---------------------------|--|
| E°_{ox1} | first oxidation potential |
| EPR | electron paramagnetic resonance |
| E°_{red1} | first reduction potential |
| E°_{red2} | second reduction potential |
| ESI | electrospray ionization |
| Et | ethyl |
| Et ₂ O | diethyl ether |
| EtOAc | ethyl acetate |
| EtOH | ethanol |
| Fc | Ferrocene |
| Fc ⁺ | Ferrocenium |
| FT-IR | Fourier transform infra-red spectroscopy |
| g | gram |
| h | hour(s) |
| Hz | hertz |
| IR | infrared |
| J | NMR coupling constant |
| K | degrees Kelvin |
| LDA | lithium diisopropylamide |
| M | molar |
| m | multiplet |
| max | maximum |

| | |
|------------------------------------|--|
| Me | methyl |
| MeCN | acetonitrile |
| MeOH | methanol |
| mg | milligram |
| MHz | megahertz |
| min | minute/minutes |
| mL | milliliter |
| mM | millimolar |
| mmol | millimoles |
| mol | moles |
| mV | millivolt |
| <i>n</i> -BuLi | <i>n</i> -butyllithium |
| Na ₂ CO ₃ | sodium carbonate |
| NaHCO ₃ | sodium bicarbonate |
| NEt ₃ | triethyl amine |
| nm | nanometer |
| NMR | nuclear magnetic resonance |
| OAc | acetate |
| OMe | methoxy |
| <i>p</i> | para |
| Pd ₂ (dba) ₃ | tris(dibenzylideneacetone)dipalladium(0) |
| Pd(PCy) ₃ | bis(tricyclohexylphosphine)palladium(0) |

| | |
|------------------------------------|---|
| Pd(PPh ₃) ₄ | tetrakis(triphenylphosphine)palladium(0) |
| Ph | phenyl |
| PMDETA | <i>N, N, N', N'', N'''</i> -pentamethyldiethylenetriamine |
| ppm | parts per million |
| <i>p</i> -tol | <i>para</i> -tolyl |
| π | pi |
| ppm | parts per million |
| Φ _F | fluorescence quantum yield |
| q | quartet |
| TFA | trifluoroacetic acid |
| r.t. | room temperature |
| s | singlet |
| t | triplet |
| <i>t</i> -BuOK | potassium <i>tert</i> -butoxide |
| THF | tetrahydrofuran |
| UV | ultraviolet |
| UV-Vis | ultraviolet-visible |
| V | volts |
| <i>x</i> | Cartesian axis |
| XRD | X-ray diffraction |
| <i>y</i> | Cartesian axis |
| <i>z</i> | Cartesian axis |

| | |
|------------------------|--|
| α | crystallographic lattice constant, torsional angle |
| β | crystallographic lattice constant, torsional angle |
| γ | crystallographic lattice constant, torsional angle |
| δ | chemical shift, partial charge |
| ϵ | molar absorptivity |
| θ | theta (range for crystallographic data collection) |
| λ | wavelength |
| λ_{max} | wavelength of maximum absorption |
| λ_{em} | wavelength of maximum emission |

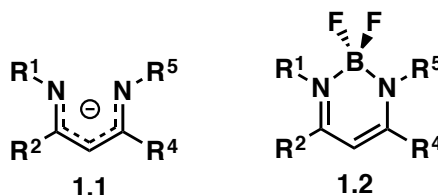
Chapter 1

1.1 Introduction

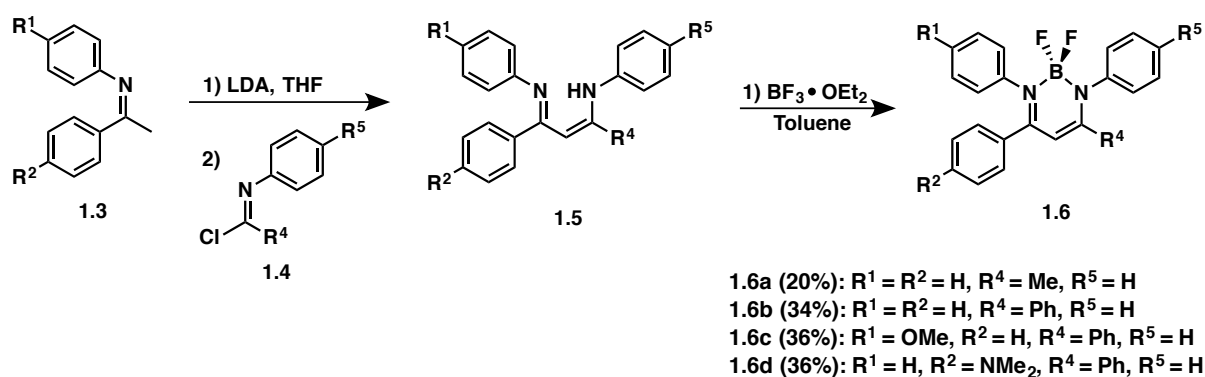
Over the past two decades, boron-containing complexes of chelating *N*-donor ligands have garnered significant interest as functional materials and have been extensively studied as a result of their unique properties, including high fluorescence quantum yields, high molar extinction coefficients, narrow absorption/emission bands and interesting redox chemistry.¹ Their desirable properties have accelerated the use of these materials in a wide array of applications, including pH sensing,^{2,3} fluorescence imaging,^{4,5,6} biological labeling^{7,8} and photodynamic therapy.⁹ The incorporation of 4-coordinate boron is a common occurrence throughout these examples, as it rigidifies the ligand systems, therefore reducing the non-radiative vibrational and rotational energy loss and increasing emission values. Numerous chelating *N*-donor ligands have been explored as the backbone of these boron-containing complexes, several of which are highlighted below.

1.2 Boron complexes of β -diketiminates

First discovered in the mid 1960s, β -diketiminates (**1.1**) were initially employed in the coordination chemistry of metal complexes.¹⁰ This monoanionic ligand is among the most fundamental chelating systems in coordination chemistry and has become more common throughout literature as a result of its facile synthesis including sterically demanding derivatives, and ease of tunability. As a result of its growing popularity, four-coordinate boron complexes of β -diketiminates have been synthesized in moderate yields (*e.g.* **1.2**) and have been shown to have interesting luminescent properties.¹¹



For example, the Chujo group synthesized a series of functionalized boron-containing β -diketimines (**1.6**) and studied their use as light-emitting solid materials.¹² The diimine ligands were synthesized via the reaction between *N*-phenylimine (**1.3**) and imidoyl chloride (**1.4**) with the corresponding substituents (Scheme 1.1). The BF_2 moiety was then incorporated using $\text{BF}_3 \cdot \text{OEt}_2$ in toluene to afford a series of compounds (**1.6a–d**) with overall yields varying from 10 to 36%.



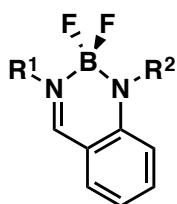
Scheme 1.1. Synthesis of functional boron diiminate complexes. Yields are indicated in brackets.¹²

The spectroscopic properties of compounds **1.6a–1.6d** were studied, and it was found that all four compounds showed strong $\pi \rightarrow \pi^*$ absorption transitions in the UV-Vis spectrum from λ_{max} 355–391 nm. The emission of these compounds was found to be red-shifted with the introduction of electron donating substituents, with compounds **1.6a–c** emitting at 448, 473 and 470 nm, respectively, while compound **1.6d** exhibited emission at 602 nm. All four compounds were weakly luminescent in THF at room temperature (298 K), with quantum yields of fluorescence (Φ_{F}) below 0.01. Upon cooling to 77 K, the emission intensities of these compounds increased, indicating that the suppression of molecular vibrations and rotations plays an important role in their luminescence. Furthermore, it was discovered that upon crystallization, the emission drastically increased further, indicating these compounds are CIEE (crystallization-induced emission enhancement) active. This process refers to a unique phenomenon in which a compound weakly emits as an amorphous solid, but emits more effectively in

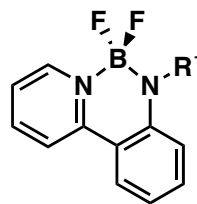
crystalline states. In the case of these compounds, both amorphous and crystalline samples were studied. Low intensity emission was observed from the amorphous samples ($\Phi_F = 0.01\text{--}0.04$) whereas the corresponding crystalline samples showed much more intense emission ($\Phi_F = 0.04\text{--}0.59$), indicating that these compounds are CIEE active.^{13,14}

1.3 Boron Complexes of Anilido-imines & Anilido-pyridines

With a similar core structure to that of the β -diketimines, boron complexes of anilido-imines (e.g. **1.7**) and anilido-pyridines (e.g. **1.8**) have also been synthesized.^{15,16} These complexes exhibit large Stokes shifts and moderate quantum yields with tunable absorption and emission profiles.



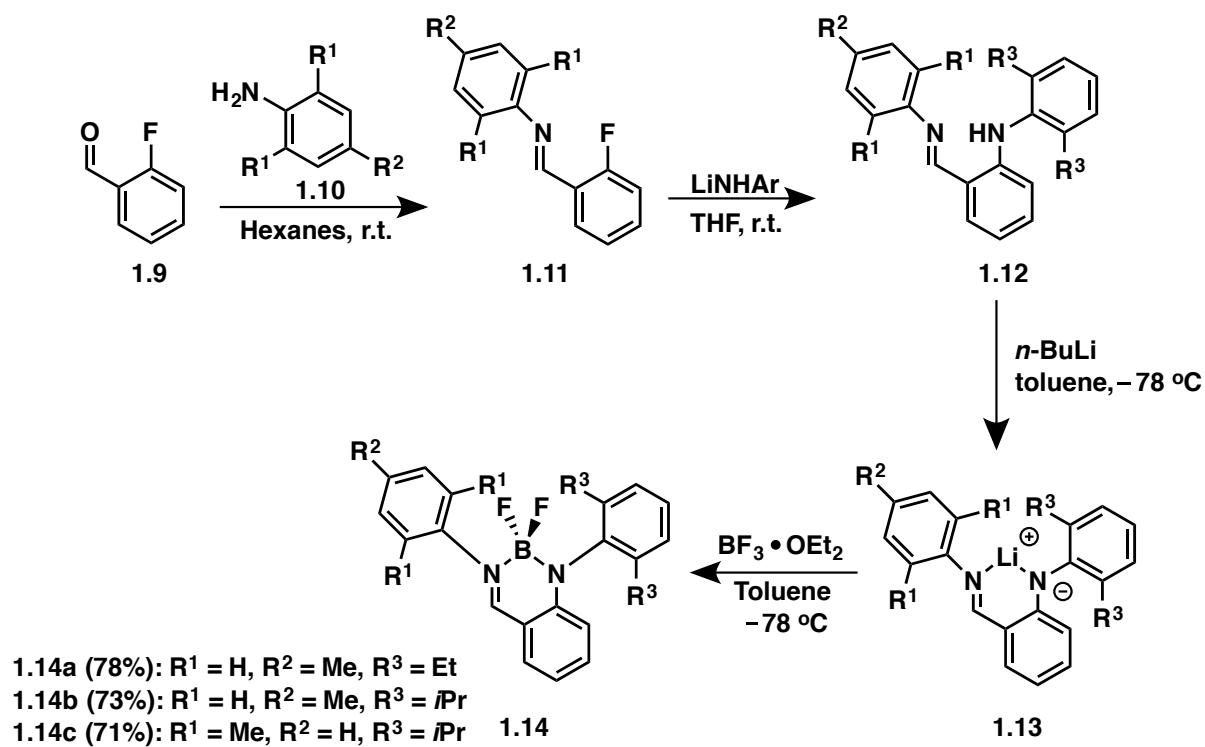
1.7



1.8

The Mu group synthesized a series of boron-containing anilido-imines and explored the effects of sterics on the absorption and emission of these complexes.¹⁷ The ligands were synthesized by stirring 2-fluorobenzaldehyde (**1.9**) in the presence of the corresponding aryl amine (**1.10**) to form **1.11**, followed by the slow addition of a lithiated aryl amine at room temperature to afford **1.12** in 75–78% yield (Scheme 1.2). The anilido-imines were then lithiated at $-78\text{ }^\circ\text{C}$ in toluene using *n*-BuLi and stirred overnight at room temperature. The resulting mixture was added dropwise to a solution of $\text{BF}_3 \cdot \text{OEt}_2$ in toluene at $-78\text{ }^\circ\text{C}$ and stirred overnight at room temperature to afford compounds **1.14a–c**. The λ_{max} values for compounds **1.14a**, **b** and **c** were found to be 440, 440 and 429 nm, with λ_{em} values of 511, 512, and 491 nm and Φ_F values of 0.55, 0.57, and 0.58, respectively. It was found that by substituting hydrogen for methyl at the *ortho* position of the imine-bound phenyl ring forces a change in conformation such that the phenyl

ring twists and decreases the extent of conjugation, thereby blue-shifting the absorption and emission maxima of **1.14c** relative to **1.14a** and **1.14b**.

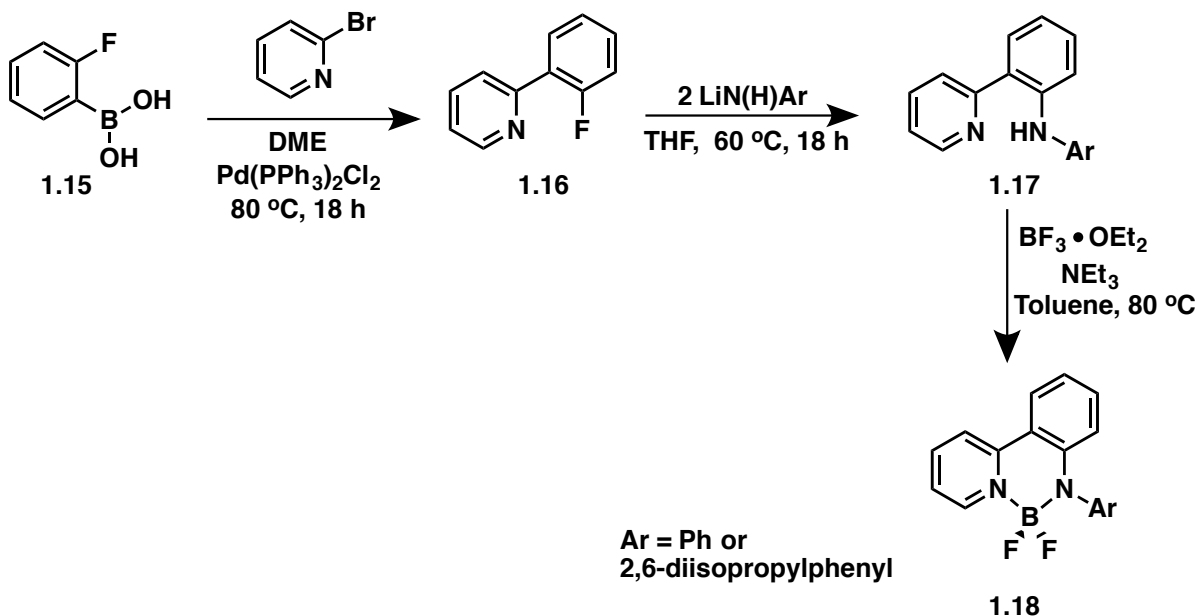


Scheme 1.2. Synthesis of boron-containing anilido-imine complexes. Yields are indicated in brackets.¹⁷

The λ_{max} values of the boron-containing anilido-imine complexes were found to be significantly red-shifted (~ 80 nm) relative to the free anilido-imine ligands. These values suggested that the formation of the B-N bond lowers the $\pi \rightarrow \pi^*$ energy gap, resulting in a red-shift of the absorption spectrum. Furthermore, the Φ_{F} values of the boron-containing complexes were significantly higher than those of the free ligands ($\Phi_{\text{F}} \sim 0.56$ vs. ~ 0.03). The incorporation of the BF_2 moiety also rigidifies the ring, therefore reducing the vibrational energy loss and increasing the Φ_{F} values.

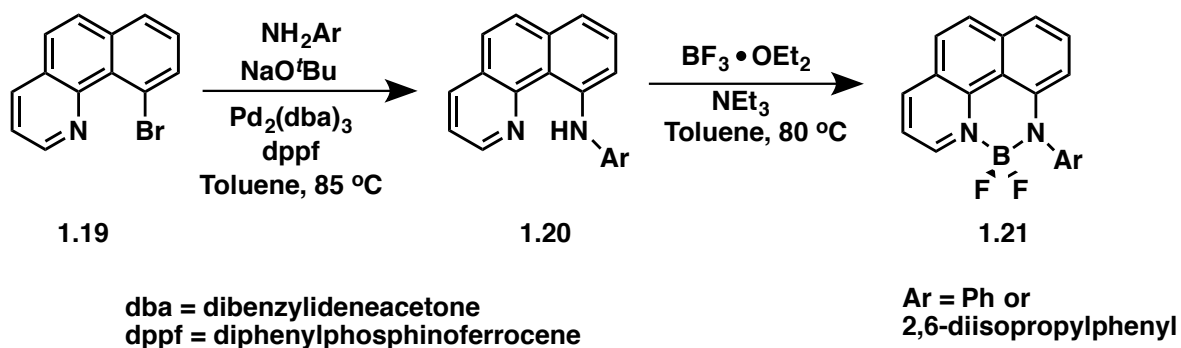
Similar boron-containing complexes of anilido-pyridines were synthesized by the Piers group.¹⁸ The first series of complexes was prepared by Suzuki-Miyaura coupling of 2-fluorophenylboronic acid (**1.15**) and the corresponding α -bromo pyridine in dimethoxyethane (DME) (Scheme 1.3). The resulting aryl fluoride (**1.16**) was then

treated with 2 equiv. of a lithiated aryl amine generated via *n*-BuLi in THF at $-78\text{ }^{\circ}\text{C}$ and the final solution was heated overnight. The ligand was then stirred in toluene with NEt_3 and $\text{BF}_3\cdot\text{OEt}_2$ and heated overnight to afford the final boron-containing anilido-pyridines in 60% yield for the phenyl derivative and 84% for the diisopropylphenyl (dipp) derivative.



Scheme 1.3. Suzuki-Miyaura coupling for the synthesis of boron-containing anilido-pyridines.¹⁸

The second series of complexes was synthesized through a palladium-catalyzed Hartwig-Buchwald amination of 10-bromobenzo[*h*]quinoline (**1.19**) and the respective aniline in toluene at $85\text{ }^{\circ}\text{C}$ (Scheme 1.4). The resulting ligand was then stirred in toluene with NEt_3 and $\text{BF}_3\cdot\text{OEt}_2$ and heated overnight to afford the final boron-containing anilido-pyridines in an 81% yield for the phenyl derivative and 44% yield for the dipp derivative.

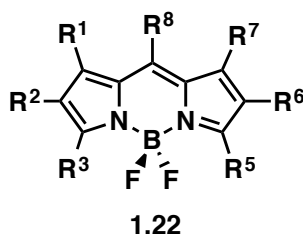


Scheme 1.4. Synthesis of boron-containing anilido-pyridines via Hartwig-Buchwald amination.¹⁸

The spectroscopic properties of these boron-containing anilido-pyridines was investigated. It was found that the less conjugated BF₂ complexes (**1.18**) absorbed in the UV-Vis region in dichloromethane at λ_{max} of 416 nm for the phenyl derivative and 417 nm for the dipp derivative, with λ_{em} of 531 ($\Phi_{\text{F}} = 0.33$) and 511 nm ($\Phi_{\text{F}} = 0.29$), respectively. The more conjugated BF₂ complexes (**1.21**) absorbed in the UV-Vis region at λ_{max} of 465 nm for the phenyl derivative and 466 nm for the dipp derivative, with λ_{em} of 584 ($\Phi_{\text{F}} = 0.60$) and 569 nm ($\Phi_{\text{F}} = 0.66$), respectively. The large differences in fluorescence quantum yield could be explained when looking at the crystallographic data. X-ray crystallography of the Suzuki-coupled derivatives revealed significant twisting in the ligand backbone of complex **1.18**, while the ligand backbone of the rigidified phenyl complex (**1.21**) was found to be completely flat. This led to the conclusion that the flexibility of the ligand backbone of complex **1.18** was providing nonradiative decay pathways for excited state relaxation, leading to decreased fluorescence quantum yields, while the rigidified phenyl complex **1.21** did not allow for the same nonradiative decay to occur. Furthermore, these complexes exhibited exceptional photostability when compared with current commercially available dyes, as their absorption profiles were unchanged after 10–16 h of irradiation at 420 nm in dichloromethane at room temperature. These properties have opened the possibility for these dyes to be used as fluorescent biological probes.

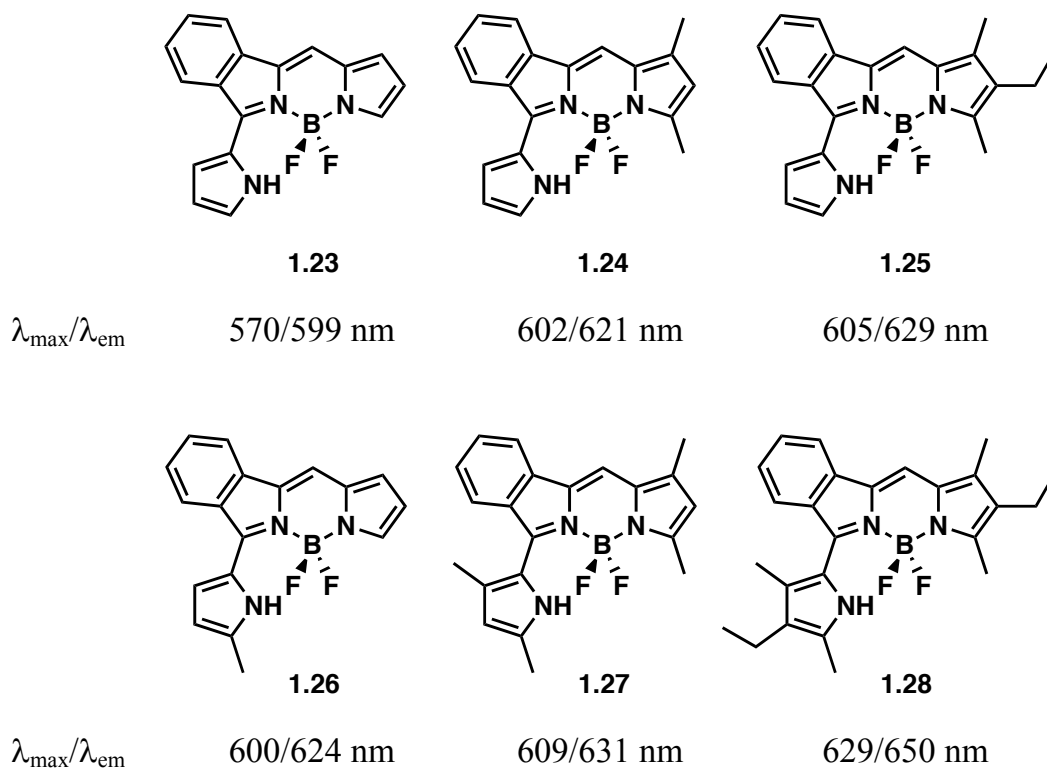
1.4 Boron dipyrromethenes (BODIPYs)

Perhaps the most popular class of boron-containing dyes are known as boron dipyrromethenes (BODIPYs),^{1,19,20,21} which consist of a dipyrromethene core coordinated to a BF₂ fragment (**1.22**). First synthesized in the late 1960s,²² these dyes have become incredibly popular as a result of their highly desirable properties, including high molar absorptivities and fluorescence quantum yields and narrow absorption/emission bands.

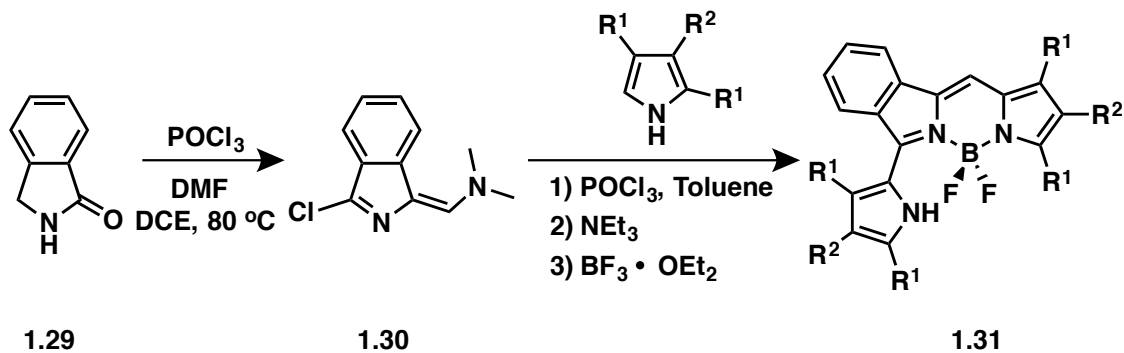


Although popular, classical BODIPYs are difficult to synthesize and require numerous synthetic steps often employing expensive metal catalysts. These compounds are also generally hydrophobic and typically exhibit maximum wavelengths of emission (λ_{em}) below 550 nm, making their use in biological applications challenging. However, numerous groups have overcome these challenges by developing synthetic strategies and tuning the spectroscopic and solubility properties of these compounds via structural modification at the meso position (**1.22** R⁸) as well as along the pyrrole rings (**1.22** R¹–R³).

For example, the Jiao group synthesized a series of isoindole BODIPY fluorophores (**1.23**–**1.28**), in which greater alkyl substitution was shown to red-shift their absorption and emission maxima and explored their use as near-IR emitting pH sensors.² These compounds were synthesized via direct condensation of 3-chloroisoindolin-1-ylidene-*N,N*-dimethylmethanamine (**1.30**) with the suitable derivatized pyrrole in order to produce the desired dipyrromethene core (Scheme 1.5). The BF₂ moiety was then incorporated using BF₃•OEt₂ and NEt₃ in toluene to afford the final BODIPY complexes in 20–50% yields.

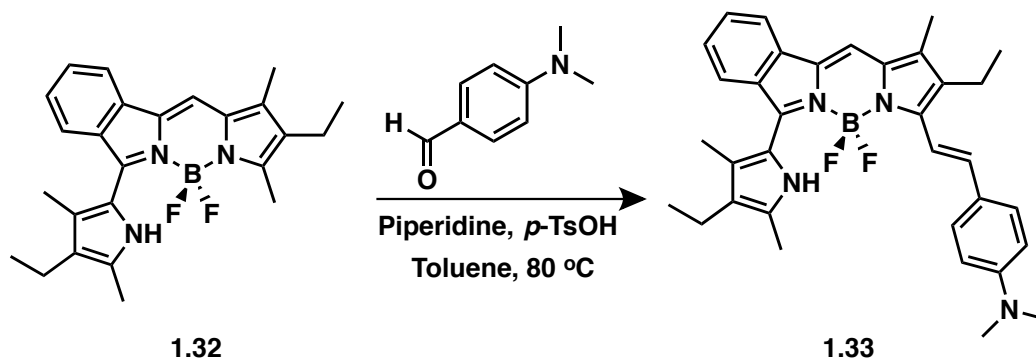


UV-Vis absorption spectra revealed increasingly red-shifted λ_{\max} and λ_{em} values with increasing alkyl substitution on the BODIPY core relative to the parent BODIPY (**1.23**), with all complexes exhibiting fluorescence quantum yields of 0.60–0.80. X-ray crystallography indicated the BODIPY cores were planar, with hydrogen bonding observed between the fluorine atoms and the pyrrolic proton, further rigidifying the structures. A gradual increase of the dihedral angle was observed between the free pyrrole and the BODIPY core with an increase of alkyl substitution at the free pyrrole (**1.23–1.28**), and as a result, a slight decrease in the fluorescence quantum yields was observed.



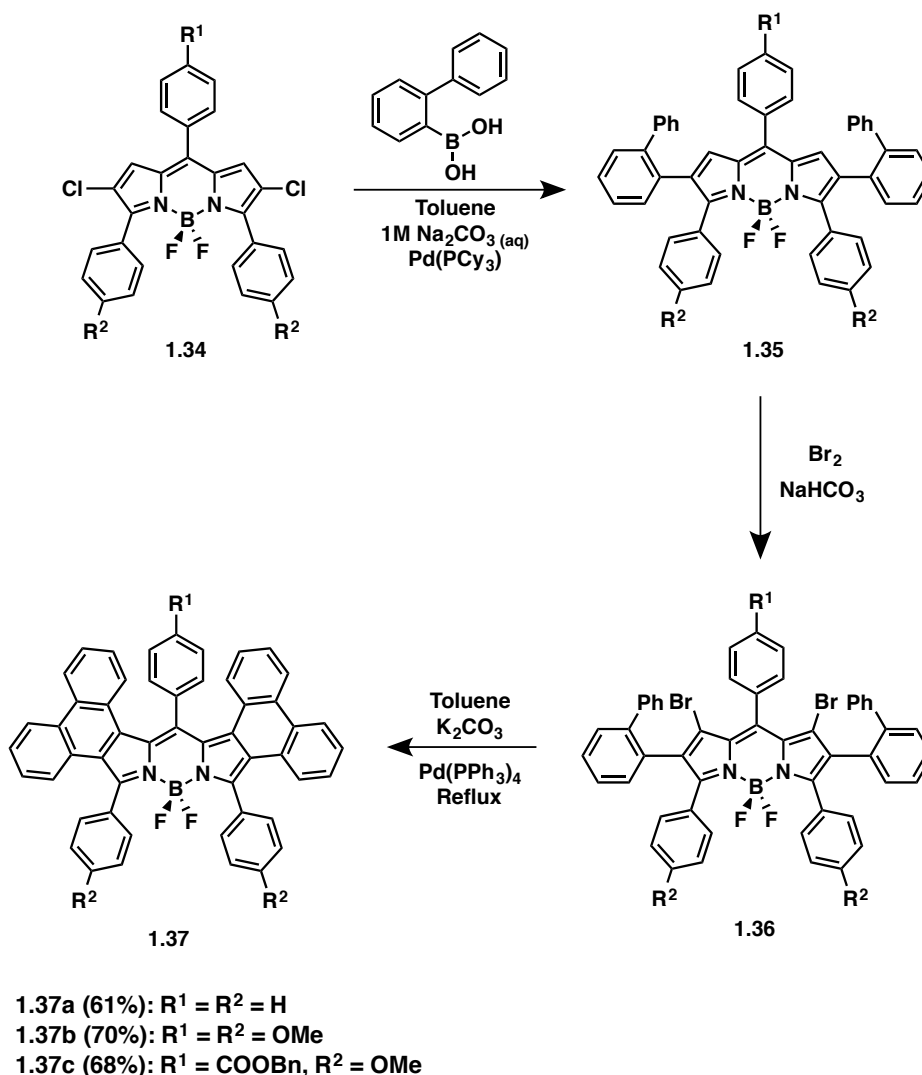
Scheme 1.5. Synthesis of alkyl-substituted BODIPY complexes.²

Alkyl-substituted BODIPY derivative (**1.28**) was further functionalized with a dimethylaniline moiety via the Knoevenagel condensation of 4-(dimethylamino)benzaldehyde in the presence of piperidine in toluene to produce complex **1.33** in 75% yield (Scheme 1.6). It absorbed strongly at 713 nm and weak fluorescence in the near-IR at 805 nm ($\Phi_F = 0.05$), the latter due to intramolecular charge transfer. However, upon addition of trifluoroacetic acid (TFA), a stepwise disappearance of the absorption maxima (λ_{\max}) at 415 and 713 nm was observed, with the appearance of new blue-shifted bands centred at 354 and 671 nm. Furthermore, a blue shift in λ_{em} was seen from 805 to 702 nm along with an increase in fluorescence intensity, suggesting the formation of a monoprotonated species. This revealed promising potential for the BODIPY complex **1.32** as a ratiometric “turn-on” near-IR fluorescent pH sensor.



Scheme 1.6. Synthesis of a fluorescent pH-sensing BODIPY complex via Knoevenagel condensation.²

Vicente and co-workers developed an efficient synthetic methodology for π -extended BODIPY systems in order to tune the absorption and emission maxima of their BODIPY systems to the red/near-IR region in order to target biological applications.²³ These phenanthrene-fused BODIPYs were synthesized by first reacting the initial halogenated BODIPYs (**1.34**) with 20 equivalents of 2-biphenylboronic acid in the presence of 5% Pd(PCy₃) and 1 M Na₂CO_{3(aq)} in refluxing toluene for 5 h (Scheme 1.7). Bromination reactions were then carried out using 10 equiv. of Br₂ and 10 equiv. of NaHCO₃ in CH₂Cl₂. By then treating the resulting products (**1.36**) with 50 equiv. of K₂CO₃ and Pd(PPh₃)₄ in refluxing toluene for 2 h, the final phenanthrene-fused BODIPY complexes were synthesized in 61–70% yields (**1.37**). All three BODIPY derivatives exhibited a drastic red-shift in the UV-Vis absorption spectra, with λ_{max} values from 566–590 for complexes **1.34a–c** to 642–660 for complexes **1.37a–c**, indicative of the increased π -conjugation. Emission wavelengths were also drastically red-shifted, with λ_{em} values from 597–640 to 671–701. Furthermore, it was found that upon slightly extending the conjugation at the *meso* position, **1.37c** exhibited absorption and emission maxima further red-shifted relative to **1.37a** and **1.37b**. As a result, **1.37a** was further studied for biological evaluation of cancerous human epithelial type 2 (HEp2) cells. Due to its hydrophobic character, the complex was readily taken up by the cells and localized in the endoplasmic reticulum (ER). This compound showed no cytotoxicity toward the cells, and demonstrated strong emission in live cells. These results indicate that this synthetic methodology may be applied effectively as an affordable alternative toward employing near-IR BODIPY-based dyes as bioimaging agents.



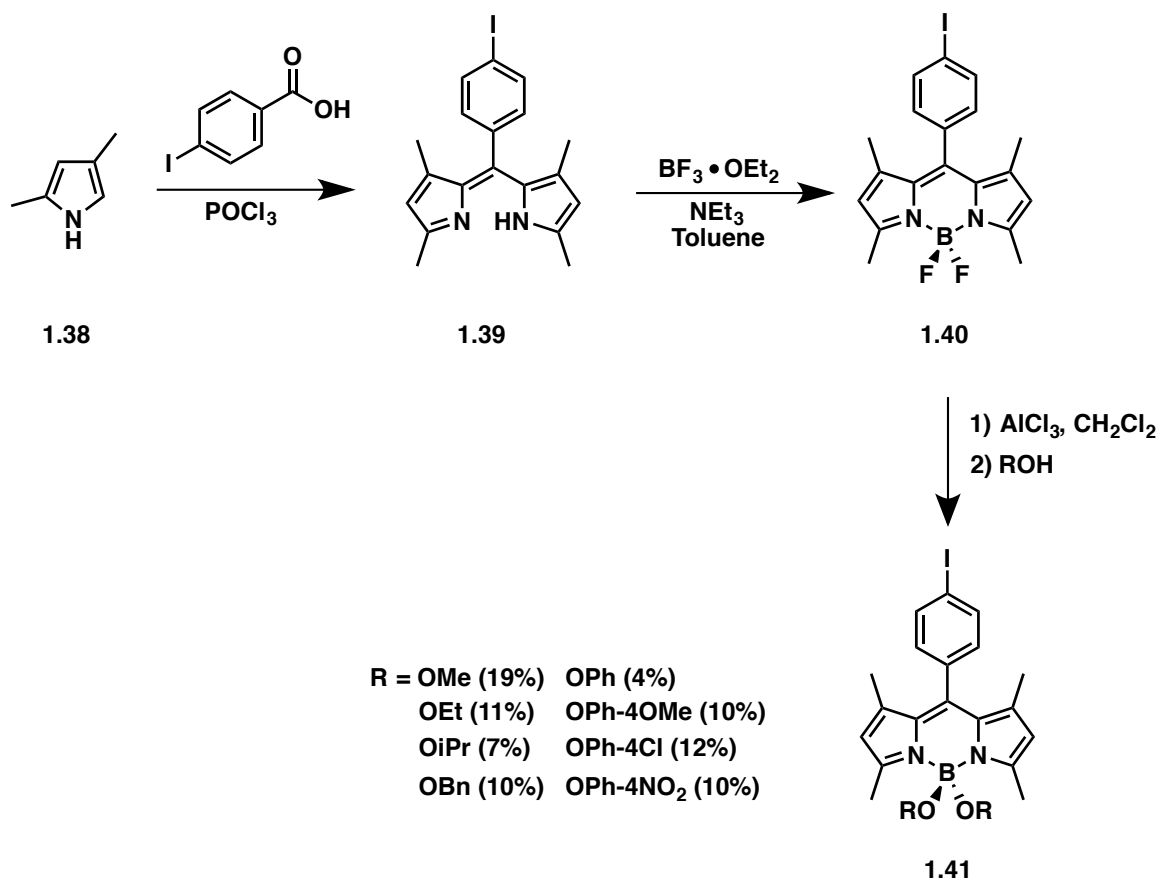
Scheme 1.7. Synthesis of phenanthrene-fused BODIPY complexes. Yields indicated in brackets.²³

1.5 BODIPY Derivatization via Fluorine Displacement

While BODIPYs are an incredibly popular class of fluorescent dyes, it has been shown that under irradiation in polar solvents, their photostability can be limited, which in turn limits their use in biological applications. The B-F bond has been identified as the main source of this instability.²⁴ In an effort to remedy this instability, numerous groups have synthesized BODIPY derivatives where the fluorine atoms of the “F-BODIPY” are replaced with chloride,²⁵ alkyl,²⁶ aryl (“C-BODIPY”),²⁷ alkoxy (“O-BODIPY”)^{28,29,30,31} or ethynyl (“E-BODIPY”)^{24, 32,33,34,35} functionalities.

1.5.1 *O*-BODIPY

The Hibert group synthesized a series of *O*-BODIPYs with alkoxy/aryloxy functionalities replacing the fluorine atoms at the boron centre.²⁹ These compounds were synthesized via the direct condensation of a pyrrole (**1.38**) with 4-iodobenzoic acid in phosphorus oxychloride used as both a reagent and solvent at reflux for 1 h (Scheme 1.8). The corresponding dipyrromethene (**1.39**) was then stirred in a solution of toluene and NEt_3 at 80 °C in the presence of $\text{BF}_3 \cdot \text{OEt}_2$ for 30 min to afford the *F*-BODIPY (**1.40**) in a 19% yield. Treatment of the resulting BODIPY with AlCl_3 in dry CH_2Cl_2 and subsequent addition of an alcohol resulted in poor to moderate conversion to the resulting *O*-BODIPY (**1.41**). Interestingly, the authors noted that the substitution of fluorine atoms did not occur in the absence of AlCl_3 , indicating this reagent plays an important role in activating the B-F bond such that subsequent nucleophilic substitution may occur.

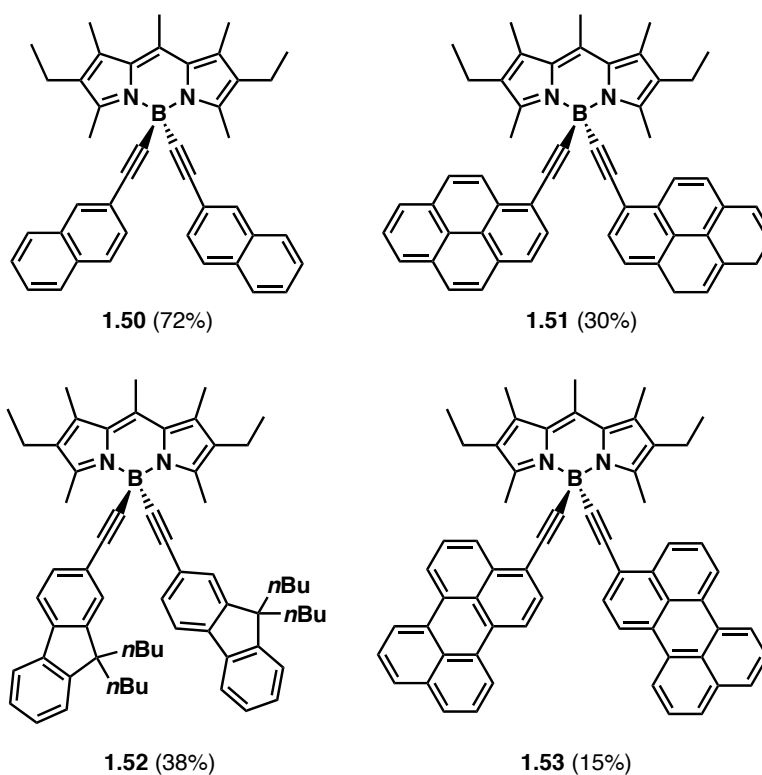


Scheme 1.8. Synthesis of *O*-BODIPYs. Overall yields indicated in brackets.²⁹

The authors examined the spectroscopic properties of these *O*-BODIPYs and found that the introduction of various alcohols produced only minor changes in the absorption maxima (1–3 nm red shift), with the parent *F*-BODIPY exhibiting a λ_{max} of 504 nm. Fluorescence quantum yields were calculated for all compounds, and it was found that relative to the parent *F*-BODIPY ($\Phi_{\text{F}} = 0.57$), only the *i*Pr ($\Phi_{\text{F}} = 0.67$), OBn ($\Phi_{\text{F}} = 0.65$) and OPh-4NO₂ ($\Phi_{\text{F}} = 0.71$) derivatives had higher quantum yields. Of these, only the OPh-4NO₂ derivative was found to have a fluorescence lifetime longer than that of the parent *F*-BODIPY, and as a result this compound was explored further. Over the course of 12 h, it was found that this derivative had greater photostability than that of the parent BODIPY in aqueous media, supporting the notion of the B-F bond being the main source of instability in these complexes. Coupled with its greater fluorescence intensity, this *O*-BODIPY derivative shows promise as a label for cell-based assays.

The Chau group developed a one-pot pathway for the synthesis of *O*-BODIPYs in yields comparable to other methods in the literature.³¹ In this synthesis, the targeted BODIPY was synthesized directly from the corresponding aldehyde, pyrrole and trimethylborate (Scheme 1.9). Initially, 2,4-dimethylpyrrole (**1.42**) was reacted with the corresponding aldehyde in the presence of trifluoroacetic acid (TFA) in THF overnight (Scheme 1.9). The resulting dipyrromethane (**1.43**) was then oxidized using tetrachloro-*p*-benzoquinone, followed by the addition of NEt₃ and trimethyl borate, to afford the final *O*-BODIPYs after 24 h (**1.45**).

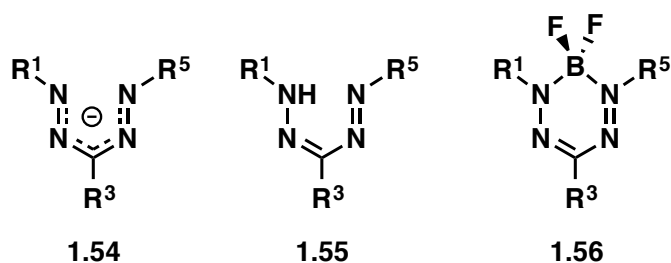
exhibited a strong $\pi \rightarrow \pi^*$ absorption between 516–528 nm indicative of the BODIPY core, with a higher energy absorption at 284 (**1.50**), 371 (**1.51**), 323 (**1.52**) or 464 (**1.53**) nm relating to the respective polyaromatic functionalities bound to the boron atom through the acetylene moiety.



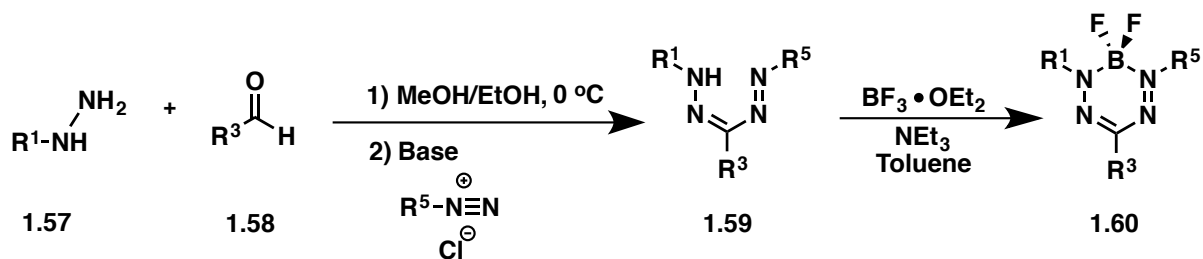
For all the newly synthesized compounds, excitation in the 516–528 nm range led to strong emission in the 535–540 nm region with quantum yields of $\Phi_F = 0.90$ – 0.95 . Interestingly, upon excitation of the more intense and higher energy absorption bands relating to the polyaromatic moieties, the observed emission was not from of the polyaromatic species but rather the BODIPY core. This resulted in nearly quantitative energy transfers (95–99%) with the exception of the naphthyl compound (**1.50**) due to poor spectral overlap with the BODIPY core. As a result, these *E*-BODIPYs exhibited a virtual Stokes shift of over 570 – 758 cm^{-1} , making these dyes promising candidates for biological labeling experiments.

1.6 Formazans & BF₂ Formazanate Complexes

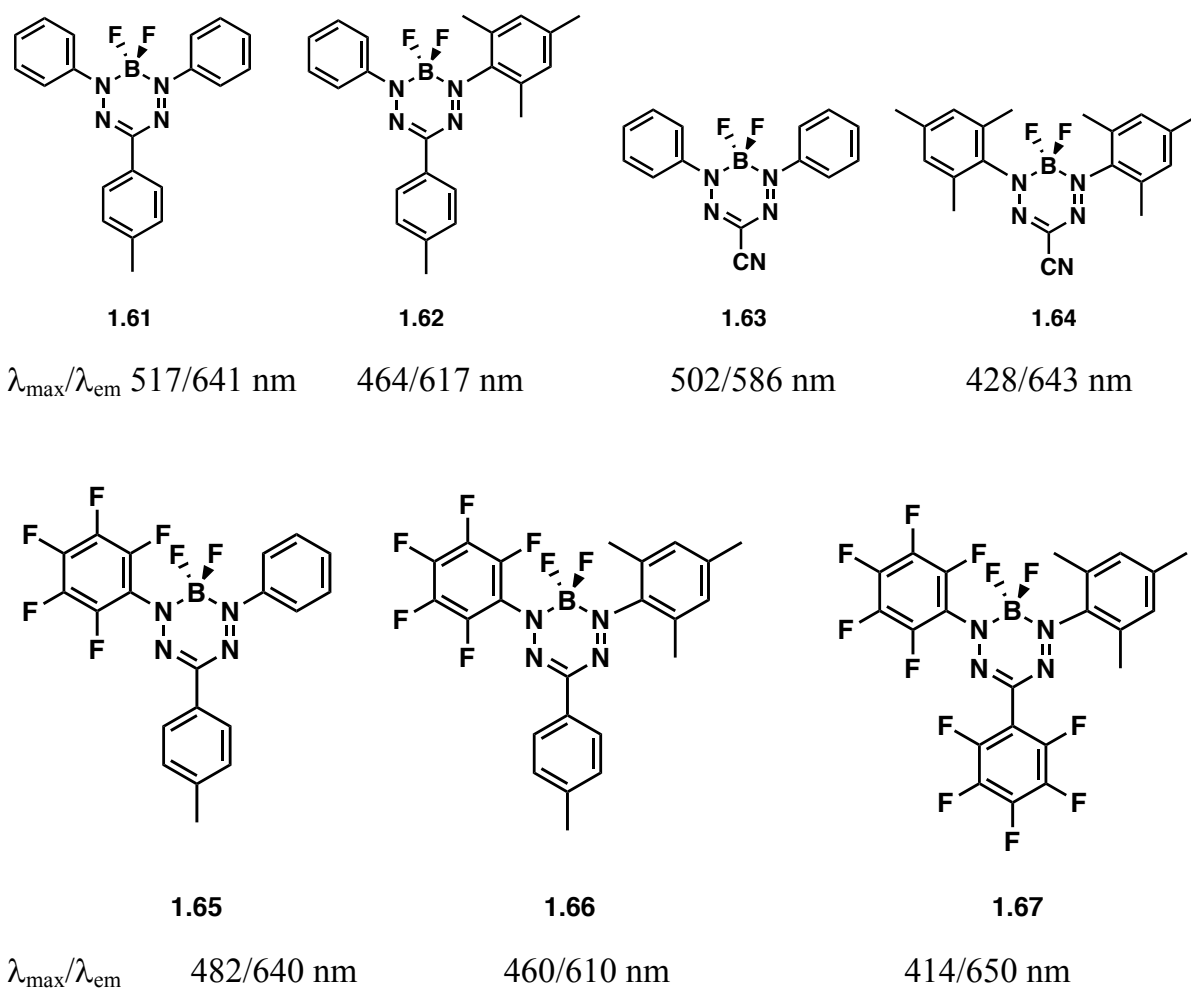
While much of the focus in the literature regarding BF₂-based fluorescent dyes has focused on the BODIPY framework, formazanate ligands (**1.54**) that are derived from formazans (**1.55**) and their resulting BF₂ complexes (**1.56**) have emerged as promising alternatives. Formazans are nitrogen-rich analogs of β -diketiminates that typically possess aryl substituents at the R¹ and R⁵ positions, with R³ bearing alkyl, aryl, nitro or cyano functionalities.



This new family of complexes has desirable spectroscopic and electrochemical properties that may be readily tuned via structural modification.^{37,38} For example, the Otten group synthesized a series of BF₂ formazanate complexes and explored substituent effects on both optical and redox properties.³⁹ Formazans were synthesized in a multi-step procedure where the hydrazones were first isolated after reacting the desired hydrazine (**1.57**) with an aryl aldehyde (**1.58**) in MeOH or EtOH (Scheme 1.11). Separately, a diazonium salt was prepared by mixing an aniline with water, HCl and NaNO₂ at 0 °C. The diazonium salt was then added to a solution of the hydrazone in water, acetone and base at 0 °C. The solution was stirred overnight while warming to room temperature and the desired formazans (**1.59**) were isolated in various yields (11–46%). The BF₂ moiety was then incorporated using BF₃•OEt₂ and NEt₃ in toluene at 80 °C to afford the final complexes in 28–42% yield (**1.61–1.67**).



Scheme 1.11. General synthesis of formazan ligands and resulting BF₂ complexes.³⁹

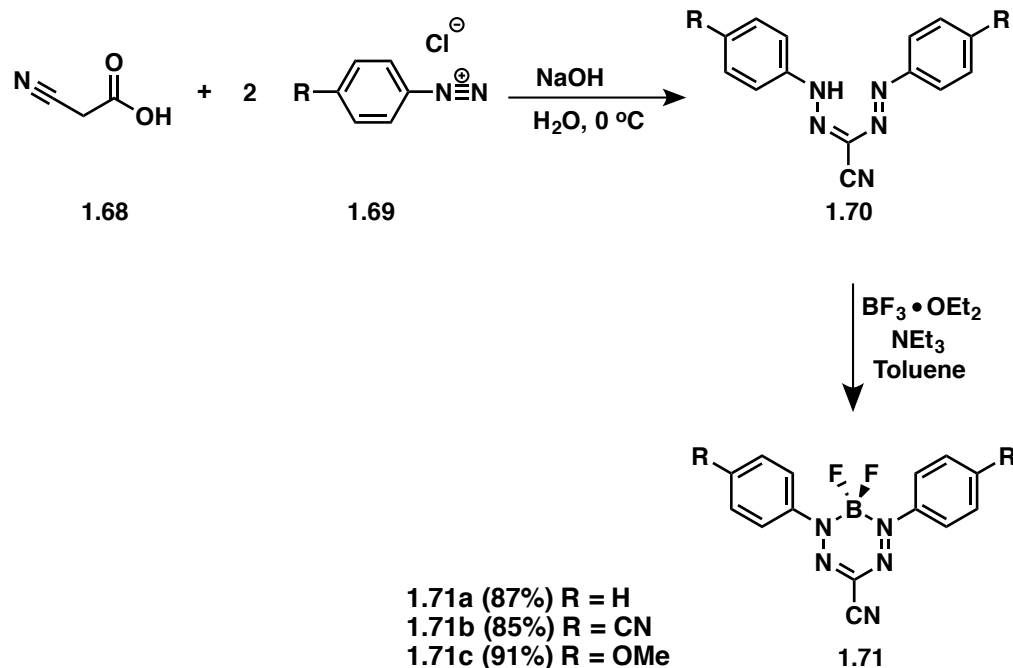


Compounds **1.61–1.67** were found to absorb strongly in the visible region of the UV-Vis spectrum (414–517 nm). In all cases, it was observed that upon replacing substituents for bulkier variants (phenyl for mesityl), a blue-shift in the absorption and emission spectra was observed. This was determined to be a result of a near perpendicular orientation of the mesityl group, as electrons are no longer conjugated

between the formazanate backbone and the mesityl ring. A blue-shift was also observed upon replacing phenyl or *p*-tolyl rings with more electronegative C₆F₅ rings, as a result of the more electronegative substituent increasing the HOMO/LUMO gap. All compounds with the exception of **1.63** ($\Phi_F = 0.15$) were found to be essentially non-emissive ($\Phi_F < 0.01$). Redox properties of these complexes were also explored using cyclic voltammetry. It was found that all complexes exhibit two quasi-reversible reductions, corresponding to the formation of the radical anion and dianion and that redox potentials could be varied greatly by manipulating the substituents on the formazanate scaffold. Upon increasing the electron-donating ability of the R³ substituent, redox potentials shifted to more negative values, while electron-withdrawing substituents result in more positive potentials. Changing the nature of the *N*-aryl substituents to more electron-withdrawing substituents was found to push the redox potentials to more positive values, with the opposite trend holding true for electron-donating substituents.

The Gilroy group has also explored BF₂ formazanates and demonstrated their readily tunable optical and electronic properties through substituent modification.^{38,40,41} For example, a series of 3-cyano BF₂ formazanates were synthesized in high yields (87–91%) and their spectroscopic properties were explored. In air, cyanoacetic acid (**1.68**) was dissolved in water and NaOH (Scheme 1.12). Separately, the corresponding diazonium salt (**1.69**) was generated via the addition of a cold aqueous NaNO₂ solution to mixture of water, HCl and the desired amine precursor. The diazonium was then slowly added to the basic cyanoacetic acid solution and stirred for 6 h, producing the desired formazan (**1.70**) in high yields (85–87%). The purified formazans were then stirred in a solution of BF₃•OEt₂, NEt₃ and toluene at 80 °C overnight to produce the corresponding BF₂ complexes. UV-Vis absorption spectroscopy data revealed that each of these complexes showed strong, substituent-dependent absorption from λ_{max} 502 nm to 515 nm to 572 nm corresponding to the $\pi \rightarrow \pi^*$ transition for complexes **1.71a–c**, respectively. It was found that all three complexes were also emissive, with λ_{em} values

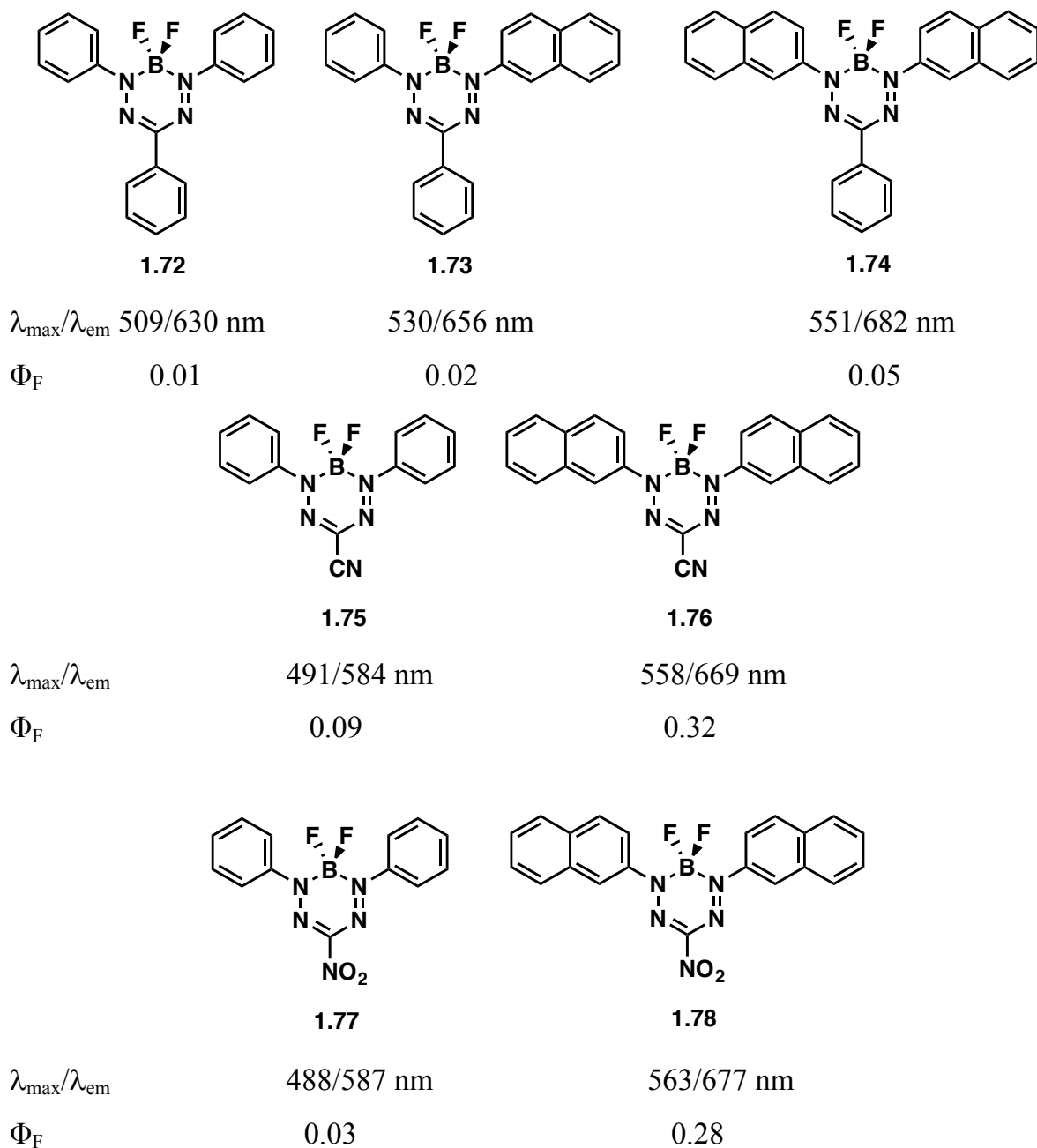
of 586 nm, 598 nm and 656 nm and Φ_F values of 0.15, 0.14 and 0.77 for complexes **1.71a–c**, respectively.



Scheme 1.12. Synthesis of 3-cyano BF_2 formazanate complexes.³⁸

Substituent effects were also examined by cyclic voltammetry, where it was found that each complex exhibited two reversible reduction events, with the electron donating derivative (**1.71c**) exhibiting more negative reduction potentials and the electron withdrawing derivative (**1.71b**) exhibiting more positive reduction potentials relative to **1.71a**. Solid state structures revealed the boron atoms in all three complexes adopt a distorted tetrahedral geometry and are slightly displaced from the N_4 plane of the formazanate backbone, while moderate twisting of the *N*-aryl substituents of all three complexes was also observed.

Recently, the Gilroy group has also demonstrated the effect of extended π conjugation on the properties of BF_2 formazanate dyes by systematically replacing phenyl with naphthyl substituents at the R^1 and R^5 positions of 3-CN, 3- NO_2 and 3-phenyl BF_2 formazanates (**1.72–1.78**).⁴¹



It was demonstrated that extending the π conjugation of these complexes red-shifted the absorption and emission maxima. However, compounds bearing a phenyl substituent at the 3 position were found to be non-emissive in solution, likely due to additional non-radiative decay pathways associated with the carbon-bound substituent. The Gilroy group confirmed this phenomenon in a recent publication in which protonation of a pyridine ring at the R³ position was found to significantly increase the

fluorescence intensity.⁴² X-ray crystallography revealed hydrogen bonding between the pyridyl NH and a *p*-toluenesulfonate counterion. This discovery supports the notion that upon protonation of the pyridine substituent at the 3-substituent, potential vibrational and rotational non-radiative decay pathways are restricted via steric hindrance and intermolecular hydrogen bonding.

BODIPYs and BF₂ formazanate dyes are both promising candidates for a wide array of applications as a result of their tunable spectroscopic properties. Where BF₂ formazanate dyes have the advantage is that they are more synthetically accessible (fewer steps) and can be isolated in greater yields. However, structural modification of BF₂ formazanate complexes has been explored only at the 1, 3 and 5 positions of the formazanate backbone, while chemistry at the boron centre has not been explored to date.

1.7 Scope of Thesis

This thesis focuses on the synthesis of alkynyl-substituted boron formazanates, and explores the electronic and spectroscopic changes that result as various alkyne-based functionalities are introduced at boron, replacing the fluorine substituents of a BF₂ formazanate. The interest in this work lies in the possibility of developing new synthetic protocols to manipulate the boron formazanate scaffold, which may increase their overall stability, alter their properties and open the door for these molecules to be used in a broader scope of applications.

Chapter 2 will focus on the synthesis and characterization of novel alkynyl-substituted boron formazanate complexes using an adapted methodology from BODIPY systems. A detailed comparison of their spectroscopic, electrochemical and X-ray crystallographic properties will be described.

Chapter 3 will focus on the post-synthetic modification and functionalization of alkynyl-substituted boron formazanate complexes, as well as a redox-active alkynyl-substituted complex and its oxidized and reduced forms. A comparison of their spectroscopic and electrochemical properties will be described. X-ray crystallographic studies will also be discussed.

Chapter 4 will summarize the impact of my work on the field and possible future directions for the project.

1.8 References

1. Loudet, A.; Burgess, K. *Chem. Rev.* **2007**, *107*, 4891–4932.
2. Yu, C. J.; Wu, Q. H.; Wang, J.; Wei, Y.; Hao, E. H.; Jiao, L. J. *J. Org. Chem.* **2016**, *81*, 3761–3770.
3. Han, J. Y.; Loudet, A.; Barhoumi, R.; Burghardt, R. C.; Burgess, K. *J. Am. Chem. Soc.* **2009**, *131*, 1642–1643.
4. Zeng, L.; Miller, E. W.; Pralle, A.; Isacoff, E. Y.; Chang, C. J. *J. Am. Chem. Soc.* **2006**, *128*, 10–11.
5. Yang, S. K.; Shi, X. H.; Park, S.; Ha, T.; Zimmerman, S. C. *Nat. Chem.* **2013**, *5*, 692–697.
6. Niu, L. Y.; Guan, Y. S.; Chen, Y. Z.; Wu, L. Z.; Tung, C. H.; Yang, Q. Z. *J. Am. Chem. Soc.* **2012**, *134*, 18928–18931.
7. Poirel, A.; Retailleau, P.; De Nicola, A.; Ziessel, R. *Chem. Eur. J.* **2014**, *20*, 1252–1257.
8. Stockert, J. C.; Horobin, R. W.; Colombo, L. L.; Blazquez-Castro, A. *Acta Histochem.* **2018**, *120*, 159–167.
9. Atilgan, S.; Ekmekci, Z.; Dogan, A. L.; Guc, D.; Akkaya, E. U. *Chem. Commun.* **2006**, 4398–4400.
10. Parks, J. E.; Holm, R. H. *Inorg. Chem.* **1968**, *7*, 1408–1416.
11. Tanaka, K.; Chujo, Y. *NPG Asia Mater.* **2015**, *7*, 1–15.

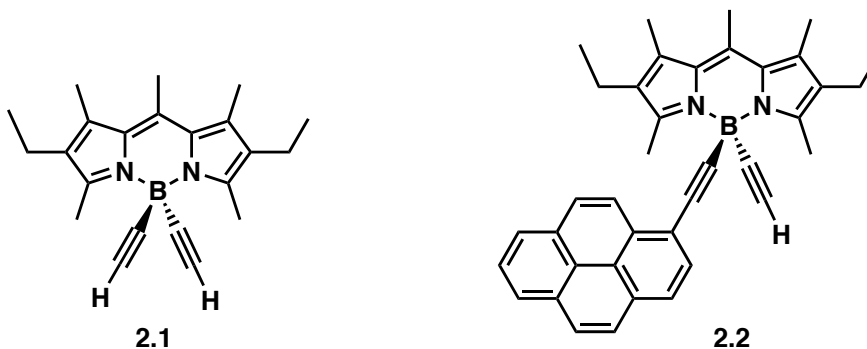
12. Yoshii, R.; Hirose, A.; Tanaka, K.; Chujo, Y. *J. Am. Chem. Soc.* **2014**, *136*, 18131–18139.
13. Qian, B. X.; Baek, S. W.; Smith, M. R. *Polyhedron* **1999**, *18*, 2405–2414.
14. Barbon, S. M.; Staroverov, V. N.; Boyle, P. D.; Gilroy, J. B. *Dalton Trans.* **2014**, *43*, 240–250.
15. Hao, Q.; Yu, S.; Li, S.; Chen, J.; Zeng, Y.; Yu, T.; Yang, G.; Li, Y. *J. Org. Chem.* **2014**, *79*, 459–464.
16. Yang, N.; Xin, L.; Gao, W.; Zhang, J.; Luo, X.; Liu, X.; Mu, Y. *Dalton Trans.* **2012**, *41*, 11454–11463.
17. Ren, Y.; Liu, X. M.; Xia, H.; Ye, L.; Mu, Y. *Eur. J. Inorg. Chem.* **2007**, 1808–1814.
18. Araneda, J. F.; Piers, W. E.; Heyne, B.; Parvez, M.; McDonald, R. *Angew. Chem. Int. Ed.* **2011**, *50*, 12214–12217.
19. Ge, Y.; O'Shea, D. F. *Chem. Soc. Rev.* **2016**, *45*, 3846–3864.
20. Kowada, T.; Maeda, H.; Kikuchi, K. *Chem. Soc. Rev.* **2015**, *44*, 4953–4972.
21. Lu, H.; Mack, J.; Yang, Y. C.; Shen, Z. *Chem. Soc. Rev.* **2014**, *43*, 4778–4823.
22. Treibs, A.; Kreuzer, F. H. *Liebigs. Ann. Chem.* **1968**, *718*, 208–223.
23. Zhao, N.; Xuan, S.; Zhou, Z.; Fronczek, F. R.; Smith, K. M.; Vicente, M. G. H. *J. Org. Chem.* **2017**, *18*, 9744–9750.
24. Goze, C.; Ulrich, G.; Ziessel, R. *J. Org. Chem.* **2007**, *72*, 313–322.
25. Lundrigan, T.; Crawford, S. M.; Cameron, T. S.; Thompson, A. *Chem. Commun.* **2012**, *48*, 1003–1005.
26. Kee, H. L.; Kirmaier, C.; Yu, L.; Thamyongkit, P.; Youngblood, W. J.; Calder, M. E.; Ramos, L.; Noll, B. C.; Bocian, D. F.; Scheidt, W. R.; Birge, R. R.; Lindsey, J. S.; Holten, D. *J. Phys. Chem. B* **2005**, *109*, 20433–20443.
27. Goze, C.; Ulrich, G.; Mallon, L. J.; Allen, B. D.; Harriman, A.; Ziessel, R. *J. Am. Chem. Soc.* **2006**, *128*, 10231–10239.
28. Gabe, Y.; Ueno, T.; Urano, Y.; Kojima, H.; Nagano, T. *Anal. Biochem.* **2006**, *386*, 621–626.

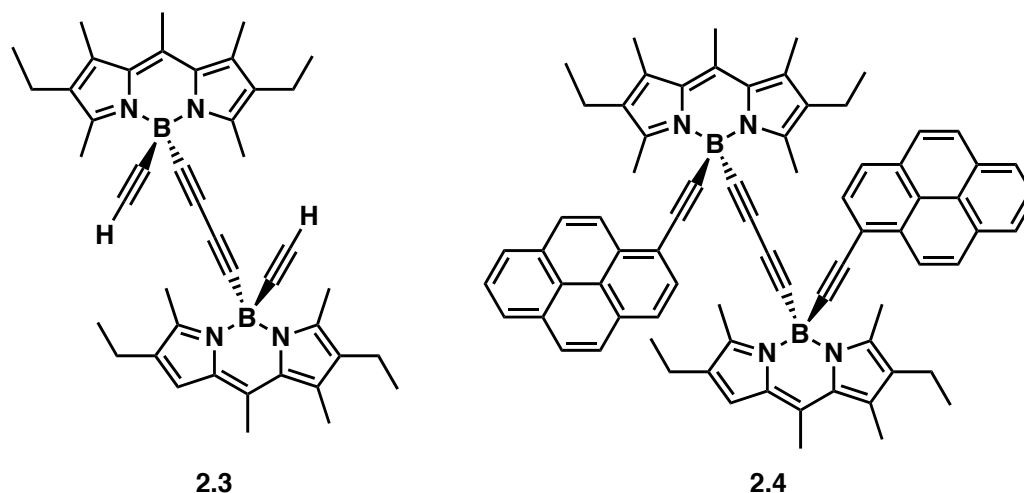
29. Tahtaoui, C.; Thomas, C.; Rohmer, F.; Klotz, P.; Duportail, G.; Mely, Y.; Bonnet, D.; Hibert, M. *J. Org. Chem.* **2007**, *72*, 269–272.
30. Kubota, Y.; Uehara, J.; Funabiki, K.; Ebihara, M.; Matsui, M. *Tetrahedron Lett.* **2010**, *51*, 6195–6198.
31. Liu, K. M.; Tsai, M. S.; Jan, M. S.; Chau, C. M.; Wang, W. J. *Tetrahedron* **2011**, *67*, 7919–7922.
32. Ulrich, G.; Goze, C.; Guardigli, M.; Roda, A.; Ziesel, R. *Angew. Chem. Int. Ed.* **2005**, *44*, 3694–3698.
33. Ziesel, R.; Ulrich, G.; Harriman, A. *New J. Chem.* **2007**, *31*, 496–501.
34. Goze, C.; Ulrich, G.; Ziesel, R. *Org. Lett.* **2006**, *8*, 4445–4448.
35. Goeb, S.; Ziesel, R. *Tetrahedron Lett.* **2008**, *49*, 2569–2574.
36. Gao, Z.; Hao, Y.; Zheng, M.; Chen, Y. *RSC. Adv.* **2017**, *7*, 7604–7609.
37. Chang, M. C.; Otten, E. *Chem. Commun.* **2014**, *50*, 7431–7433.
38. Barbon, S. M.; Reinkeluers, P. A.; Price, J. T.; Staroverov, V. N.; Gilroy, J. B. *Chem. Eur. J.* **2014**, *20*, 11340–11344.
39. Chang, M. C.; Chantzis, A.; Jacquemin, D.; Otten, E. *Dalton Trans.* **2016**, *45*, 9477–9484.
40. Barbon, S. M.; Price, J. T.; Reinkeluers, P. A.; Gilroy, J. B. *Inorg. Chem.* **2014**, *53*, 10585–10593.
41. Barbon, S. M.; Staroverov, V. N.; Gilroy, J. B. *J. Org. Chem.* **2015**, *80*, 5226–5235.
42. Barbon, S. M.; Buddingh, J. V.; Maar, R. R.; Gilroy, J. B. *Inorg. Chem.* **2017**.

Chapter 2

2.1 Introduction

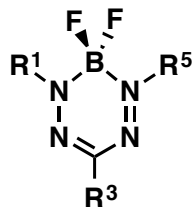
A significant amount of research has been done over the past two decades focusing on boron-containing complexes of chelating *N*-donor ligands.^{1,2} BODIPY systems in particular have garnered significant interest as functional materials and have been extensively studied as a result of their easily tunable optical and spectroscopic properties, making them promising candidates for a number of applications.³ The presence of the B-F bond, however, is an area of concern, as it results in some instability under irradiation and in polar solvents.⁴ Numerous BODIPY derivatives have been explored in which the fluorine atoms have been replaced in order to remedy this instability, giving rise to new families of BODIPYs including *C*-, *O*- and *E*-BODIPYs.^{2,5} As previously mentioned, both *O*- and *E*-BODIPY derivatives exhibit an increased stability toward photoirradiation compared to their parent *F*-BODIPY counterparts, making them useful in biological labeling experiments, cell-based assays and solar cells. Ziessel *et al.* have extensively studied these *E*-BODIPY systems and developed novel bridged *E*-BODIPY dimers that were shown to have unique spectroscopic and redox properties (2.1–2.4).⁶



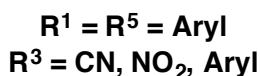


Compounds **2.1**–**2.4** exhibited an intense $\pi \rightarrow \pi^*$ absorption in the UV-Vis spectrum at roughly $\lambda_{\text{max}} = 515$ nm corresponding to the BODIPY backbone, with dimers **2.3** and **2.4** exhibiting transitions with extinction coefficients roughly double that of their monomeric counterparts. **2.1** and **2.3** exhibited very strong emission at 550 nm with Φ_{F} values of 0.92–0.98. Irradiation of the pyrene moieties of **2.2** and **2.4** exhibited exclusive emission at 535 nm ($\Phi_{\text{F}} = 0.80$) corresponding to the BODIPY core, indicating a near quantitative energy transfer of 94%. These molecules also exhibited interesting redox properties, where in all cases, reversible oxidation and reduction processes could be observed at $\sim +0.9$ and -1.4 V, respectively. It was found that by replacing the fluorine atoms with ethynyl moieties, oxidation potentials decreased by roughly 100 mV and reduction potentials shifted to more anodic potentials by roughly 230 mV. Interestingly, the dimeric compound **2.4** was found to have an oxidative event involving two successive redox processes, indicating that the two anthracene substituents are electronically independent of one another.

Another class of *N*-donor ligands that have been shown as potential BODIPY alternatives are BF_2 formazanates (**2.5**). This family of compounds has been shown to exhibit readily tunable spectroscopic and electrochemical properties while being synthesized in high yields.^{7,8}



2.5

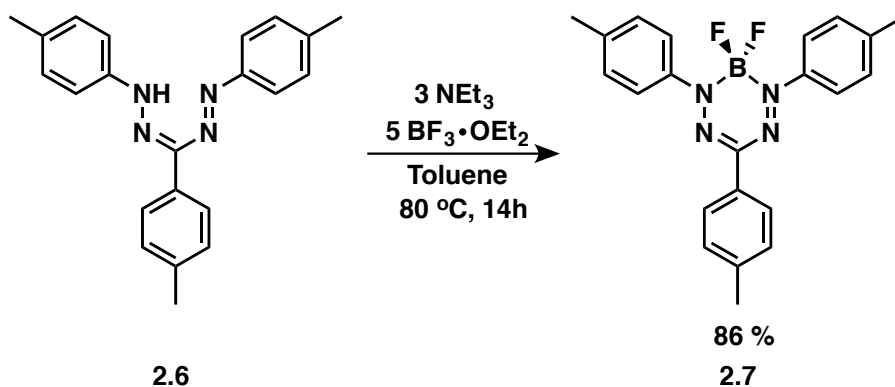


Increasing electronic delocalization at the *N*-aryl substituents (R^1 and R^5) has been shown to red-shift the absorption and emission maxima of these compounds, while varying electron withdrawing and electron donating substituents at these positions has been shown to drastically affect the rich redox chemistry that these complexes exhibit. While much work has been done exploring the unique properties of BF_2 formazanates, structural modification has not been explored at the boron centre. Chapter 2 presents the synthesis and characterization of the first reported alkynyl-substituted boron formazanate complexes using an adapted synthetic protocol previously reported for BODIPY-based systems. The spectroscopic, electrochemical and structural effects of these substitutions on the boron centre will be explored.

2.2 Results & Discussion

2.2.1 Synthesis of Alkynyl-Substituted Boron Formazanate Complexes

Tri-*p*-tolylformazan (**2.6**) was synthesized according to a previously published procedure,⁹ and exhibited a characteristic NH shift in its ^1H NMR spectrum at 15.42 ppm (Figure 2.1). BF_2 formazanate complex **2.7** was synthesized from the parent formazan **2.6** by heating at 80 °C in a toluene solution containing excess $\text{BF}_3 \cdot \text{OEt}_2$ and NEt_3 for 14 h under inert atmosphere (Scheme 2.1). The resulting BF_2 complex was synthesized in 86% yield.



Scheme 2.1. Synthesis of tri-*p*-tolyl BF₂ formazanate complex **2.7**.

The formation of compound **2.7** was accompanied by a colour change from red to deep purple (*vide infra*) and confirmed by ¹H NMR spectroscopy including the loss of the diagnostic NH resonance (Figures 2.1 & 2.2). In addition, a 1:1:1:1 quartet in the ¹⁹F NMR spectrum (Figure 2.3a) is observed as a result of coupling to ¹¹B with a spin of 3. Interestingly, a fraction of a septet can also be observed in the baseline of the ¹⁹F NMR spectrum (Figure 2.3a) with an intensity roughly 20% of the major 1:1:1:1 quartet. This is a result of coupling to the ¹⁰B isotope with a spin of 3/2, with the relative intensity resulting from a 20% isotopic abundance. Finally, a 1:2:1 triplet observed in the ¹¹B NMR spectrum (Figure 2.3b) as a result of coupling to two fluorine atoms also provides evidence for the incorporation of the BF₂ functionality into the formazan.

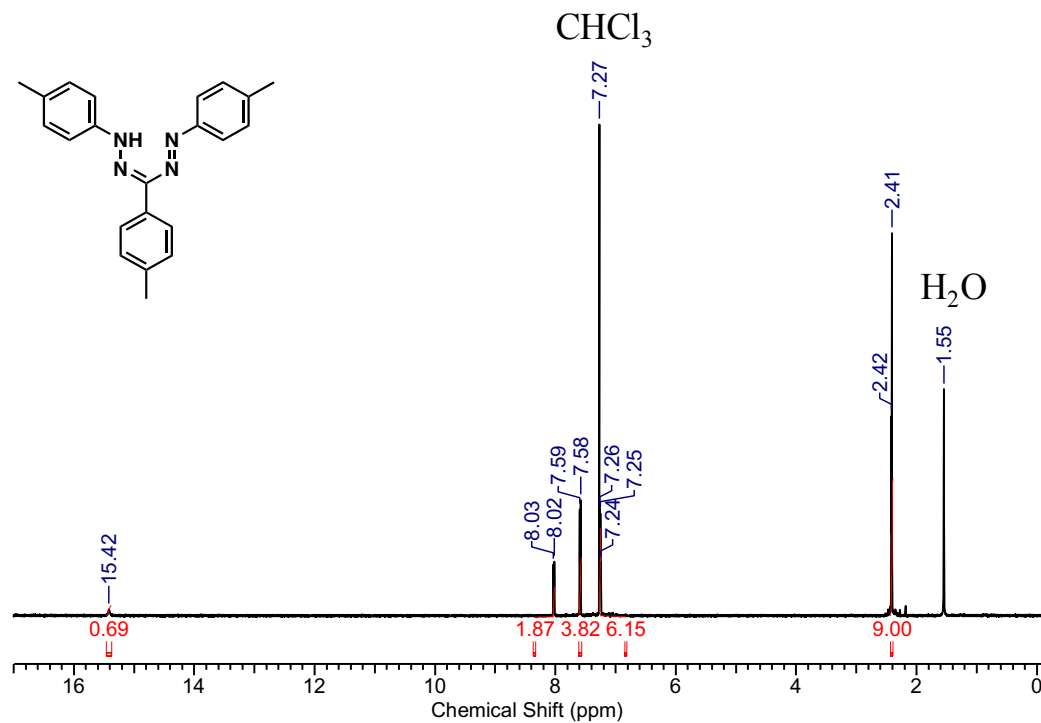


Figure 2.1. ^1H NMR spectrum of compound 2.6 in CDCl_3 .

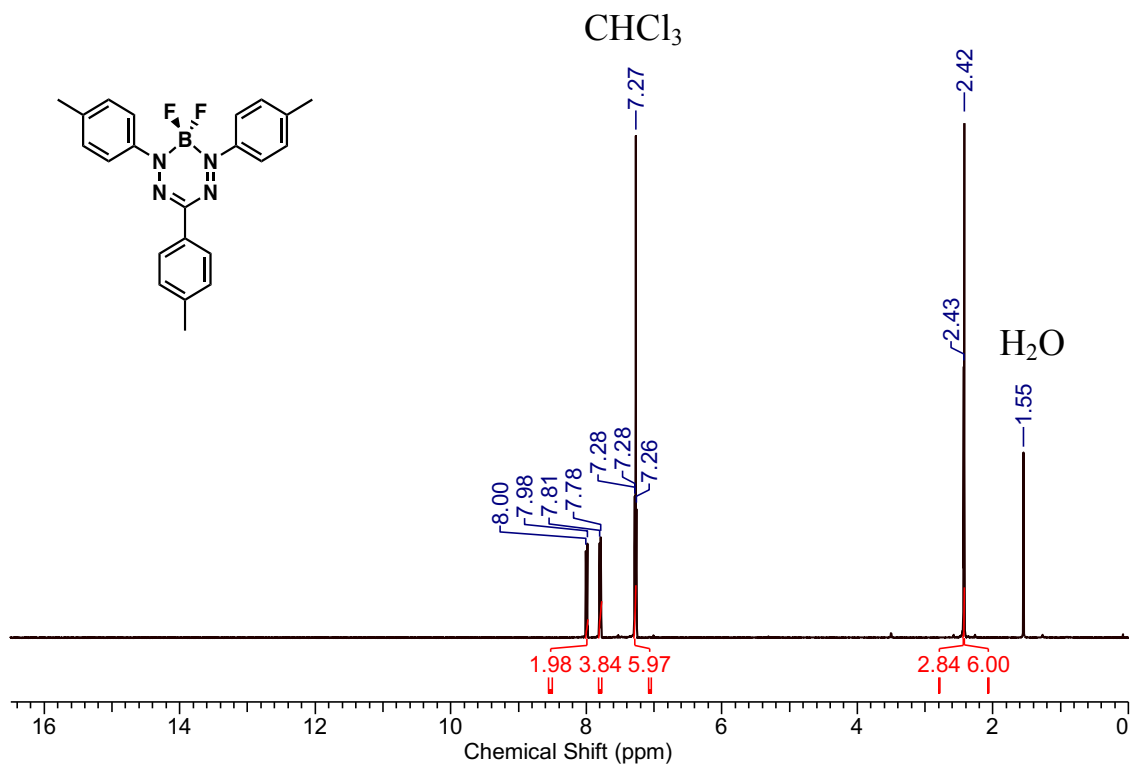


Figure 2.2. ^1H NMR spectrum of compound 2.7 in CDCl_3 .

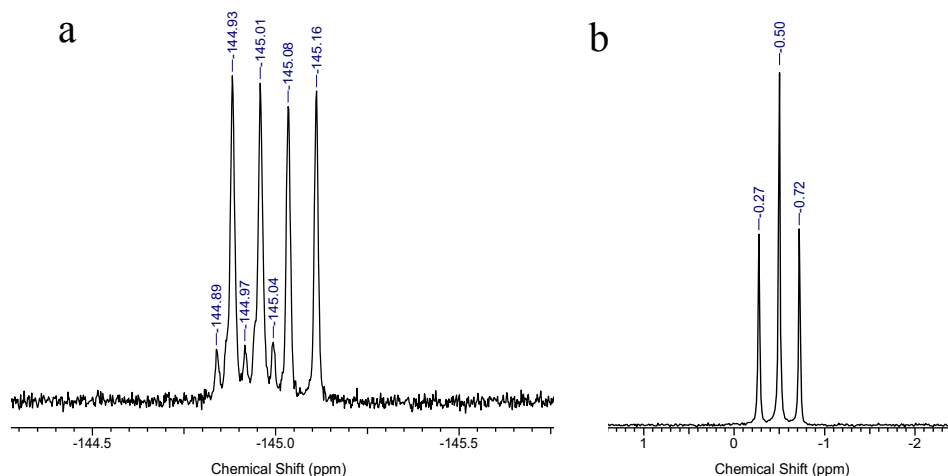
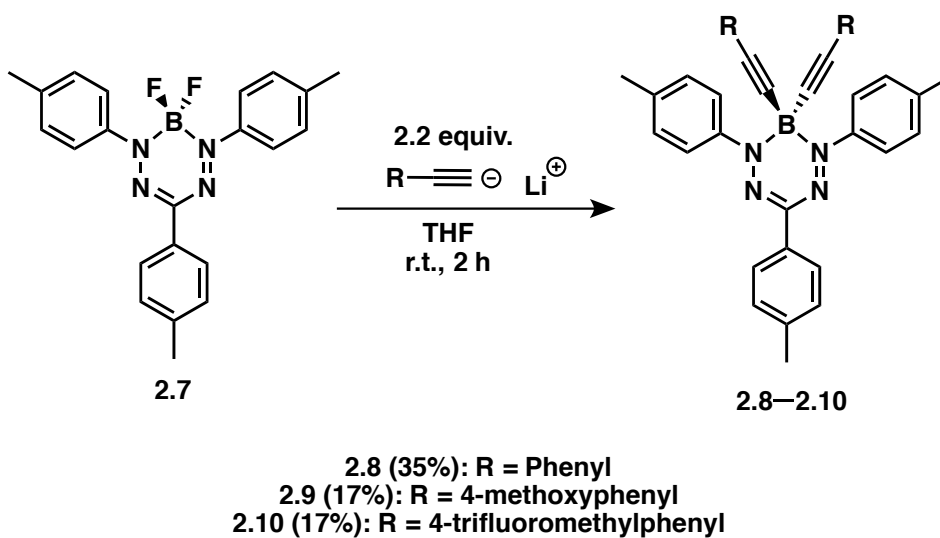


Figure 2.3. ^{19}F (a) and ^{11}B (b) NMR spectra of compound **2.7** recorded in CDCl_3 .

Upon isolating BF_2 complex **2.7**, a series of alkyne-substituted boron-containing formazanate complexes were synthesized by first dissolving 2.2 equiv. of the corresponding terminal acetylene in dry THF, cooling to $-78\text{ }^\circ\text{C}$ and stirring for 30 min (Scheme 2.2). 2.2 equiv. of $n\text{-BuLi}$ was then added dropwise and the solution was stirred at $-78\text{ }^\circ\text{C}$ for 1 h, warmed to room temperature, and stirred for an additional 30 min. Separately, a solution of **2.7** dissolved in dry THF was stirred for 15 min at room temperature. The lithiated terminal acetylene was then added dropwise to the solution of compound **2.7** in THF and the resulting solution was stirred for 2 h.



Scheme 2.2. Synthesis of alkyne-substituted boron formazanate complexes **2.8–2.10**.

The formation of complexes **2.8–2.10** was accompanied by colour changes from deep purple to red/orange for **2.8**, red/brown for **2.9** and orange/brown for **2.10** upon the addition of the acetylene/*n*-BuLi solution to **2.7**. The formation of **2.8** and **2.9** was accompanied by a disappearance of the 1:1:1:1 quartet in the corresponding ^{19}F NMR spectrum as well as the disappearance of the 1:2:1 triplet and appearance of a broad singlet in the ^{11}B NMR spectrum (Figures A1.2–1.7). The formation of **2.10** was accompanied by a disappearance of the 1:1:1:1 quartet and appearance of a singlet in the ^{19}F NMR spectrum at -62.8 ppm attributed to the CF_3 group, as well as the disappearance of the 1:2:1 triplet and appearance of a broad singlet in the ^{11}B NMR spectrum (Figures A1.3, A1.6, A1.10). Further supporting the formation of these compounds was a diagnostic signal in each of their IR spectra indicating the presence of an internal alkyne functionality at roughly 2186 cm^{-1} (Figure 2.4, Table 2.1).

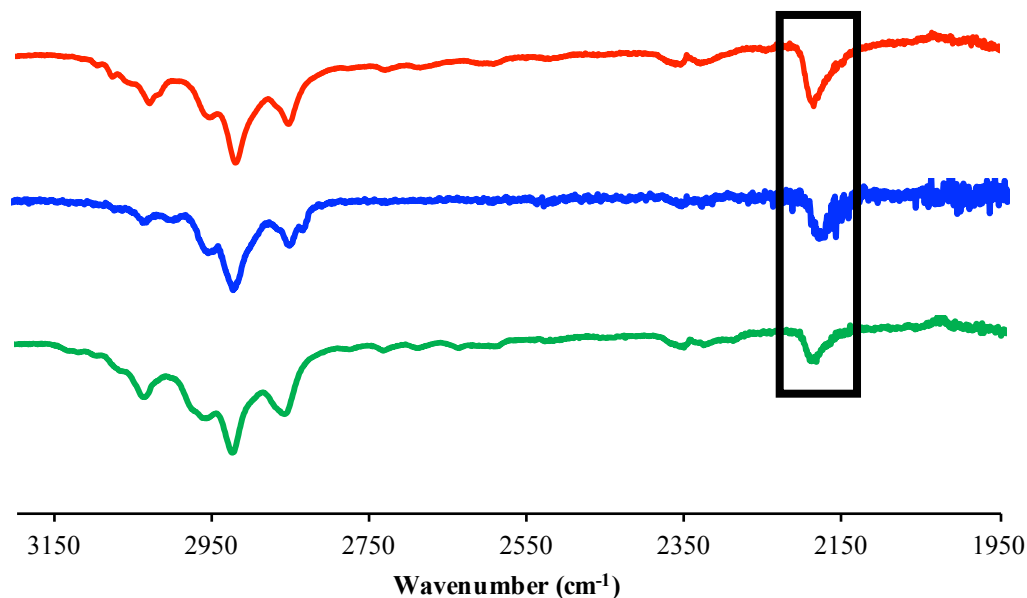


Figure 2.4. IR spectra of compounds **2.8** (red), **2.9** (blue) and **2.10** (green). Black box indicates the internal alkyne stretch.

Table 2.1. IR stretches for the internal alkyne of compounds **2.8–2.10**.

| Compound | Wavenumber (cm ⁻¹) |
|-------------|--------------------------------|
| 2.8 | 2186 |
| 2.9 | 2189 |
| 2.10 | 2188 |

2.2.2 X-Ray Crystallography

Single crystals for X-ray diffraction studies were grown by slow vapour diffusion of hexanes into a saturated THF solution (**2.7**) and hexanes into a saturated CH₂Cl₂ solution (**2.3**) (Figure 2.7). The solid-state structures show that the boron atoms are four-coordinate and adopt a tetrahedral geometry. They also show a delocalized formazanate backbone with all C-N and N-N bond lengths between those of typical single and double bonds (Table 2.4).¹⁰ The C-N bond lengths for **2.7** and **2.8** fall between 1.3385(8) and 1.346(3) Å, while typical C-N single and double bonds are 1.47 and 1.29 Å, respectively. The N-N bonds lengths for **2.7** and **2.8** fall between 1.3028(7) and 1.3136(3), while typical N-N single and double bonds are 1.45 and 1.25 Å, respectively. Complex **2.7** is relatively planar, with the boron atom displaced by 0.094 Å relative to the formazanate backbone, while the boron atom of **2.8** is further displaced by 0.713 Å, as a result of much larger substituents bound to the boron centre. The 1,5-aryl substituents in complex **2.7** are slightly twisted with respect to the formazanate backbone, with the angle between the N1-N2-N3-N4 plane and the plane defined by the *N*-aryl substituents being 4.51 and 8.48°. Complex **2.8** exists in a ‘dragonfly’ conformation where the dihedral angles between the 1,5-aryl substituents and formazanate backbone are significantly more twisted, with angles ranging from 54.9 to 60.6°. The B-N bonds in complex **2.8** are slightly longer than those of complex **2.7**, with bond lengths of 1.560(9) and 1.566(1) Å for **2.7** and 1.573(3) and 1.575(4) Å for **2.8**, indicating the boron atom of the parent BF₂ complex is more strongly bound by the formazanate backbone.

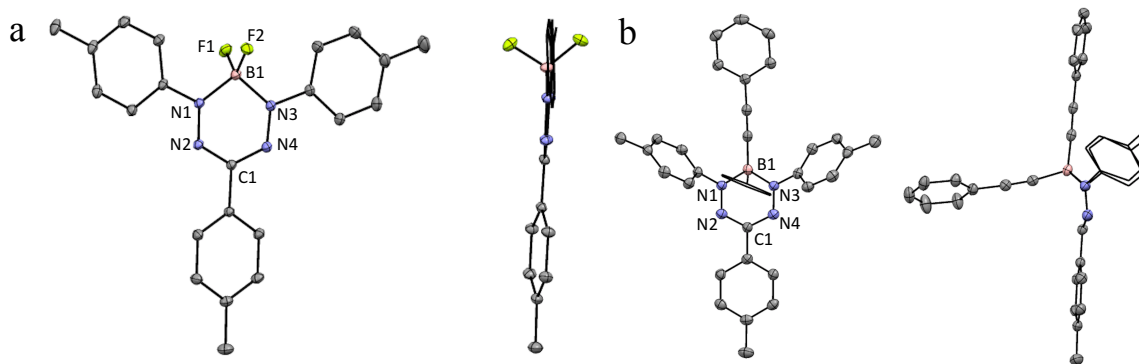


Figure 2.5. Top-view and side-view of the solid-state structures of a) **2.7** and b) **2.8**. Thermal ellipsoids are shown at 50% probability and hydrogen atoms are removed for clarity. Substituents at the boron centre in the side-view of b) have been converted to wireframe for clarity.

Table 2.2. Selected bond lengths (Å) and bond angles (°) of compounds **2.7** and **2.8**.

| | 2.7 | 2.8 |
|---------------------------------|------------|--------------|
| B1-N1 | 1.566(1) | 1.575(4) |
| B1-N3 | 1.560(9) | 1.573(3) |
| N1-N2 | 1.3037(7) | 1.312(3) |
| N3-N4 | 1.3028(7) | 1.316(3) |
| C1-N2 | 1.3417(8) | 1.346(3) |
| C1-N4 | 1.3385(8) | 1.344(3) |
| Dihedral Angles ^a | 4.51, 8.48 | 54.92, 60.60 |
| Boron Displacement ^b | 0.094 | 0.713 |

^aThe angle (°) between the *N*-aryl substituents and the N₄ plane of the formazanate backbone. ^bDistance (Å) between B₁ and the plane defined by the four N atoms.

2.2.3 UV-Visible Absorption Spectroscopy

The UV-Visible absorption spectra of compounds **2.7–2.10** are shown in Figure 2.5 and summarized in Table 2.2. Compounds **2.7–2.10** absorb in the visible region of the electromagnetic spectrum, however there is no substantial difference in the λ_{\max} values between compounds **2.8–2.10**, although compounds **2.8–2.10** exhibit a slight blue-shift (11–13 nm) relative to the parent BF₂ (**2.7**). The transitions may be assigned as $\pi \rightarrow \pi^*$ transitions, as their energies and intensities closely match reported transitions of previously synthesized BF₂ formazanate complexes.^{9,11}

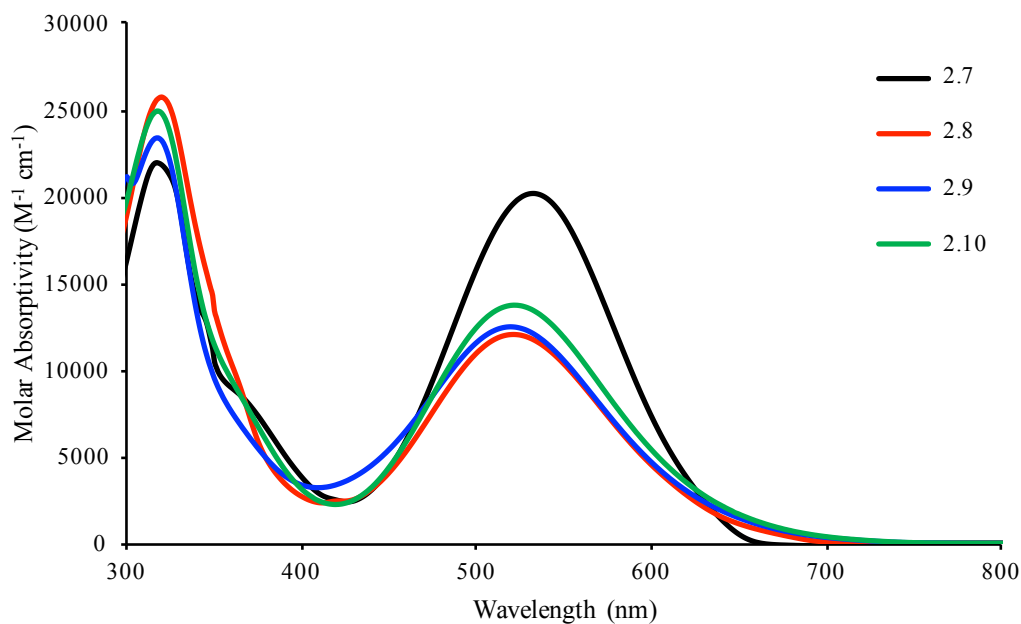


Figure 2.6. UV-Visible absorption spectra of compounds **2.7–2.10** recorded for degassed 10 μM toluene solutions.

None of the compounds studied exhibited any detectable fluorescence, likely due to non-radiative vibrational and rotational decay pathways relating to the 3-phenyl substituent, which agrees with previous reports.⁷ Interestingly, a small solvatochromic effect (10–17 nm shift) is observed as the λ_{max} values of the compounds blue-shift in more polar solvents, moving from toluene to CH_3CN , indicating a degree of charge transfer.

Table 2.3. Spectroscopic properties of complexes **2.7–2.10**.

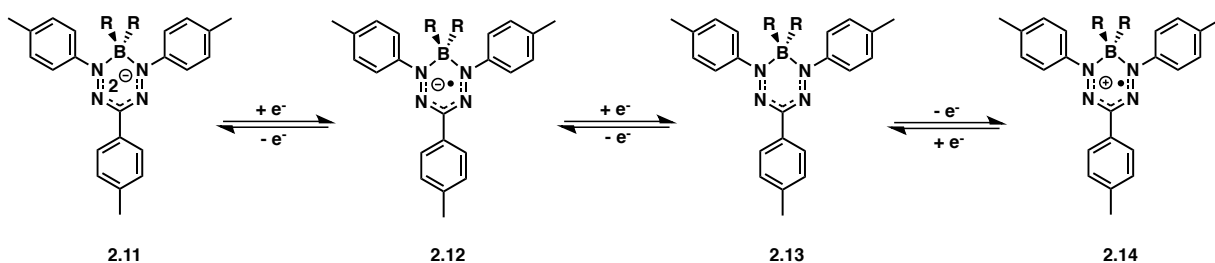
| Compound | Solvent | λ_{max}^a , nm, (ϵ , M ⁻¹ cm ⁻¹) |
|-------------|---------------------------------|--|
| 2.7 | CH ₃ CN | 251 (20 350), 313 (22 700), 522 (21 500) |
| | THF | 265 (21 250), 315 (21 500), 529 (19 550) |
| | CH ₂ Cl ₂ | 253 (22 450), 318 (27 925), 529 (27 350) |
| | Toluene | 317 (21 900), 532 (20 200) |
| 2.8 | CH ₃ CN | 257 (22 900), 312 (20 950), 504 (10 750) |
| | THF | 260 (6650), 314 (30 100), 517 (16 600) |
| | CH ₂ Cl ₂ | 260 (23 070), 316 (35 050), 517 (19 200) |
| | Toluene | 320 (25 700), 521 (12 000) |
| 2.9 | CH ₃ CN | 263 (35 750), 313 (28 500), 504 (12 850) |
| | THF | 262 (39 950), 313 (28 400), 516 (14 200) |
| | CH ₂ Cl ₂ | 265 (44 850), 516 (15 550) |
| | Toluene | 317 (23 400), 519 (12 500) |
| 2.10 | CH ₃ CN | 263 (32 400), 312 (24 300), 506 (11 750) |
| | THF | 265 (33 150), 313 (25 100), 517 (12 500) |
| | CH ₂ Cl ₂ | 265 (36 050), 519 (12 650) |
| | Toluene | 317 (24 900), 521 (13 700) |

^aValues recorded for degassed 10 μM solutions.

2.2.4 Electrochemical Properties

The electrochemical properties of compounds **2.7–2.10** were explored using cyclic voltammetry and are summarized in Table 2.4. Experiments were performed in dry, degassed CH₂Cl₂ and the cyclic voltammograms are shown in Figure 2.6. Compounds **2.7–2.10** exhibited two ligand-centred reversible (or quasi-reversible) one-electron reduction waves relative to the ferrocene/ferrocenium redox couple. In this experiment, the neutral complex (**2.13**) is first reduced to form the radical anion (**2.12**) at the first half wave reduction potential (E°_{red1}), followed by a second reduction to form the dianion (**2.11**) at the second half wave reduction potential (E°_{pc}) (Scheme 2.3). In all

cases, the second reduction wave was found to become more chemically reversible as the scan rate increased. Compounds **2.7**, **2.8** and **2.10** also exhibited one ligand-centred reversible (or quasi-reversible) one-electron oxidation wave relative to the ferrocene/ferrocenium redox couple, while **2.9** exhibited an irreversible oxidation event. In this experiment, the neutral complex (**2.13**) is oxidized to form the radical cation (**2.14**) at the half wave oxidation potential (E°_{ox1}) (Scheme 2.3).



Scheme 2.3. Stepwise electrochemical reduction of neutral boron-containing formazanate complexes (**2.13**) to the corresponding radical anion (**2.12**) and radical dianion (**2.11**) oxidation of neutral boron-containing formazanate complexes (**2.13**) to the corresponding radical cation (**2.14**).

Table 2.4. Summary of the electrochemical properties of compounds **2.7–2.10**.^a

| Compound | E°_{red1} (V) | E°_{red2} (V) ^b | E°_{ox1} (V) |
|-------------|-------------------------------|--|------------------------------|
| 2.7 | -1.04 | -1.99 | 1.03 |
| 2.8 | -1.18 | -2.03 | 0.83 |
| 2.9 | -1.21 | -2.12 | 0.86 ^c |
| 2.10 | -1.14 | -2.01 | 0.89 |

^aCyclic voltammograms were recorded in dry, degassed CH_2Cl_2 containing ~ 1 mM analyte and 0.1 M $[\text{nBu}_4\text{N}][\text{PF}_6]$ as a supporting electrolyte at a scan rate of 250 mV s^{-1} . Cyclic voltammograms of compounds **2.7–2.10** were referenced internally against the ferrocene/ferrocenium redox couple. ^bReduction peaks are not reversible and the values listed are of the maximum cathodic current. ^cOxidation peak is not reversible, and the value listed is of the maximum anodic current.

Relative to the parent BF₂ (**2.7**), compounds **2.8–2.10** were found to be more difficult to reduce and easier to oxidize with no fluorine atoms present. A trend may be observed when comparing compounds **2.8–2.10**, as the data suggests **2.10** is the easiest to reduce ($E^{\circ}_{\text{red1}} = -1.14$, $E^{\circ}_{\text{pc}} = -2.03$), followed by **2.8** ($E^{\circ}_{\text{red1}} = -1.18$, $E^{\circ}_{\text{pc}} = -2.01$), with compound **2.9** being the most difficult to reduce ($E^{\circ}_{\text{red1}} = -1.21$, $E^{\circ}_{\text{pc}} = -2.12$) (Table 4). These results may be rationalized by considering the substituents bound to the phenylacetylene moiety. Compound **2.10** contains an electron withdrawing CF₃ substituent at the *para* position, making it slightly easier to reduce relative to compound **2.9** bearing the electron donating OMe substituent at the *para* position, while compound **2.8** lies between as it contains a hydrogen atom at the *para* position.

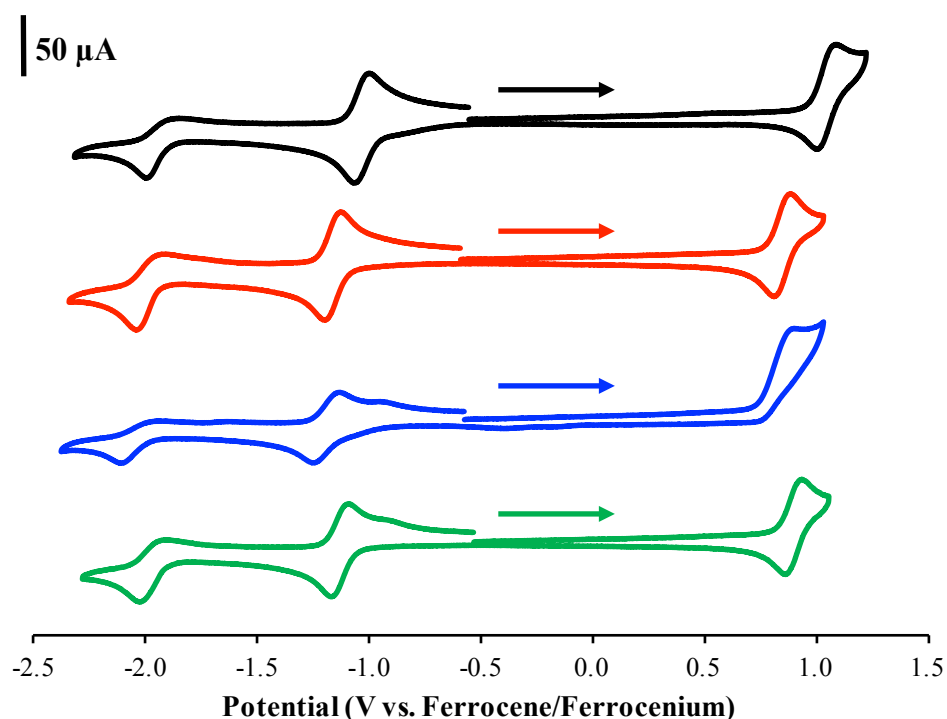


Figure 2.7. Cyclic voltammograms of compounds **2.7** (black), **2.8** (red), **2.9** (blue) and **2.10** (green) recorded in dry, degassed CH₂Cl₂ containing ~1 mM analyte and 0.1 M [nBu₄N][PF₆] as a supporting electrolyte at a scan rate of 250 mV s⁻¹. Arrow indicates the direction of scan.

2.3 Conclusions

The first reported alkynyl-substituted boron formazanate complexes **2.8–2.10** were synthesized using a series of lithiated terminal acetylenes. X-ray crystallography indicated that upon replacing the fluorine atoms at the boron centre, B-N bonds were elongated and all C-N and N-N bond lengths were found to be between those of typical single and double bonds, indicating a significant degree of electronic delocalization. Significant twisting of the *N*-aryl substituents on the formazanate backbone was observed as a result of the increased steric bulk at the boron centre, with complex **2.8** existing in a ‘dragonfly’ conformation where the dihedral angles between the 1,5-aryl substituents and formazanate backbone ranged from 54.9 to 67.9°. IR spectra confirmed the presence of an alkyne functionality at 2186–2189 cm⁻¹ for compounds **2.8–2.10**. Compounds **2.8–2.10** were found to absorb within the visible region of the electromagnetic spectrum and were also found to be non-emissive. Compounds **2.8–2.10** exhibited a slight blue-shift in the UV-Visible spectrum relative to the parent BF₂ complex **2.7** and a small solvatochromic effect (10–17 nm shift) moving from toluene to CH₃CN. Cyclic voltammetry demonstrated that complexes **2.8–2.10** were redox active and exhibited two quasi-reversible one-electron reduction processes and one quasi-reversible oxidation process relative to the ferrocene/ferrocenium redox couple. Electrochemical data also suggested compound **2.10** was the easiest to reduce as a result of the electron withdrawing CF₃ at the *para* position of the phenyl substituent while compound **2.9** was the most difficult to reduce as a result of the electron donating OMe at the *para* position of the phenyl substituent.

2.4 Experimental

2.4.1 General Considerations

Solvents were obtained from Caledon Laboratories, dried using an Innovative Technologies Inc. solvent purification system, collected under vacuum, and stored under an N₂ atmosphere over 4 Å molecular sieves. All other reagents were purchased from Sigma Aldrich, Alfa Aesar or TCI America and used as received. Formazan **2.6** was synthesized according to a published procedure.⁹ NMR spectra were recorded on a Bruker 400 MHz NMR spectrometer, 400 MHz Varian INova NMR spectrometer, or 600 MHz Varian Inova NMR spectrometer. ¹H NMR spectra were recorded in CDCl₃ and referenced against residual protonated solvent at 7.27 ppm. ¹³C{¹H} NMR spectra were referenced to CDCl₃ at 77.0 ppm. ¹¹B NMR spectra were referenced internally to BF₃•OEt₂ at 0 ppm. ¹⁹F NMR spectra were referenced internally to CFCl₃ at 0 ppm. Mass spectra were recorded in positive-ion mode using a high-resolution Finnigan MAT 8200 spectrometer. UV-Vis absorption spectra were recorded using a Cary 5000 Scan instrument using standard quartz cells (1 cm path length) with a scan range of 200 to 800 nm. Samples were dissolved in spectroscopic grade solvents to obtain various concentrations. The background was subtracted from each spectrum and the solvent used for each experiment is indicated. Emission spectra were recorded using a Photon Technology International QM-4 SE spectrofluorometer. FT-IR spectra were recorded using a Perkin Elmer Spectrum Two FT-IR spectrometer.

2.4.2 X-ray Crystallography Methods

Single crystals suitable for X-ray diffraction studies were grown by slow vapour diffusion of hexanes into a saturated THF solution (**2.7**) and hexanes into a saturated solution of CH₂Cl₂ (**2.8**) and were analyzed by Ryan Maar. Samples were mounted on a MiTeGen polyimide micromount with a small amount of Paratone *N* oil. X-ray measurements were made on a Bruker Kappa Axis Apex2 diffractometer or Nonius KappaCCD Apex2 diffractometer at a temperature of 110 K. The unit cell dimensions

of **2.7** were determined from a symmetry constrained fit of 9632 reflections with $5.06^\circ < 2\theta < 75.3^\circ$. The data collection strategy was a number of ω and φ scans which collected data up to 84.298° (2θ). The frame integration for both compounds was performed using SAINT.¹² The resulting raw data was scaled and absorption corrected using a multi-scan averaging of symmetry equivalent data using SADABS.¹³ The structures were solved by using a dual space methodology using the SHELXT program.¹⁴ All non-hydrogen atoms were obtained from the initial solution. The hydrogen atoms for complex **2.7** were introduced at idealized positions and were allowed to refine isotropically. The structural model was fit using full matrix least-squares based on F^2 . The calculated structure factors included corrections for anomalous dispersion from the usual tabulation. The structure was refined using the SHELXL program from the SHELX suite of crystallographic software.¹⁵ Graphic plots were produced using the Mercury program suite.¹⁶

Initial indexing of complex **2.8** indicated that the sample crystal was non-merohedrally twinned. The twin law was determined to be:

$$\begin{array}{ccc} 0.98961 & -0.03862 & -0.00825 \\ 0.04331 & 1.00934 & 0.01391 \\ 0.00875 & -0.02604 & 0.99903 \end{array}$$

which represents a -2.586° rotation about the $[-2 \ -1 \ 7]$ (reciprocal cell) or $[-11 \ -6 \ 15]$ (direct cell). The twin fraction was included as an adjustable parameter. The unit cell dimensions were determined from a symmetry constrained fit of 3050 reflections with $5.84^\circ < 2\theta < 51.24^\circ$. The data collection strategy was a number of ω and φ scans which collected data up to 56.776° (2θ). The frame integration was performed using SAINT.¹² The resulting raw data was scaled and absorption corrected using a multi-scan averaging of symmetry equivalent data using TWINABS.¹⁷ The structure was solved by using a dual space methodology using the SHELXT program.¹⁴ All non-hydrogen atoms were obtained from the initial solution. The hydrogen atoms were introduced at idealized positions and were allowed to refine isotropically. The twin fraction refined

to a value of 0.29480(115). The structural model was fit to the data using full matrix least-squares based on F^2 . The calculated structure factors included corrections for anomalous dispersion from the usual tabulation. The structure was refined using the SHELXL program from the SHELX suite of crystallographic software.¹⁵ Graphic plots were produced using the Mercury program suite.¹⁶ See Table 2.5 for additional crystallographic data.

Table 2.5. X-ray diffraction data collection and refinement details for compounds **2.7** and **2.8**.

| | 2.7 | 2.8 |
|---------------------------------------|--|---|
| Formula | C ₂₂ H ₂₁ BF ₂ N ₄ | C ₃₈ H ₃₁ BN ₄ |
| Formula Weight (g mol ⁻¹) | 390.24 | 554.48 |
| Crystal Dimensions (mm) | 0.363 × 0.195 × 0.155 | 0.223 × 0.186 × 0.101 |
| Crystal Colour and Habit | purple prism | red plate |
| Crystal System | monoclinic | triclinic |
| Space Group | P 2 ₁ /c | P -1 |
| Temperature, (K) | 110 | 110 |
| <i>a</i> , (Å) | 12.335(3) | 9.863(2) |
| <i>b</i> , (Å) | 12.866(3) | 10.432(2) |
| <i>c</i> , (Å) | 12.803(2) | 15.125(4) |
| α, (°) | 90 | 92.766(11) |
| β, (°) | 110.343(7) | 91.008(12) |
| γ, (°) | 90 | 103.191(9) |
| <i>V</i> , (Å ³) | 1905.0(7) | 1512.7(6) |
| <i>Z</i> | 4 | 2 |
| ρ (g cm ⁻³) | 1.361 | 1.217 |
| λ, Å, (MoKα) | 0.71073 | 0.71073 |
| μ, (cm ⁻¹) | 0.095 | 0.072 |
| Diffractometer Type | Bruker Kappa Axis Apex2 | Bruker Kappa Axis Apex2 |
| R ₁ | 0.0433 | 0.0670 |
| ωR ₂ | 0.1198 | 0.1511 |
| R ₁ (all data) | 0.0661 | 0.1425 |
| ωR ₂ (all data) | 0.1336 | 0.1851 |
| GOF | 1.047 | 1.025 |

$$R_1 = \frac{\sum(|F_o| - |F_c|)}{\sum F_o}$$

$$\omega R_2 = \left[\frac{\sum(\omega(F_o^2 - F_c^2)^2)}{\sum(\omega F_o^4)} \right]^{1/2}$$

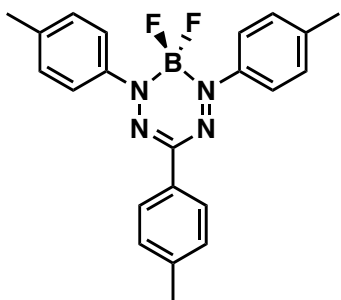
$$GOF = \left[\frac{\sum(\omega(F_o^2 - F_c^2)^2)}{(\text{No. of reflns.} - \text{No. of params.})} \right]^{1/2}$$

2.4.3 Electrochemical Methods

Cyclic voltammetry experiments were performed using a Bioanalytical Systems Inc. (BASi) Epsilon potentiostat and analyzed using BASi Epsilon software. Typical electrochemical cells consisted of a three-electrode setup including a glassy carbon working electrode, platinum counter electrode, and silver *pseudo* reference electrode. Experiments were run at 250 mV s^{-1} in degassed CH_2Cl_2 solutions of the analyte ($\sim 1 \text{ mM}$) and electrolyte ($0.1 \text{ M } [n\text{Bu}_4\text{N}][\text{PF}_6]$). Cyclic voltammograms were internally referenced against the ferrocene/ferrocenium redox couple ($\sim 1 \text{ mM}$ internal standard) and corrected for internal cell resistance using the BASi Epsilon software.

2.4.4 Synthetic Procedures

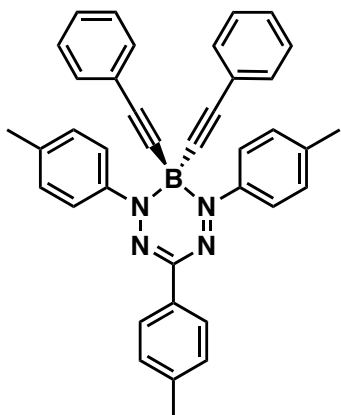
BF₂ Complex 2.7



Under N_2 , formazan **2.6** (1.0 g, 3.0 mmol) was dissolved in dry toluene (100 mL). NEt_3 (1.4 mL, 10 mmol) was then added dropwise and the solution was stirred for 5 mins. $\text{BF}_3 \cdot \text{OEt}_2$ (1.9 mL, 15 mmol) was then added, and the solution was heated at $80 \text{ }^\circ\text{C}$ for 18 h. The solution changed from dark red to dark purple during this time. The solution was then cooled to room temperature and H_2O (20 mL) was added to quench any reactive boron-containing compounds. The solution was then washed with deionized H_2O ($3 \times 50 \text{ mL}$), dried over MgSO_4 , gravity filtered and concentrated *in vacuo*. The resulting residue was purified by flash chromatography (CH_2Cl_2 , neutral alumina) to afford the BF_2 complex **2.2** as a dark purple microcrystalline solid. Yield = 0.98 g (86%). ^1H NMR (399.8 MHz, CDCl_3) δ 7.99 (d, $^3J_{\text{HH}} = 8 \text{ Hz}$, 2H, Aryl CH), 7.80 (d, $^3J_{\text{HH}} = 8 \text{ Hz}$, 4H, Aryl CH), 7.29–7.26 (m, 6H, Aryl CH), 2.43 (s, 3H, CH_3), 2.42 (s, 6H, CH_3). ^{19}F NMR (376.1 MHz, CDCl_3) δ -145.0 (q, $^1J_{\text{FB}} = 30 \text{ Hz}$). ^{11}B NMR (128.3 MHz, CDCl_3) δ 0.5 (t, $^1J_{\text{BF}} = 29 \text{ Hz}$). $^{13}\text{C}\{^1\text{H}\}$ NMR (101.6 MHz, CDCl_3) δ 149.0, 141.7, 140.0, 139.1, 131.1, 129.6, 129.4, 125.4, 123.2, 21.34, 21.32. FT-IR (ATR, cm^{-1}) 3033, 2916, 2858, 1909, 1605, 1506, 1504, 1414, 1377, 1350, 1317, 1302. UV-Vis (Toluene):

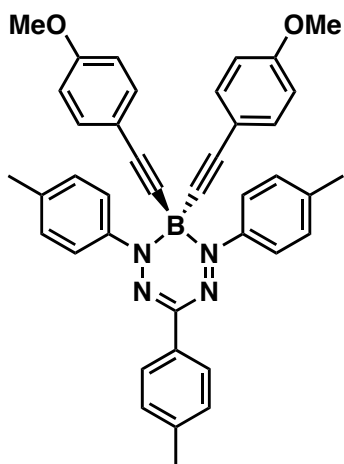
$\lambda_{\max} = 317 \text{ nm}$ ($\epsilon = 21\,900 \text{ M}^{-1} \text{ cm}^{-1}$), 532 nm ($\epsilon = 20\,200 \text{ M}^{-1} \text{ cm}^{-1}$). ESI-HRMS (+ve mode) calculated for $[\text{C}_{22}\text{H}_{21}\text{BF}_2\text{N}_4]^+$: 390.1827, found 390.1841, difference: +3.6 ppm.

Phenylacetylene Complex 2.8



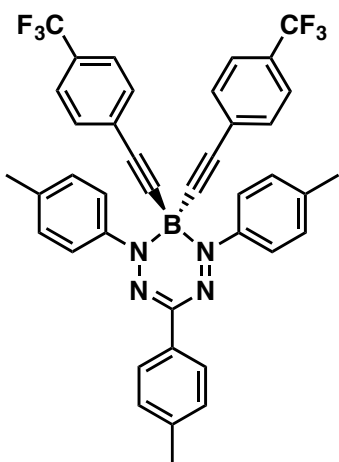
Under N_2 , phenylacetylene (0.13 mL, 1.1 mmol) was dissolved in dry THF (5 mL) in a greaseless Schlenk flask, cooled to $-78 \text{ }^\circ\text{C}$, and stirred for 30 min. *n*-BuLi (1.6 M, 0.45 mL, 1.1 mmol) was added dropwise over 5 min and the solution was stirred for 1 h. The solution was then brought to room temperature, stirred for 30 min and added dropwise to a second greaseless Schlenk flask containing BF_2 complex **2.7** (0.20 g, 0.50 mmol) dissolved in THF (10 mL). The solution was stirred for 2 h at room temperature and gradually changed colour from deep purple to red/orange. The solution was then quenched with deionized H_2O (7 mL), extracted with Et_2O (25 mL) and washed with deionized H_2O ($3 \times 50 \text{ mL}$), dried over MgSO_4 , gravity filtered and concentrated *in vacuo*. The resulting residue was purified by flash chromatography (2:1 hexanes: CH_2Cl_2 , silica gel) to afford complex **2.3** as a red/orange microcrystalline solid. Yield = 0.10 g (35%). ^1H NMR (599.5 MHz, CDCl_3) δ 8.01 (dm, 2H, $J = 6 \text{ Hz}$, Aryl CH), 7.90 (dm, 4H, $J_{\text{HH}} = 6 \text{ Hz}$, Aryl CH), 7.28–7.19 (m, 16H, Aryl CH), 2.43 (s, 3H, CH_3), 2.42 (s, 6H, CH_3). ^{11}B NMR (128.3 MHz, CDCl_3) δ -11.8 (s). $^{13}\text{C}\{^1\text{H}\}$ NMR (101.6 MHz, CDCl_3) δ 151.7, 143.3, 139.4, 138.7, 131.5, 131.3, 129.3, 128.5, 127.9, 127.5, 125.5, 125.2, 124.4, 99.9, 77.2, 21.38, 21.35. FT-IR (ATR, cm^{-1}) 3030, 2952, 2920, 2854, 2367, 2341, 2187, 1598, 1491, 1489, 1442, 1350, 1280. UV-Vis (Toluene): $\lambda_{\max} = 320 \text{ nm}$ ($\epsilon = 25\,700 \text{ M}^{-1} \text{ cm}^{-1}$), 521 nm ($\epsilon = 12\,000 \text{ M}^{-1} \text{ cm}^{-1}$). ESI-HRMS (+ve mode) calculated for $[\text{C}_{38}\text{H}_{31}\text{BN}_4]^+$: 554.2642, found 554.2651, difference: +1.6 ppm.

4-methoxyphenylacetylene Complex 2.9



Under N₂, 4-methoxyphenylacetylene (0.22 g, 1.7 mmol) was dissolved in dry THF (5 mL) in a greaseless Schlenk flask, cooled to -78 °C, and stirred for 30 min. *n*-BuLi (1.6 M, 0.68 mL, 1.7 mmol) was added dropwise over 5 min and the solution was stirred for 1 h. The solution was then brought to room temperature and slowly changed from clear yellow to an opaque coffee-brown colour. The solution was stirred for 30 min, added dropwise to a second greaseless Schlenk flask containing BF₂ complex **2.7** (0.30 g, 0.8 mmol) dissolved in THF (10 mL) and stirred for an additional 2 h. The resulting solution gradually changed from deep purple to red and finally brown. The solution was then quenched with deionized H₂O (7 mL), extracted with Et₂O and washed with deionized H₂O (3 × 50 mL), dried over MgSO₄, gravity filtered and concentrated *in vacuo*. The resulting residue was purified by flash chromatography (toluene, silica gel) to afford complex **2.4** as a red/brown film. Yield = 0.08 g (17%). ¹H NMR (399.8 MHz, CDCl₃) δ 8.00 (dm, 2H, *J*_{HH} = 8 Hz, Aryl CH), 7.90 (dm, 4H, *J*_{HH} = 12 Hz, Aryl CH), 7.28–7.26 (m, 2H, Aryl CH), 7.23–7.21 (m, 4H, Aryl CH), 7.17–7.15 (m, 4H, Aryl CH), 6.73–6.71 (m, 4H, Aryl CH), 3.76 (s, 6H, OCH₃), 2.42 (s, 3H, CH₃), 2.41 (s, 6H, CH₃). ¹¹B NMR (128.3 MHz, CDCl₃) δ -11.8 (s). ¹³C {¹H} NMR (101.6 MHz, CDCl₃) δ 159.0, 151.7, 143.3, 139.2, 138.7, 132.9, 131.4, 129.2, 128.4, 125.6, 125.2, 116.8, 113.5, 99.7, 77.2, 55.2, 21.38, 21.35. FT-IR (ATR, cm⁻¹) 3038, 2956, 2926, 2854, 2189, 1605, 1508, 1464, 1441, 1355, 1282. UV-Vis (Toluene): λ_{max} = 317 nm (ε = 23 400 M⁻¹ cm⁻¹), 519 nm (ε = 12 500 M⁻¹ cm⁻¹). ESI-HRMS (+ve mode) calculated for [C₄₀H₃₅BN₄O₂]⁺: 614.2853, found 614.2879, difference: +4.2 ppm.

4-trifluoromethylphenylacetylene Complex 2.10



Under N_2 , 4-trifluoromethylphenylacetylene (0.28 mL, 1.7 mmol) was dissolved in dry THF (5 mL) in a greaseless Schlenk flask, cooled to $-78\text{ }^\circ\text{C}$, and stirred for 30 min. *n*-BuLi (1.6 M, 0.68 mL, 1.7 mmol) was added very slowly over 5 min and the solution was stirred for 1 h. While stirring, the solution changed from clear yellow to cloudy white. The solution was held at $-78\text{ }^\circ\text{C}$ and then added dropwise to a second greaseless Schlenk flask containing BF_2 complex **2.7** (0.3 g, 0.8 mmol) dissolved in THF (10 mL) at $-78\text{ }^\circ\text{C}$. The deep purple solution slowly turned orange/brown as the solution was brought from $-78\text{ }^\circ\text{C}$ to room temperature and stirred for 2 h. The solution was then quenched with deionized H_2O (7 mL), extracted with Et_2O and washed with deionized H_2O ($3 \times 50\text{ mL}$), dried over $MgSO_4$, gravity filtered and concentrated *in vacuo*. The resulting residue was purified by flash chromatography (silica gel). The column was first flushed with hexanes (50 mL) to remove impurities, followed by toluene (50 mL) to afford complex **2.5** as a purple/brown film. Yield = 0.09 g (17%). 1H NMR (399.8 MHz, $CDCl_3$) δ 8.00 (dm, 2H, $J_{HH} = 8\text{ Hz}$, Aryl CH), 7.85 (dm, 4H, $J_{HH} = 8\text{ Hz}$, Aryl CH), 7.46 (dm, 4H, $J_{HH} = 8\text{ Hz}$, Aryl CH), 7.32–7.24 (m, 10H, Aryl CH), 2.43 (m, 9H, CH_3). ^{19}F NMR (376.1 MHz, $CDCl_3$) δ -62.8 (s). ^{11}B NMR (128.3 MHz, $CDCl_3$) δ -12.0 (s). $^{13}C\{^1H\}$ NMR (101.6 MHz, $CDCl_3$) δ 152.1, 143.1, 139.7, 139.1, 131.7, 130.9, 129.5, 129.4, 129.2, 128.6, 127.9, 125.5, 125.2, 124.9 (q, $^1J_{CF} = 16\text{ Hz}$), 122.6, 98.6, 77.2, 21.38, 21.36. FT-IR (ATR, cm^{-1}) 3043, 2976, 2926, 2872, 2188, 1926, 1615, 1506, 1405, 1320, 1278, 1263. UV-Vis (Toluene): $\lambda_{max} = 317\text{ nm}$ ($\epsilon = 24\ 900\text{ M}^{-1}\text{ cm}^{-1}$), 521 nm ($\epsilon = 13\ 700\text{ M}^{-1}\text{ cm}^{-1}$). ESI-HRMS (+ve mode) calculated for $[C_{40}H_{29}BF_6N_4]^+$: 690.2389, found 690.2403, difference: +2.0 ppm.

2.5 References

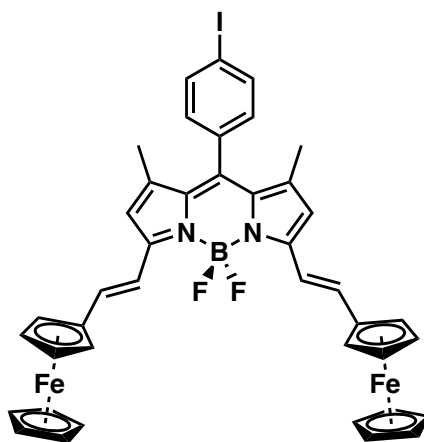
1. Loudet, A.; Burgess, K. *Chem. Rev.* **2007**, *107*, 4891–4932.
2. Wood, T. E.; Thompson, A. *Chem. Rev.* **2007**, *107*, 1831–1861.
3. Ulrich, G.; Ziesel, R.; Harriman, A. *Angew. Chem. Int. Ed.* **2008**, *47*, 1184–1201.
4. Goze, C.; Ulrich, G.; Ziesel, R. *J. Org. Chem.* **2007**, *72*, 313–322.
5. Sanchez-Carnerero, E. M.; Moreno, F.; Maroto, B. L.; Agarrabeitia, A. R.; Ortiz, M. J.; Vo, B. G.; Muller, G.; de la Moya, S. *J. Am. Chem. Soc.* **2014**, *136*, 3346–3349.
6. Goze, C.; Ulrich, G.; Ziesel, R. *Org. Lett.* **2006**, *8*, 4445–4448.
7. Barbon, S. M.; Reinkeluers, P. A.; Price, J. T.; Staroverov, V. N.; Gilroy, J. B. *Chem. Eur. J.* **2014**, *20*, 11340–11344.
8. Chang, M. C.; Roewen, P.; Travieso-Puente, R.; Lutz, M.; Otten, E. *Inorg. Chem.* **2015**, *54*, 379–388.
9. Gilroy, J. B.; McKinnon, S. D. J.; Koivisto, B. D.; Hicks, R. G. *Org. Lett.* **2007**, *9*, 4837–4840.
10. Haynes, W. M., CRC Handbook of Chemistry and Physics 96th Edition. Taylor & Francis Group: New York, **2015**.
11. Barbon, S. M.; Price, J. T.; Reinkeluers, P. A.; Gilroy, J. B. *Inorg. Chem.* **2014**, *53*, 10585–10593.
12. Bruker-AXS, *SAINT* version 2013.8, **2013**, Bruker-AXS, Madison, WI, 53711, USA.
13. Bruker-AXS, *SADABS* version 2012.1, **2012**, Bruker-AXS, Madison, WI 53711, USA.
14. Sheldrick, G. M. *Acta. Cryst.* **2015**, *A71*, 3–8.
15. Sheldrick, G. M. *Acta. Cryst.* **2015**, *C71*, 3–8.
16. Macrae, C. F.; Bruno, I. J.; Chisholm, J. A.; Edgington, P. R.; McCabe, P.; Pidcock, E.; Rodriguez-Monge, L.; Taylor, R.; van de Streek, J.; Wood, P. A. *J. Appl. Cryst.* **2008**, *41*, 466–470.

17. Bruker-AXS, *TWINABS* version 2012.1, **2012**, Bruker-AXS, Madison, WI, 53711, USA.

Chapter 3

3.1 Introduction

Upon the successful synthesis of alkynyl-substituted boron formazanate complexes described in Chapter 2, the focus was shifted toward employing the alkynyl functionality as a handle toward post-synthetic modifications and the incorporation of redox-active species. Redox-active molecular systems have seen widespread use in applications such as electrochemical and pH sensing.^{1,2,3} Interesting systems exhibiting these unique properties include redox-active BODIPYs containing ferrocene functionalities.^{4,5} For example, the Zhu group developed a ferrocene-containing BODIPY (**3.1**) that exhibited unique electrochromism and provided a handle for sensing.⁶

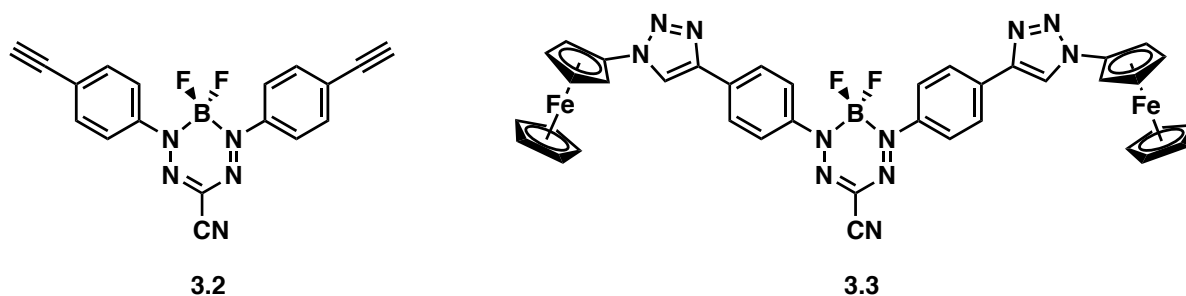


3.1

The authors took advantage of the electrochemical reversibility of ferrocene in order to modulate the electronics of the BODIPY core. Initially, UV-Vis absorption spectroscopy indicated complex **3.1** had a λ_{\max} value of 700 nm. Cyclic voltammetry revealed that oxidation of the ferrocene functionalities at roughly 0.5 V (vs. Ag/Ag⁺) was two distinct peaks (each corresponding to one-electron) at lower scan rates, indicating that the second ferrocene unit was more difficult to oxidize than the first as a result of this electronically conjugated system. A spectrochemical experiment was

then carried out where an oxidative potential of 0.7 V (vs. Ag/Ag⁺) was applied in order to oxidize both ferrocene moieties. UV-Vis absorption spectra displayed the λ_{max} of 700 nm slowly decreasing while a new λ_{max} was observed at 600 nm as the oxidation proceeded, corresponding to a colour change of the solution from deep blue to red. When a reduction potential was applied (0 V vs. Ag/Ag⁺), the solution returned to deep blue and the λ_{max} of 700 nm was regenerated, demonstrating the reversibility of the system. Interestingly, it was found that upon exposure of this BODIPY system to Cu²⁺ ions in a copper(II)perchlorate solution, the λ_{max} of 700 nm in the UV-Vis absorption spectrum decreased, with an appearance of a new peak at roughly 550 nm, producing similar results to the electrochemically oxidized UV-Vis spectrum. As a result, the unique electrochromic properties of this system allowed the authors to demonstrate the potential use of this BODIPY system in metal ion sensing.

The Gilroy group has also explored redox-active systems synthesized via Cu(I)-catalyzed alkyne-azide cycloaddition (CuAAC) chemistry in order to modify a fluorescent BF₂ formazanate (**3.2**) with a redox-active handle. A ferrocene-functionalized BF₂ formazanate (**3.3**) was synthesized via CuAAC with BF₂ formazanate **3.2** and ferrocenyl azide. UV-Vis absorption spectroscopy indicated complex **3.3** had a λ_{max} value of 569 nm and was non-emissive in solution. Cyclic voltammetry revealed an oxidation event of two coincident one-electron waves corresponding to the ferrocene units occurred at 0.21 V (vs. ferrocene/ferrocenium). Interestingly, the coincident appearance of the oxidation indicated that there was little communication between the ferrocene units and the BF₂ formazanate, likely as a result of the triazole ring. It was found that upon chemically oxidizing the ferrocene units of complex **3.3** with NOBF₄, absorption maxima in the UV-Vis were blue-shifted by roughly 20 nm and an increase in emission intensity was observed (to a maximum of $\Phi_{\text{F}} = 0.14$), showcasing this system as a potential redox sensor.

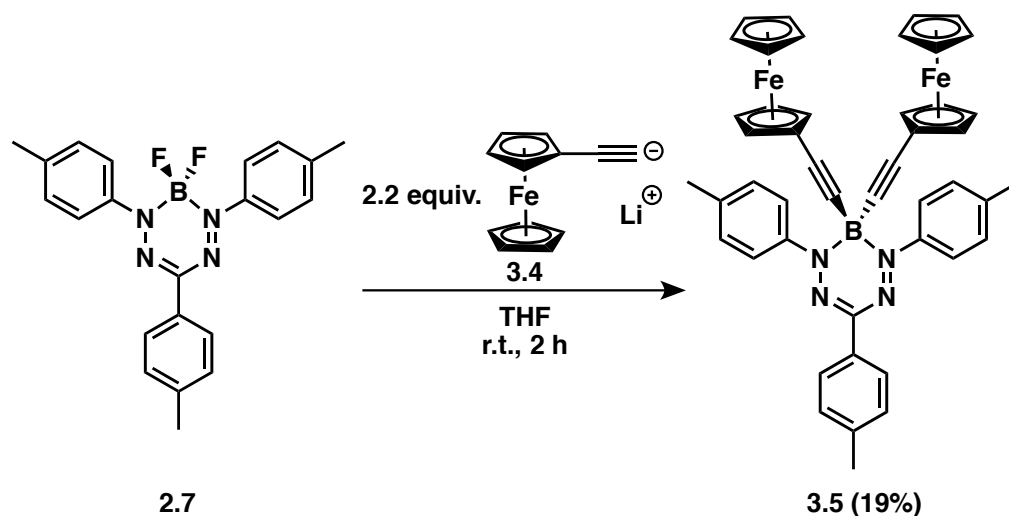


Chapter 3 presents the synthesis and characterization of a redox-active alkynyl-substituted boron formazanate complex, and explores the chemical oxidation and reduction of this system. It also explores the post-synthetic functionalization of a boron formazanate complex bearing a free terminal acetylene at the boron centre using CuAAC chemistry.

3.2 Results & Discussion

3.2.1 Synthesis of a Redox-Active Alkynyl-Substituted Boron Formazante Complex

A redox-active alkynyl-substituted boron formazanate complex was synthesized according to Scheme 3.1. First, a solution of **2.7** was dissolved in dry THF and stirred for 15 min at room temperature. Separately, 2.2 equiv. of ethynylferrocene (**3.4**) was dissolved in dry THF, cooled to $-78\text{ }^{\circ}\text{C}$ and stirred for 30 min. 2.2 equiv. of *n*-BuLi was then added dropwise and the solution was stirred at $-78\text{ }^{\circ}\text{C}$ for 1 h, warmed to room temperature and stirred for an additional 30 min. The lithiated terminal acetylene was then added dropwise to the solution of compound **2.7** in THF and the resulting solution was stirred for 2 h.



Scheme 3.1. Synthesis of redox-active boron formazanate complex **3.5**. Yield is indicated in brackets.

The formation of complex **3.5** was accompanied by a colour change from deep purple to red/orange upon the addition of the acetylene/*n*-BuLi solution to **2.7**, and the complex was isolated in 19% yield. The formation of **3.5** was accompanied by a disappearance of the 1:1:1:1 quartet in the ^{19}F NMR spectrum as well as the disappearance of the 1:2:1 triplet at -0.50 ppm due to loss of the fluorine atoms, and appearance of a broad singlet in the ^{11}B NMR spectrum at -11.8 ppm (Figures B1–B3). Further supporting the formation of this compound was a diagnostic signal in the IR spectrum at 2188 cm^{-1} indicating the presence of an alkyne functionality (Figure 3.1).

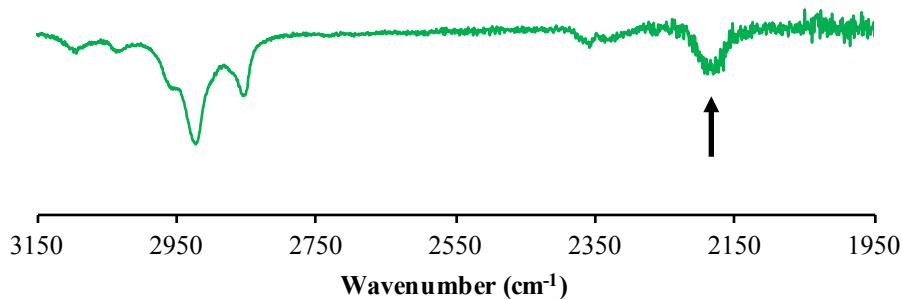


Figure 3.1. IR Spectrum of complex **3.5**. Arrow indicates the internal alkyne stretch at 2188 cm^{-1} .

3.2.2 X-ray Crystallography

Single crystals for X-ray diffraction studies were grown by slow vapour diffusion of pentane into a saturated CH_2Cl_2 solution (**3.5**) (Figure 3.2). Side views of the solid-state structures of the parent BF_2 complex (**2.7**) and phenylacetylene complex (**2.8**) from Chapter 2 (Figure 3.2a,b) are included for comparison.

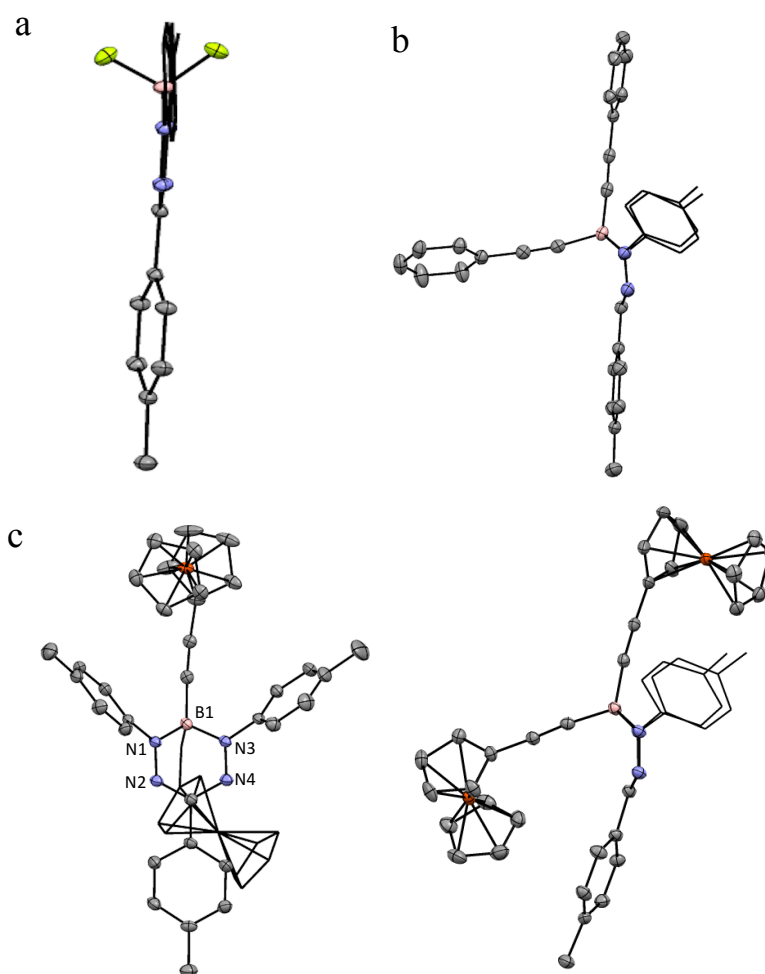


Figure 3.2. Side-view solid-state structures of a) **2.7**, b) **2.8**. Top-view and side-view solid-state structures of c) **3.5**. Thermal ellipsoids are shown at 50% probability and hydrogen atoms are removed for clarity. Some substituents in b) and c) have been converted to wireframe for clarity. a) and b) have been reproduced from Chapter 2 for comparison.

The solid-state structures show that the boron atoms are four-coordinate and adopt a tetrahedral geometry. They also show a delocalized formazanate backbone with all C-N and N-N bond lengths between those of typical single and double bonds (Table 3.1). The C-N bond lengths for all three compounds fall between 1.3385(8) and 1.352(2) Å, while typical C-N single and double bonds are 1.47 and 1.29 Å, respectively.⁷ The N-N bond lengths fall between 1.3028(7) and 1.316(3) Å, while typical N-N single and double bonds are 1.45 and 1.25 Å. Complex **2.7** is relatively planar, with the boron atom displaced by 0.094 Å relative to the formazanate backbone, while the boron atoms of **2.8** and **3.5** are significantly further displaced by 0.713 Å and 0.755 Å, respectively, as a result of the large substituents bound to the boron centre. The 1,5-aryl substituents in complex **2.7** are slightly twisted with respect to the formazanate backbone, with the angle between the N1-N2-N3-N4 plane and the plane defined by the *N*-aryl substituents being 4.51 and 8.48°. Complexes **2.8** and **3.5** exist in a ‘dragonfly’ conformation where the dihedral angles between the 1,5-aryl substituents and formazanate backbone are significantly more twisted, with angles ranging from 54.9 to 67.9°. The ethynyl-substituted complexes exhibit B-N bond lengths slightly longer than those of complex **2.7**, with bond lengths ranging from 1.573(3) and 1.581(3) Å compared to 1.560(9) and 1.566(1) Å for **2.7**, indicating the boron atom of the parent BF₂ complex is strongly bound by the formazanate backbone. In contrast, the steric effects of the ethynyl-substituted boron complexes are a likely cause of the elongated B-N bonds, which suggest the boron atoms are more weakly held by the formazanate backbone in these ethynyl-substituted complexes.

Table 3.1. Selected bond lengths (Å) and angles (°) of compounds **2.7**, **2.8** and **3.5**.

| | 2.7 | 2.8 | 3.5 |
|---------------------------------|------------|--------------|--------------|
| B1-N1 | 1.566(1) | 1.575(4) | 1.576(3) |
| B1-N3 | 1.560(9) | 1.573(3) | 1.581(3) |
| N1-N2 | 1.3037(7) | 1.312(3) | 1.313(2) |
| N3-N4 | 1.3028(7) | 1.316(3) | 1.308(2) |
| C1-N2 | 1.3417(8) | 1.346(3) | 1.343(2) |
| C1-N4 | 1.3385(8) | 1.344(3) | 1.352(2) |
| Dihedral Angles ^a | 4.51, 8.48 | 54.92, 60.60 | 66.87, 67.92 |
| Boron Displacement ^b | 0.094 | 0.713 | 0.755 |

^aThe angle (°) between the *N*-aryl substituents and the N₄ plane of the formazanate backbone. ^bDistance (Å) between B₁ and the plane defined by the four N atoms.

3.2.3 Electrochemical Properties

The electrochemical properties of **3.5** were explored using cyclic voltammetry and are summarized in Table 3.2 along with complexes **2.7** and **2.8** for comparison. Experiments were performed in dry, degassed CH₂Cl₂ and the cyclic voltammograms are shown in Figure 3.3. Complexes **2.7**, **2.8** and **3.5** exhibited two ligand-centred reversible (or quasi-reversible) one-electron reduction waves at $E^{\circ}_{\text{red1}} = -1.04, -1.18, -1.21$ V and $E^{\circ}_{\text{red2}} = -1.99, -2.03$ and -2.13 V, respectively, relative to the ferrocene/ferrocenium redox couples. All three complexes also exhibited one quasi-reversible oxidation wave at $E^{\circ}_{\text{ox1}} = 1.03, 0.83$ and 0.89 , respectively. In addition, complex **3.5** exhibited another reversible oxidation at a lower potential ($E^{\circ}_{\text{Fc}} = 0.03$ V). This additional oxidation was a two electron process and corresponded to the coincident oxidation of the two ferrocene moieties.

Table 3.2. Summary of the electrochemical properties of compounds **2.7**, **2.8** and **3.5**.^a

| Compound | E°_{red1} (V) | E°_{red2} (V) ^b | E°_{Fc} (V) | E°_{ox1} (V) |
|------------|-------------------------------|--|-----------------------------|------------------------------|
| 2.7 | -1.04 | -1.99 | - | 1.03 |
| 2.8 | -1.18 | -2.03 | - | 0.83 |
| 3.5 | -1.21 | -2.13 | 0.03 | 0.89 |

^aCyclic voltammograms were recorded in dry, degassed CH_2Cl_2 containing ~ 1 mM analyte and 0.1M $[\text{nBu}_4\text{N}][\text{PF}_6]$ as a supporting electrolyte at a scan rate of 250 mV s^{-1} . Compounds **2.7**, **2.8** and **3.5** was referenced internally against the ferrocene/ferrocenium redox couple. ^bReduction peaks are not reversible and the values listed are of the maximum cathodic current.

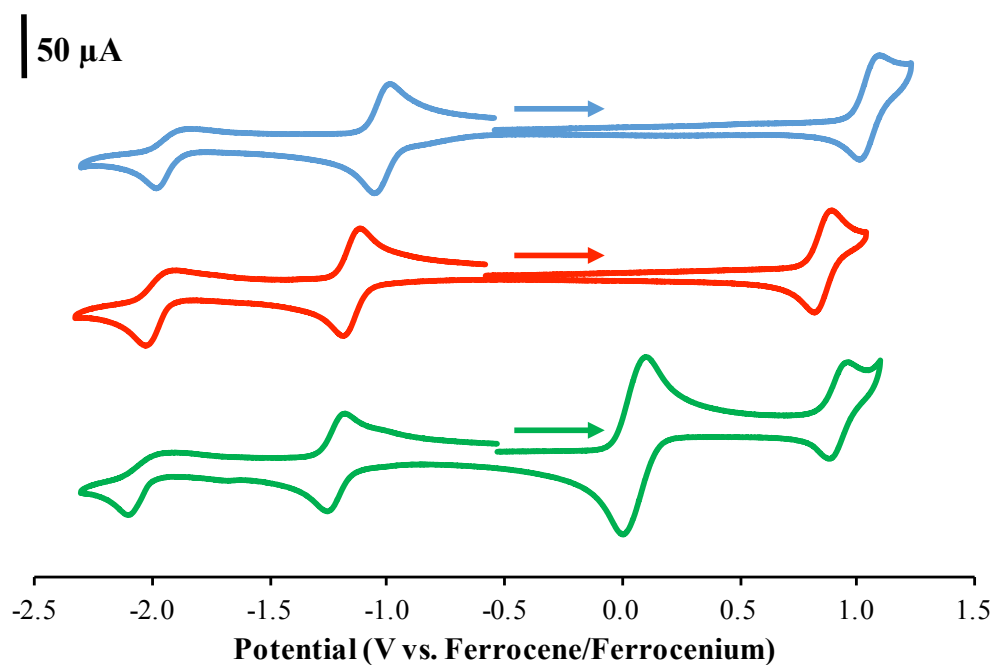


Figure 3.3. Cyclic voltammograms of compounds **2.7** (blue), **2.8** (red) and **3.5** (green) recorded in dry, degassed CH_2Cl_2 containing ~ 1 mM analyte and 0.1 M $[\text{nBu}_4\text{N}][\text{PF}_6]$ as a supporting electrolyte at a scan rate of 250 mV s^{-1} . Arrows indicate the direction of scan.

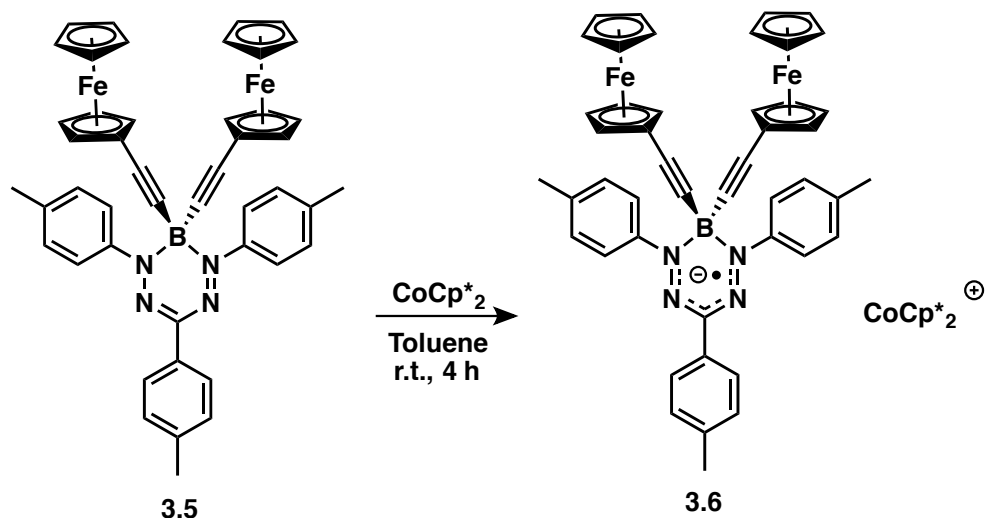
Relative to the parent BF_2 complex (**2.7**), **3.5** was found to be more difficult to reduce and easier to oxidize as it lacks electronegative fluorine groups, following the trend observed in complex **2.8** and others from Chapter 2. The first oxidation wave of compound **3.5** (Figure 3.3, green) is a two \times one-electron process and may be attributed

to oxidation of the ferrocene moieties. The coincidence or near coincidence of the waves indicates that there is little or no communication between the two ferrocene substituents through the boron atom, as both ferrocene moieties oxidize at the same (or nearly the same) potential. The second oxidation wave was found to become more reversible upon an increase of the scan rate. Based on the information obtained from the cyclic voltammograms, appropriate oxidants and reductants were selected in order to probe the chemically reduced and oxidized forms of the ferrocene complex **3.5**.

3.2.4 Reduced & Oxidized Forms of Redox-Active Complex

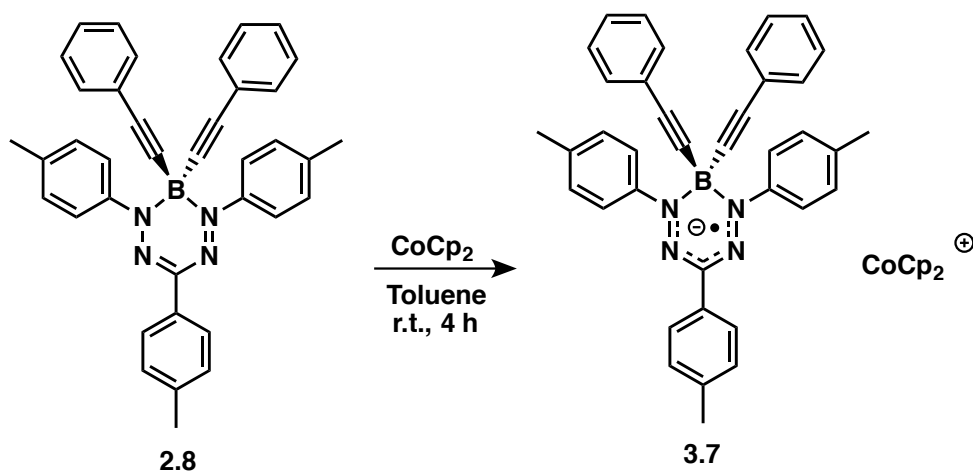
3.5

The reduced form of the redox-active boron formazanate complex was isolated by first dissolving 1 equiv. of bis(pentamethylcyclopentadienyl)cobalt(II) (CoCp^*_2) in toluene and stirring for 15 min in a glovebox (Scheme 3.2). The CoCp^*_2 solution was then added dropwise to a stirring solution of complex **3.5** in dry toluene and the resulting solution turned from deep purple to an emerald green suspension. The suspension was stirred for 4 h, vacuum filtered and the resulting green solid was washed with 5 mL toluene followed by 10 mL pentane before it was dried *in vacuo* to afford the final reduced complex **3.6** in 89% yield.



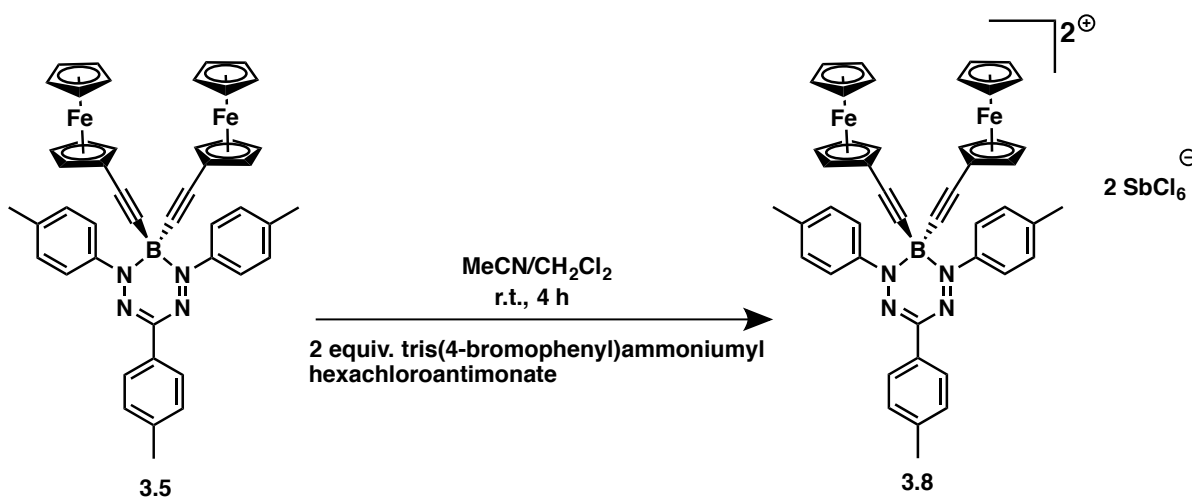
Scheme 3.2. Synthesis of the reduced ferrocene-containing boron formazanate complex **3.6**.

In order to achieve an accurate basis for comparison, reduction of the phenylacetylene complex from Chapter 2 (**2.8**) was carried out using cobaltocene (CoCp_2) (Scheme 3.3) under the same conditions described above for reduction of the ferrocene complex (Scheme 3.2). While the reduced phenylacetylene complex **3.7** was a green powder with the CoCp_2^+ counter ion, CoCp^*_2 was used for the reduced ferrocene complex **3.6** to increase crystallinity of the sample in an effort to explore its X-ray crystallographic properties.



Scheme 3.3. Synthesis of the reduced phenylacetylene complex **3.7**.

The oxidized form of the ferrocene complex **3.5** was isolated by first dissolving complex **3.5** in a 1:1 mixture of dry MeCN and dry CH₂Cl₂ in a glovebox and stirring at room temperature for 15 min (Scheme 3.4). Separately, 2 equiv. of tris(4-bromophenyl)ammoniumyl hexachloroantimonate (magic blue) was dissolved in MeCN and stirred for 15 min. The magic blue solution was then added dropwise to the solution containing **3.5** and the resulting solution turned from deep purple to dark green. The solution was then stirred for 4 h to afford the final oxidized complex **3.8** in 90% yield.



Scheme 3.4. Synthesis of the oxidized ferrocene-containing boron formazanate complex **3.8**.

3.2.5 UV-Visible Absorption Spectroscopy

The UV-Visible absorption spectra of compounds **3.5**, **3.6** and **3.8** are shown in Figure 3.4 and summarized in Table 3.3. All three compounds absorb in the visible region of the electromagnetic spectrum, with significant changes to the absorbance spectrum upon reduction or oxidation of complex **3.5**.

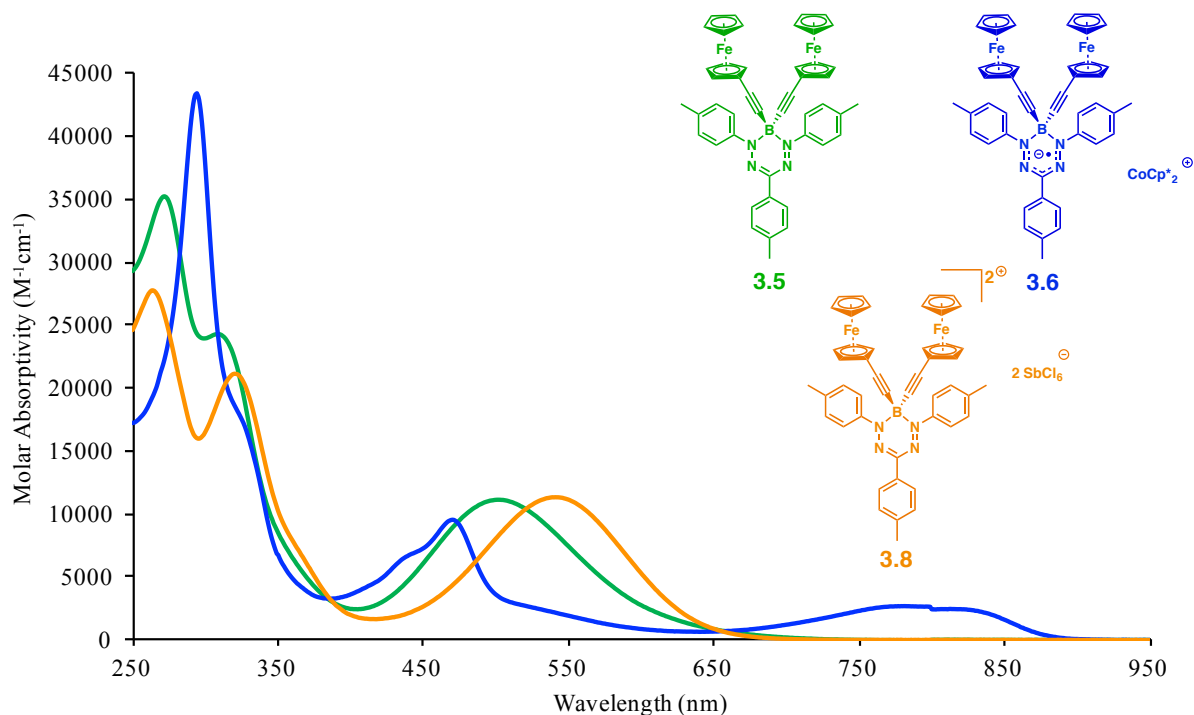


Figure 3.4. UV-Visible absorption spectra of compounds **3.5**, **3.6** and **3.8** recorded for degassed 10 μM CH_3CN solutions.

Upon reduction with CoCp^*_2 , complex **3.6** exhibits a longer-wavelength absorption (~ 775 nm) as well as peaks at 470 and 294 nm, providing evidence for a singly reduced formazanate backbone, which agrees with previous reports.^{8,9} The position of these peaks is also similar to those reported for triarylverdazyls.¹⁰ Furthermore, the formation of a singly reduced formazanate backbone is supported by the UV trace of the reduced phenylacetylene complex **3.7** compared to its neutral parent complex **2.8** shown in Figure 3.5 and summarized in Table 3.4.

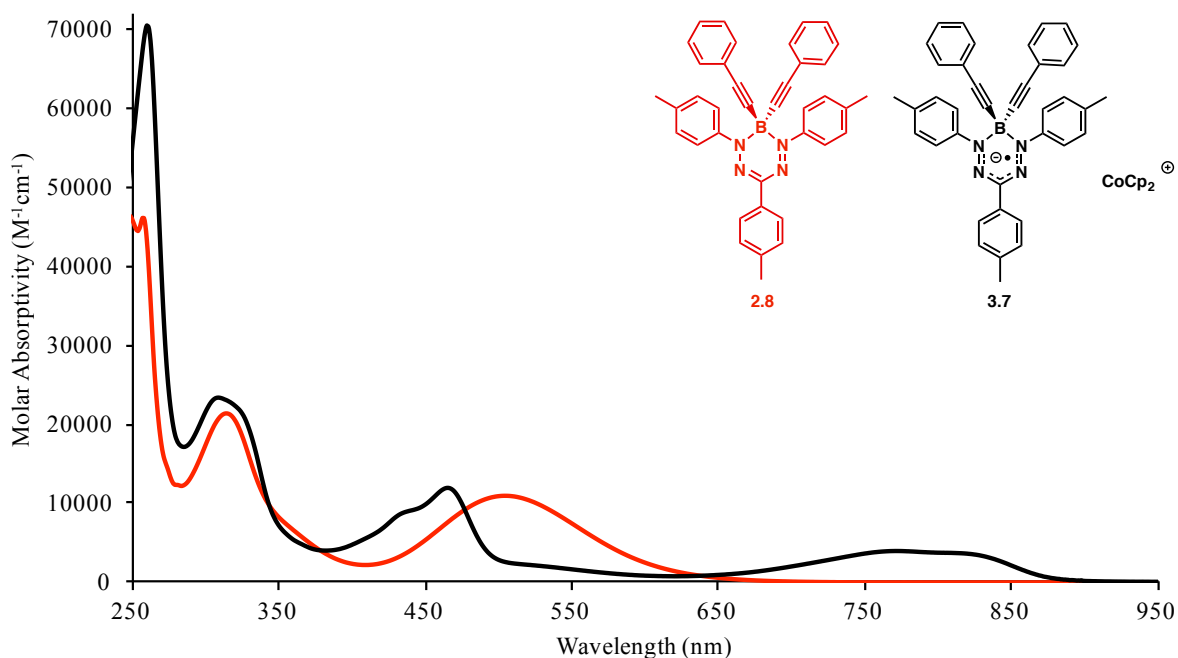


Figure 3.5. UV-Visible absorption spectra of compounds **2.8** and **3.7** recorded for degassed 10 μM CH_3CN solutions.

The reduction of complex **2.8** exhibits a similar UV trace to the reduction of complex **3.7**, as a longer-wavelength absorption is observed as well as blue-shifted absorption maxima at 465 and 308 nm.

Table 3.3. Spectroscopic properties of complexes **3.5**, **3.6** and **3.8**.

| Compound | Solvent | λ_{max}^a , nm, (ϵ , $\text{M}^{-1} \text{cm}^{-1}$) |
|------------|------------------------|--|
| 3.5 | CH_3CN | 271 (35 200), 309 (24 300), 501 (11 150) |
| 3.6 | CH_3CN | 294 (43 450), 470 (9600), 775 (2700), 830 (2350) |
| 3.8 | CH_3CN | 264 (27 700), 320 (21 100), 541 (11 300) |

^aValues recorded for degassed 10 μM solutions.

Table 3.4. Spectroscopic properties of complexes **2.8** and **3.7**.

| Compound | Solvent | λ_{\max}^a , nm, (ϵ , $M^{-1} \text{ cm}^{-1}$) |
|------------|--------------------|--|
| 2.8 | CH ₃ CN | 257 (45 800), 312 (21 000), 504 (10 800) |
| 3.7 | CH ₃ CN | 260 (70 400), 308 (23 300), 465 (11 900), 787 (3800), 826 (3450) |

^aValues recorded for degassed 10 μM solutions.

Further supporting the presence of radical complexes **3.6** and **3.7** is a broad, featureless signal present in each of the electron paramagnetic resonance (EPR) spectra at $g = 2.0035$ (Figure 3.6a, b), similar to other ligand-centred boron formazanate radicals.^{9,10}

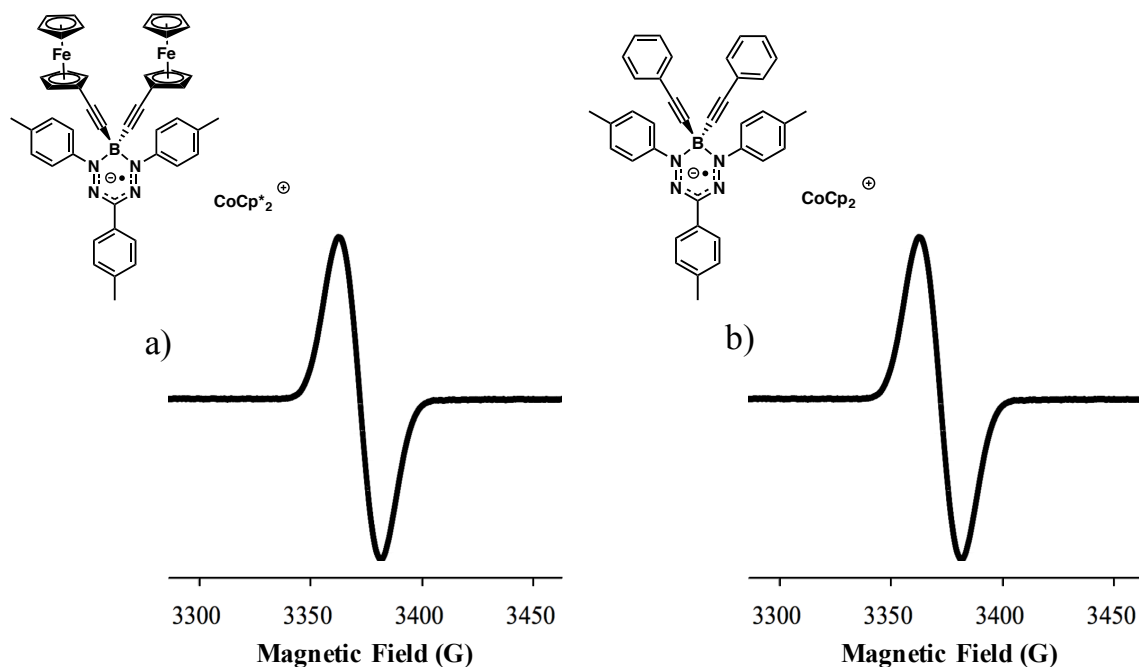


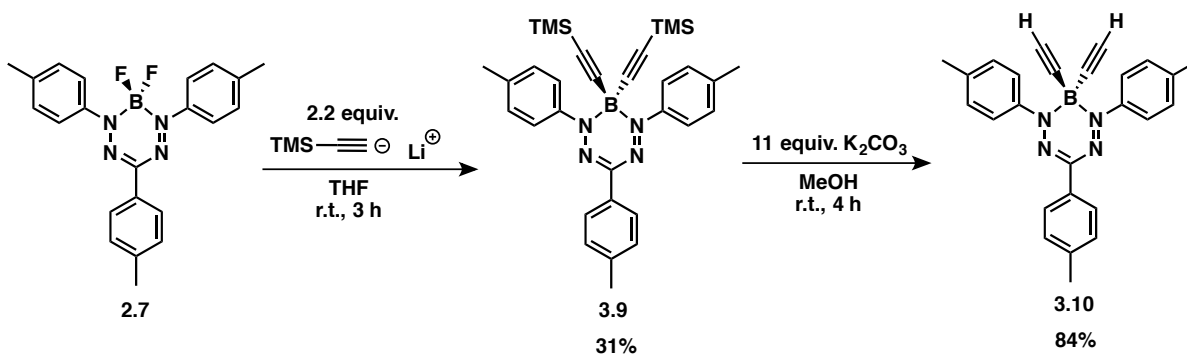
Figure 3.6. EPR spectra of a) **3.6** and b) **3.7** in degassed THF at 298 K ($g = 2.0035$).

Upon oxidation of complex **3.5** with magic blue, the absorption spectrum of **3.8** exhibits a red-shift of 40 nm in the $\pi \rightarrow \pi^*$ region from 501 to 541 nm (Figure 3.4). Furthermore, complex **3.8** did not produce a signal in the EPR spectrum at 298 K, as the ferrocenium cation is not detected above 77 K as a result of fast spin-lattice relaxation.¹¹

3.2.6 Post-synthetic Functionalization via Cu(I)-Catalyzed Click Chemistry

Click Chemistry

CuAAC chemistry was explored using the terminal acetylene at the boron centre as the functional handle in order to further expand the scope of boron formazanate chemistry. Boron-acetylene complex **3.10** was synthesized by first dissolving 2.2 equiv. of trimethylsilylacetylene in dry THF, cooling to $-78\text{ }^{\circ}\text{C}$ and stirring for 30 min (Scheme 3.5). 2.2 equiv. of *n*-BuLi was then added dropwise and the solution was stirred at $-78\text{ }^{\circ}\text{C}$ for 1 h. The solution was held at $-78\text{ }^{\circ}\text{C}$ and added dropwise to a solution of **2.7** dissolved in dry THF at $-78\text{ }^{\circ}\text{C}$. The deep purple solution slowly turned red/orange as the solution was brought from $-78\text{ }^{\circ}\text{C}$ to room temperature and stirred for 3 h. Complex **3.9** was then added to a solution of 11 equiv. of K_2CO_3 in MeOH and stirred for 4 h at room temperature to afford the final boron-acetylene complex **3.10** in 84% yield.



Scheme 3.5. Synthesis of boron acetylene complex **3.10**.

The formation of complex **3.9** was accompanied by the appearance of a large singlet at 0.05 ppm in the ^1H NMR spectrum corresponding to the TMS groups (Figure 3.8, top). A disappearance of the 1:1:1:1 quartet in the ^{19}F NMR spectrum and a disappearance of the 1:2:1 triplet and appearance of a broad singlet in the ^{11}B NMR spectrum were also observed (Figures B4–B5), indicating the fluorine atoms were no longer present. The formation of complex **3.10** was accompanied by the disappearance of the TMS signal at 0.05 ppm in the ^1H NMR spectrum and the appearance of the terminal

acetylene protons at 2.23 ppm (Figure 3.8, middle, Figures B6–B7). Further supporting the formation of this compound was two diagnostic signals in the IR spectrum indicating the presence of a terminal acetylene at 3281 and 2060 cm^{-1} (Figure 3.7).

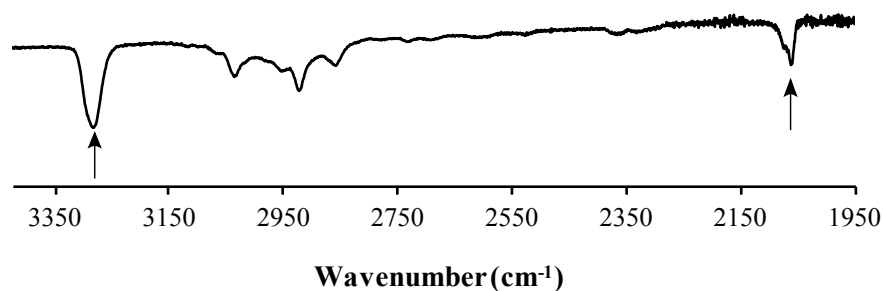
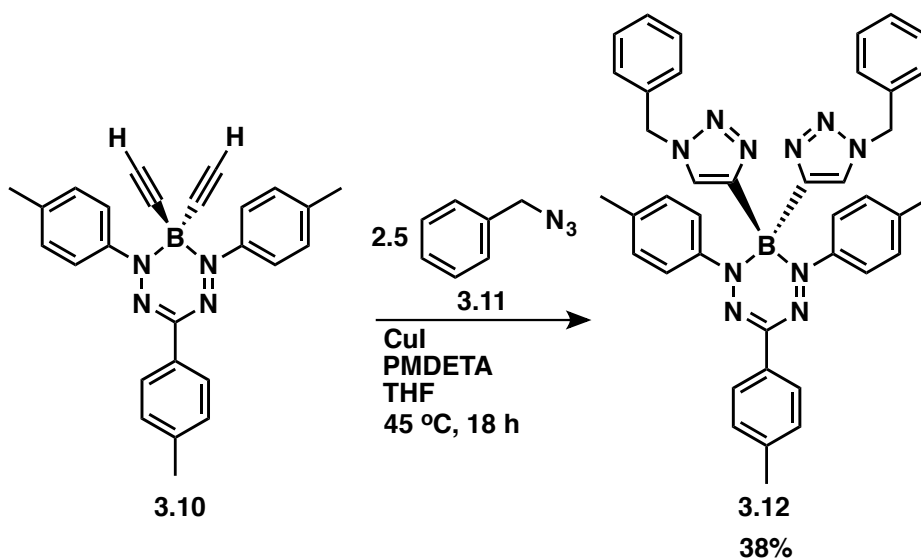


Figure 3.7. IR spectrum of compound **3.10**. Arrows indicate the terminal acetylene functionality at 3281 and 2060 cm^{-1} .

As a proof of concept, benzyl azide (**3.11**) was used as a model reactant for the CuAAC reaction with complex **3.10** to afford the cycloaddition product **3.12** (Scheme 3.6).



Scheme 3.6. CuAAC reaction with benzyl azide.

The formation of complex **3.12** was accompanied by a disappearance of the terminal acetylene protons at 2.23 ppm in the ¹H NMR spectrum and the appearance of the

diagnostic benzyl protons at 5.36 ppm, as well as a signal corresponding to the protons of the triazole rings at 8.07 ppm (Figure 3.8 bottom, Figures B8–B9). Further supporting the formation of the cycloaddition product was the disappearance of the acetylene stretches at 3281 and 2060 cm^{-1} from the IR spectrum of **3.10** (Figure 3.9, black) to **3.12** (Figure 3.9, blue). The IR spectrum also confirmed the consumption of benzyl azide (Figure 3.9, red), as no azide stretch was present at 2095 cm^{-1} in the spectrum of **3.12** (Figure 3.9, black).

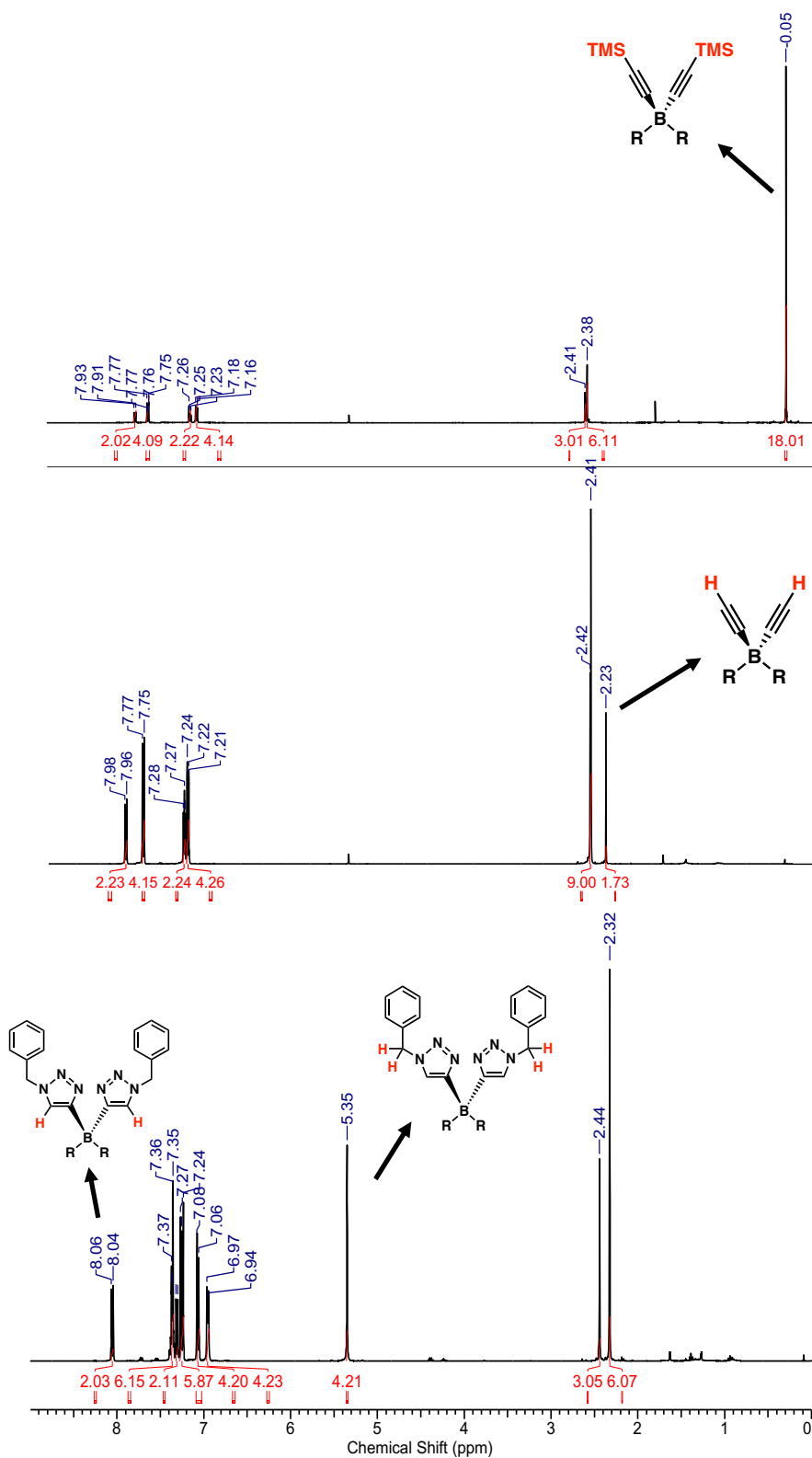


Figure 3.8. ^1H NMR spectra of compounds **3.9** (top), **3.10** (middle) and **3.12** (bottom) in CDCl_3 . Red highlights on structures indicate protons of interest.

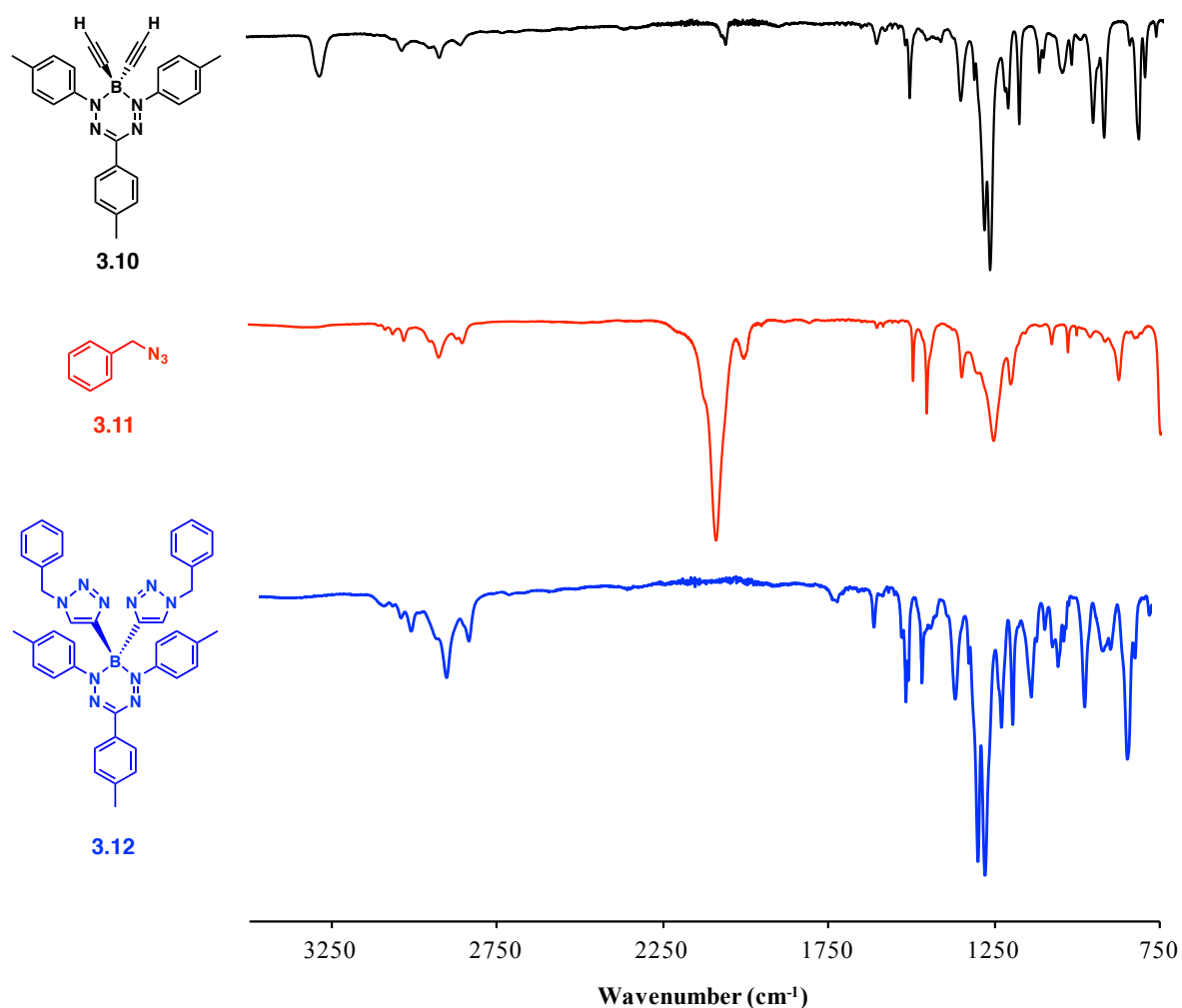


Figure 3.9. IR spectra of compounds **3.10** (black), **3.11** (red) and **3.12** (blue).

3.2.7 UV-Visible Absorption Spectroscopy

The UV-Visible absorption spectra of compounds **3.10** and **3.12** are shown in Figure 3.10 and relevant data are summarized in Table 3.5. Both compounds absorb in the visible region of the electromagnetic spectrum with the cycloaddition product exhibiting a slight red-shift in the $\pi \rightarrow \pi^*$ region from 524 to 532 nm. The slight red-shift observed is in agreement with previous reports of similar BF₂ formazanate systems in which red-shifts of up to 30 nm were observed in cycloaddition products.¹²

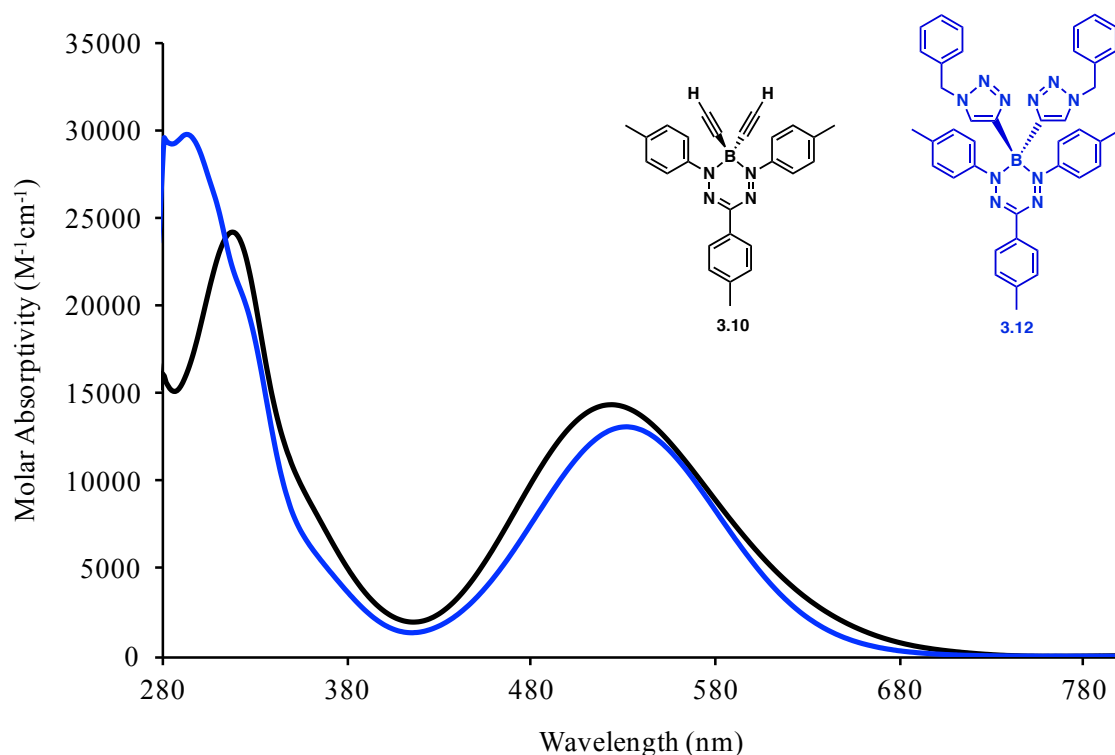


Figure 3.10. UV-Visible absorption spectra of compounds **3.10** and **3.12** recorded for degassed 10 μM toluene solutions.

Table 3.5. Spectroscopic properties of complexes **3.10** and **3.12**.

| Compound | Solvent | λ_{max}^a , nm, (ϵ , $M^{-1} cm^{-1}$) |
|-------------|---------|---|
| 3.10 | Toluene | 317 (28 500), 524 (16 900) |
| 3.12 | Toluene | 295 (36 000), 532 (14 000) |

^aValues recorded for degassed 10 μM solutions.

3.3 Conclusions

Through the ethynyl moiety it has been demonstrated that functionality can be introduced at the boron centre including redox-active handles and functional groups capable of undergoing post-synthetic modification. The first reported alkynyl-substituted boron formazanate complex bearing a redox-active ferrocene moiety was synthesized, and its optical and spectroscopic properties were explored alongside the chemically oxidized and reduced forms of the parent system (**3.5**, **3.6** and **3.8**) and the

reduced phenylacetylene complex **3.7**. X-ray crystallography revealed an elongation of the B-N bonds upon incorporation of the ethynylferrocene moiety (**3.5**) at the boron atom, and all C-N and N-N bond lengths were found to be between those of typical single and double bonds, indicating a significant degree of electronic delocalization. The boron atoms were found to be significantly displaced from the plane of the formazanate backbone, as the displacement in the parent BF₂ (**2.7**) was found to be 0.094 Å while the displacement in the ethynylferrocene complex (**3.5**) and phenylacetylene complex (**2.8**) was found to be 0.755 and 0.713 Å, respectively. Significant twisting of the *N*-aryl substituents on the formazanate backbone was also observed as a result of the increased steric bulk at the boron centre, with complexes **2.8** and **3.5** existing in a ‘dragonfly’ conformation where the dihedral angles between the 1,5-aryl substituents and the formazanate backbone were found to be 54.9 and 67.9°. IR spectroscopy confirmed the presence of an internal alkyne at 2188 cm⁻¹ for complex **3.5**. The three ferrocene complexes (**3.5**, **3.6** and **3.8**) were found to absorb within the visible region of the electromagnetic spectrum, with drastic changes to the absorbance spectrum upon chemical reduction or oxidation of the parent complex **3.5**. A similar trend was observed upon the chemical reduction of the neutral phenylacetylene complex **2.8**, showing a UV trace similar to that of the reduced ferrocene complex. Upon reduction of **3.5** with CoCp^{*}₂, a longer-wavelength absorption at 775 nm was observed alongside a blue-shift of the λ_{max} from 501 nm in the parent complex to 470 nm, closely matching the UV trace of the similarly reduced phenylacetylene complex **3.7**, providing evidence for a singly reduced formazanate backbone. EPR spectroscopy also confirmed the presence of a radical with *g* = 2.0035, similar to other ligand-centred formazanate radicals. Oxidation of the parent ferrocene complex with magic blue unexpectedly caused a red-shift of the λ_{max} from 501 nm in the parent complex to 541 nm. Cyclic voltammetry demonstrated that complex **3.5** was redox-active and exhibited two quasi-reversible one-electron reduction processes and two oxidation processes (one quasi-reversible, the other reversible) relative to the ferrocene/ferrocenium redox couple. Electrochemical data suggested complex **3.5** was

more difficult to reduce and easier to oxidize compared to the parent BF_2 complex (**2.7**). The first oxidation wave of **3.5** was determined to be a two \times one-electron process attributed to oxidation of the ferrocene moieties. The coincidence or near coincidence of the waves indicated little or no communication between the two ferrocene substituents through the boron atom.. The CuAAC reaction was also explored as a means to further modify the boron formazanate template. As a proof of concept, benzyl azide was used as a model reactant for the CuAAC reaction with boron acetylene complex **3.10**. The cycloaddition product was successfully synthesized and characterized by the disappearance of terminal acetylene protons at 2.23 ppm in the ^1H NMR of the starting material and appearance of diagnostic benzyl protons at 5.36 ppm and protons characteristic of the triazole rings at 8.07 ppm in the cycloaddition product (**3.12**). IR spectra revealed a disappearance of the terminal acetylene stretches at 3281 and 2060 cm^{-1} , and comparison with the IR spectrum of benzyl azide confirmed no residual azide remained, confirming the successful synthesis of the cycloaddition product.

3.4 Experimental

3.4.1 General Considerations

Solvents were obtained from Caledon Laboratories, dried using an Innovative Technologies Inc. solvent purification system, collected under vacuum, and stored under an N_2 atmosphere over 4 Å molecular sieves. All other reagents were purchased from Sigma Aldrich, Alfa Aesar or Oakwood Chemical and used as received. NMR spectra were recorded on a Bruker 400 MHz NMR spectrometer, 400 MHz Varian INova NMR spectrometer, or 600 MHz Varian Inova NMR spectrometer. ^1H NMR spectra were recorded in CDCl_3 and referenced against residual protonated solvent at 7.27 ppm. $^{13}\text{C}\{^1\text{H}\}$ NMR spectra were referenced to CDCl_3 at 77.0 ppm. ^{11}B NMR spectra were referenced internally to $\text{BF}_3\cdot\text{OEt}_2$ at 0 ppm. ^{19}F NMR spectra were referenced internally to CFCl_3 at 0 ppm. Mass spectra were recorded in positive-ion mode using a high-resolution Finnigan MAT 8200 spectrometer. UV-Vis absorption

spectra were recorded using a Cary 5000 Scan instrument using standard quartz cells (1 cm path length) with a scan range of 200 to 800 nm. Samples were dissolved in spectroscopic grade solvents to obtain various concentrations. The background was subtracted from each spectrum and the solvent used for each experiment is indicated. FT-IR spectra were recorded using a Perkin Elmer Spectrum Two FT-IR spectrometer.

3.4.2 X-ray Crystallography Methods

Single crystals suitable for X-ray diffraction studies were grown by slow vapour diffusion of pentane into a saturated CH_2Cl_2 solution (**3.5**) and were analyzed by Ryan Maar. Samples were mounted on a MiTeGen polyimide micromount with a small amount of Paratone *N* oil. X-ray measurements were made on a Bruker Kappa Axis Apex2 diffractometer or Nonius KappaCCD Apex2 diffractometer at a temperature of 110 K. The unit cell dimensions of complex **3.5** were determined from a symmetry constrained fit of 9882 reflections with $7.64^\circ < 2\theta < 131.94^\circ$. The data collection strategy was a number of ω and φ scans which collected data up to 132.764° (2θ). The frame integration was performed using SAINT.¹³ The resulting raw data was scaled and absorption corrected using a multi-scan averaging of symmetry equivalent data using SADABS.¹⁴ The structure was solved by using a dual space methodology using the SHELXT program.¹⁵ All non-hydrogen atoms were obtained from the initial solution. The hydrogen atoms for complex **3.5** were introduced at idealized positions and were allowed to ride on the parent atom. The structural model was fit to both sets of data using full matrix least-squares based on F^2 . The calculated structure factors included corrections for anomalous dispersion from the usual tabulation. The structures were refined using the SHELXL program from the SHELX suite of crystallographic software.¹⁶ Graphic plots were produced using the Mercury program suite.¹⁷ See Appendix B for additional crystallographic data.

Table 3.6. X-ray diffraction data collection and refinement details for compound **3.5**.

| | 3.5 |
|---------------------------------------|---|
| Formula | C ₄₆ H ₃₉ BF _{e2} N ₄ |
| Formula Weight (g mol ⁻¹) | 770.32 |
| Crystal Dimensions (mm) | 0.612 × 0.227 × 0.224 |
| Crystal Colour and Habit | red prism |
| Crystal System | monoclinic |
| Space Group | P 2 ₁ /c |
| Temperature, (K) | 110 |
| <i>a</i> , (Å) | 13.8977(15) |
| <i>b</i> , (Å) | 14.8248(19) |
| <i>c</i> , (Å) | 18.489(2) |
| α, (°) | 90 |
| β, (°) | 92.527(5) |
| γ, (°) | 90 |
| <i>V</i> , (Å ³) | 3805.6(8) |
| <i>Z</i> | 4 |
| ρ (g cm ⁻¹) | 1.344 |
| λ, Å, (CuKα) | 1.54178 |
| μ, (cm ⁻¹) | 6.401 |
| Diffractometer Type | Nonius Kappa CCD Apex2 |
| R ₁ | 0.0312 |
| ωR ₂ | 0.0786 |
| R ₁ (all data) | 0.0351 |
| ωR ₂ (all data) | 0.0804 |
| GOF | 1.029 |

$$R_1 = \frac{\sum(|F_o| - |F_c|)}{\sum F_o}$$

$$\omega R_2 = \left[\frac{\sum(\omega(F_o^2 - F_c^2)^2)}{\sum(\omega F_o^4)} \right]^{1/2}$$

$$GOF = \left[\frac{\sum(\omega(F_o^2 - F_c^2)^2)}{(\text{No. of reflns.} - \text{No. of params.})} \right]^{1/2}$$

3.4.3 Electrochemical Methods

Cyclic voltammetry experiments were performed using a Bioanalytical Systems Inc. (BASi) Epsilon potentiostat and analyzed using BASi Epsilon software. Typical electrochemical cells consisted of a three-electrode setup including a glassy carbon working electrode, platinum counter electrode, and silver *pseudo* reference electrode. Experiments were run at 250 mV s⁻¹ in degassed CH₂Cl₂ solutions of the analyte

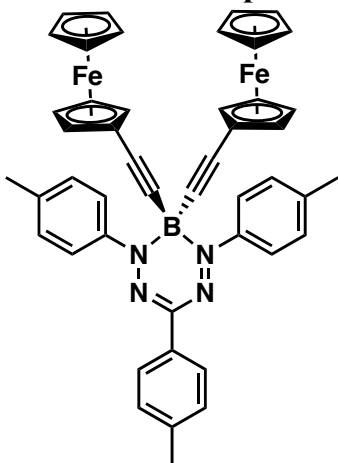
(~1 mM) and electrolyte (0.1 M [*n*Bu₄N][PF₆]). Cyclic voltammograms were internally referenced against the ferrocene/ferrocenium redox couple (~1 mM internal standard) and corrected for internal cell resistance using the BASi Epsilon software. Ferrocene complex **3.5** was internally referenced against the ferrocene/ferrocenium redox couple using decamethylferrocene/decamethylferrocenium (−520 mV vs ferrocene/ferrocenium).

3.4.4 Electron Paramagnetic Resonance Spectroscopy

EPR measurements were made for degassed 10 μM THF solutions of radical anions **3.6^{•−}** and **3.7^{•−}** using a JEOL JES-FA200 EPR spectrometer. All measurements were made at 25 °C and *g*-values were referenced relative to a built-in Mn²⁺ marker within the resonant cavity of the instrument.

3.4.5 Synthetic Procedures

Ferrocene Complex **3.5**

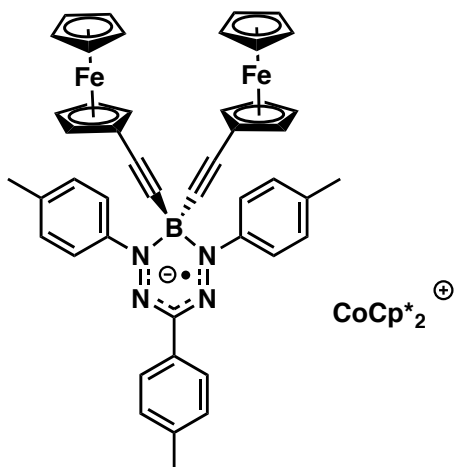


Under N₂, ethynyl ferrocene (0.36 g, 1.7 mmol) was dissolved in dry THF (5 mL) in a greaseless Schlenk flask, cooled to −78 °C and stirred for 30 min. *n*-BuLi (0.68 mL, 1.7 mmol) was added dropwise over 5 min and the solution was stirred for 1 h. The solution was then brought to room temperature and stirred for 30 min before it was added dropwise to a second greaseless Schlenk flask containing BF₂ complex **2.7** (0.31 g, 0.79 mmol) dissolved in THF (10 mL).

The solution was then stirred at room temperature for 2 h and quenched with deionized H₂O (7 mL), the organics were extracted with Et₂O and washed with deionized H₂O (3 × 50 mL), dried over MgSO₄, gravity filtered and concentrated *in vacuo*. The resulting residue was purified by flash chromatography (silica gel). The column was first flushed with hexanes (150 mL) to remove impurities, followed by toluene (50 mL) to afford the resulting complex **3.5** as a green/blue microcrystalline solid.

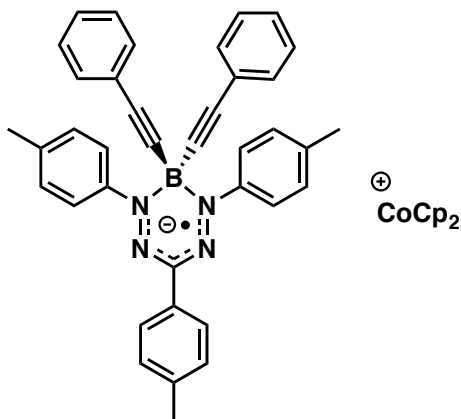
Yield = 0.12 g (19%). ^1H NMR (399.8 MHz, CDCl_3) δ 8.04 (dm, 2H, $J_{\text{HH}} = 4$ Hz, Aryl CH), 7.90 (dm, 4H, $J_{\text{HH}} = 12$ Hz, Aryl CH), 7.30–7.26 (m, 6H, Aryl CH), 4.22 (t, 4H, $J_{\text{HH}} = 4$ Hz, Aryl CH), 4.05 (t, 4H, $J_{\text{HH}} = 4$ Hz, Aryl CH), 3.92 (s, 10H, Aryl CH), 2.42 (s, 9H, CH_3). ^{11}B NMR (128.3 MHz, CDCl_3) δ -11.8 (s). $^{13}\text{C}\{^1\text{H}\}$ NMR (101.6 MHz, CDCl_3) δ 151.8, 143.4, 139.2, 138.7, 131.4, 129.3, 128.4, 125.6, 125.1, 98.2, 77.2, 71.2, 69.6, 68.0, 66.6, 21.39, 21.36. FT-IR (ATR, cm^{-1}) 3093, 3037, 2957, 2923, 2854, 2358, 2189, 1739, 1605, 1506, 1456, 1353, 1282, 1263. UV-Vis (CH_3CN): $\lambda_{\text{max}} = 271$ nm ($\epsilon = 35\,200$ $\text{M}^{-1}\text{cm}^{-1}$), 309 nm ($\epsilon = 24\,300$ $\text{M}^{-1}\text{cm}^{-1}$), 501 nm ($\epsilon = 11\,150$ $\text{M}^{-1}\text{cm}^{-1}$). ESI-HRMS (+ve mode) calculated for $[\text{C}_{46}\text{H}_{39}\text{BFe}_2\text{N}_4]^+$: 770.1967, found 770.1977, difference: +1.2 ppm.

Reduced Ferrocene Complex 3.6



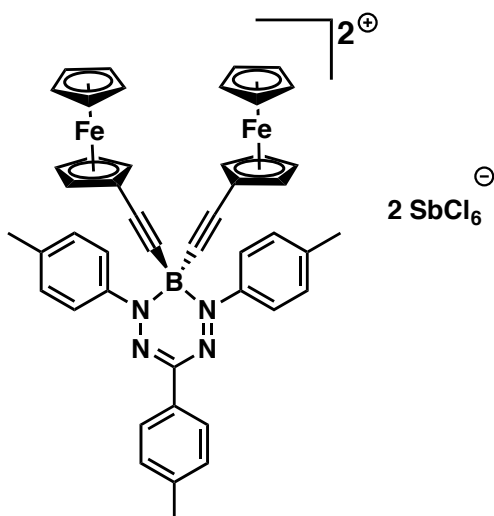
In an N_2 filled glovebox, complex **3.5** (0.18 g, 0.23 mmol) was dissolved in toluene (15 mL) and stirred for 15 min. Separately, bis(pentamethylcyclopentadienyl) cobalt(II) (0.075 g, 0.23 mmol) was dissolved in toluene (6 mL) and stirred for 15 min. This solution was then added dropwise to the solution of complex **3.5** and stirred for 4 h. The resulting emerald green suspension was then vacuum filtered, and the solid was washed with toluene (5 mL) followed by pentane (10 mL) before the microcrystalline green powder was dried *in vacuo*. Yield = 0.27 g (89%). FT-IR (ATR, cm^{-1}) 3096, 3078, 3021, 2991, 2958, 2916, 2853, 2156, 1716, 1602, 1501, 1374, 1334. UV-Vis (CH_3CN): $\lambda_{\text{max}} = 294$ ($\epsilon = 43\,450$ $\text{M}^{-1}\text{cm}^{-1}$), 470 ($\epsilon = 9600$ $\text{M}^{-1}\text{cm}^{-1}$), 767 ($\epsilon = 2700$ $\text{M}^{-1}\text{cm}^{-1}$), 833 ($\epsilon = 2350$ $\text{M}^{-1}\text{cm}^{-1}$) nm. ESI-HRMS (-ve mode) calculated for $[\text{C}_{46}\text{H}_{39}\text{BFe}_2\text{N}_4]^-$: 770.1972, found 770.1967, difference: +0.7 ppm.

Reduced Phenylacetylene Complex 3.7



In a N₂ filled glovebox, complex **2.8** (0.29 g, 0.51 mmol) was dissolved in toluene (15 mL) and stirred for 15 min. Separately, bis(cyclopentadienyl)cobalt (II) (0.10 g, 0.51 mmol) was dissolved in toluene (6 mL) and stirred for 15 min. The solution was then added dropwise to the solution of complex **2.8** and stirred for 4 h. The resulting brown/green suspension was then vacuum filtered, and the solid was washed with toluene (5 mL) followed by pentane (10 mL) to afford complex **3.7** as a green powder. Yield = 0.31 g (81%). FT-IR (ATR, cm⁻¹) 3098, 3015, 2919, 2858, 1500, 1485, 1415, 1327, 1278, 1260. UV-Vis (CH₃CN): λ_{max} = 260 (ε = 70 400 M⁻¹ cm⁻¹), 308 (ε = 23 300 M⁻¹ cm⁻¹), 465 (ε = 11 900 M⁻¹ cm⁻¹), 787 (ε = 3800 M⁻¹ cm⁻¹), 826 nm (ε = 3450 M⁻¹ cm⁻¹). ESI-HRMS (-ve mode) calculated for [C₃₈H₃₁BN₄]⁻: 554.2647, found 554.2642, difference: +0.9 ppm.

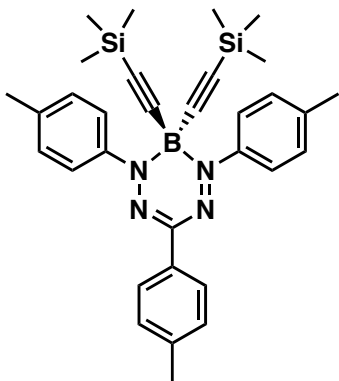
Oxidized Ferrocene Complex 3.8



In an N₂ filled glovebox, complex **3.5** (0.10 g, 0.13 mmol) was dissolved in MeCN (7 mL) and CH₂Cl₂ (7 mL) and stirred for 15 min. Separately, tris(4-bromophenyl) ammonium hexachloroantimonate (0.22 g, 0.27 mmol) was dissolved in acetonitrile (6 mL) and stirred for 15 min. The solution was then added dropwise to the solution of complex **3.5** and stirred for 4 h. The purple suspension was then concentrated *in vacuo* and the resulting residue was purified by flash chromatography (CH₂Cl₂, alumina) to remove impurities followed by THF to afford complex **3.8** as a purple film. Yield = 0.17 g (90%). FT-IR (ATR, cm⁻¹) 3033, 2973, 2924, 2857, 1894,

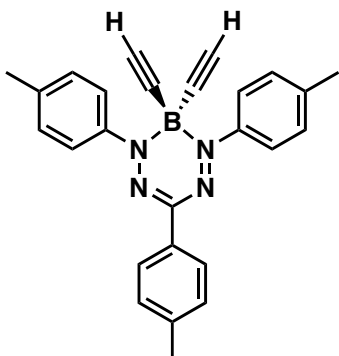
1579, 1484, 1310, 1282, 1264. UV-Vis (CH₃CN): $\lambda_{\max} = 264$ ($\epsilon = 27\,700\text{ M}^{-1}\text{ cm}^{-1}$), 321 ($\epsilon = 21\,100\text{ M}^{-1}\text{ cm}^{-1}$), 541 nm ($\epsilon = 11\,300\text{ M}^{-1}\text{ cm}^{-1}$).

TMS-acetylene Complex 3.9



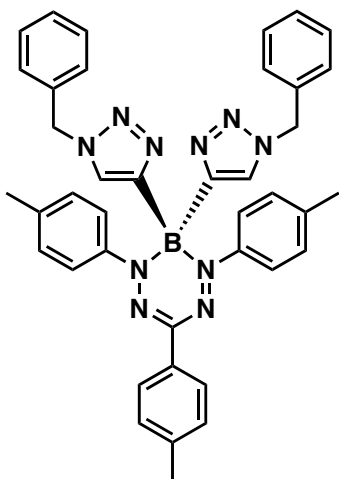
Under N₂, trimethylsilylacetylene (0.27 mL, 1.9 mmol) was dissolved in dry THF (5 mL) in a greaseless Schlenk flask, cooled to $-78\text{ }^{\circ}\text{C}$ and stirred for 30 min. *n*-BuLi (0.79 mL, 1.9 mmol) was added very slowly over 5 min and the solution was stirred for 1 h. The solution was held at $-78\text{ }^{\circ}\text{C}$ and then added dropwise to a second greaseless Schlenk flask containing BF₂ complex **2.7** (0.35 g, 0.90 mmol) dissolved in THF (10 mL) at $-78\text{ }^{\circ}\text{C}$. The deep purple solution slowly turned red/orange as the solution was warmed from $-78\text{ }^{\circ}\text{C}$ to room temperature and stirred for 3 h. The solution was then quenched with deionized H₂O (7 mL), the organics were extracted with Et₂O and washed with deionized H₂O (3 × 50 mL), dried over MgSO₄, gravity filtered and concentrated *in vacuo*. The resulting residue was purified by flash chromatography (toluene, silica gel) to afford the resulting complex **3.9** as a purple/brown film. Yield = 0.15 g (31%). ¹H NMR (399.8 MHz, CDCl₃) δ 7.92 (dm, 2H, $J_{\text{HH}} = 8\text{ Hz}$, Aryl CH), 7.77 (dm, 4H, $J_{\text{HH}} = 8\text{ Hz}$, Aryl CH), 7.24 (dm, 2H, $J_{\text{HH}} = 8\text{ Hz}$, Aryl CH), 7.16 (dm, 4H, $J_{\text{HH}} = 8\text{ Hz}$, Aryl CH), 2.40 (s, 3H, CH₃), 2.38 (s, 6H, CH₃), -0.05 (s, 18H, CH₃). ¹¹B NMR (128.3 MHz, CDCl₃) δ -13.2 (s). ¹³C {¹H} NMR (101.6 MHz, CDCl₃) δ 152.6, 142.8, 139.2, 138.8, 131.0, 129.1, 128.3, 125.7, 125.3, 106.8, 77.2, 21.4, 21.3, -0.3 . FT-IR (ATR, cm⁻¹) 3035, 2957, 2923, 2897, 2857, 2132, 1605, 1505, 1351, 1260, 1247, 1209. UV-Vis (Toluene): $\lambda_{\max} = 317$ ($\epsilon = 25\,100\text{ M}^{-1}\text{ cm}^{-1}$), 515 nm ($\epsilon = 14\,200\text{ M}^{-1}\text{ cm}^{-1}$). ESI-HRMS (+ve mode) calculated for [C₃₂H₃₉BN₄Si₂]⁺: 546.2806, found 546.2770, difference: -6.5 ppm .

Acetylene Complex 3.10



In air, complex **3.9** (0.41 g, 0.74 mmol) was dissolved in warm MeOH (50 mL). K_2CO_3 (1.5 g, 11 mmol) was added and the solution was stirred at room temperature for 4 h. The solution was then concentrated *in vacuo* and the resulting residue was extracted with Et_2O and deionized H_2O (3×50 mL), dried over MgSO_4 , gravity filtered and concentrated *in vacuo*. The resulting residue was purified by flash chromatography (1:1 hexanes: CH_2Cl_2 , silica gel) to afford the resulting complex **3.10** as a purple film. Yield = 0.25 g (84%). ^1H NMR (399.8 MHz, CDCl_3) δ 7.97 (dm, 2H, $J_{\text{HH}} = 8$ Hz, Aryl CH), 7.76 (dm, 4H, $J_{\text{HH}} = 8$ Hz, Aryl CH), 7.27 (dm, 2H, $J_{\text{HH}} = 8$ Hz, Aryl CH), 7.23 (dm, 4H, $J_{\text{HH}} = 8$ Hz, Aryl CH), 2.41 (s, 3H, CH_3), 2.40 (s, 6H, CH_3), 2.22 (s, 2H, Alkyne CH). ^{11}B NMR (128.3 MHz, CDCl_3) δ -13.3 (s). $^{13}\text{C}\{^1\text{H}\}$ NMR (101.6 MHz, CDCl_3) δ 151.6, 143.0, 139.6, 139.0, 130.9, 129.3, 128.6, 125.5, 125.1, 88.1, 77.2, 21.4, 21.3. FT-IR (ATR, cm^{-1}) 3281, 3031, 2921, 2060, 1606, 1506, 1353, 1281, 1264, 1177. UV-Vis (Toluene): $\lambda_{\text{max}} = 317$ ($\epsilon = 24\,200\ \text{M}^{-1}\ \text{cm}^{-1}$), 524 nm ($\epsilon = 14\,400\ \text{M}^{-1}\ \text{cm}^{-1}$). ESI-HRMS (+ve mode) calculated for $[\text{C}_{26}\text{H}_{23}\text{BN}_4]^+$: 402.2016, found 402.2017, difference: +0.3 ppm.

Cycloaddition Complex 3.12



Under N_2 , N,N,N',N'',N''' -Pentamethyldiethylenetriamine (PMDETA) (3 μ L, 0.02 mmol) and CuI (3 mg, 0.02 mmol) were dissolved in dry THF (3 mL) and stirred for 30 min. The solution gradually changed from clear to pale yellow. Benzyl azide (58 μ L, 0.50 mmol) was added dropwise followed by complex **3.10** (62 mg, 0.2 mmol). The resulting purple solution was diluted with THF (7 mL) and stirred at 45 $^{\circ}$ C for 18 h. The solution was then cooled to room temperature, gravity filtered and the supernatant concentrated *in vacuo*. The resulting residue was purified by flash chromatography (CH_2Cl_2 , silica gel) to afford complex **3.12** as a purple film. Yield = 0.050 g (38%). 1H NMR (399.8 MHz, $CDCl_3$) δ 8.05 (dm, 2H, $J_{HH} = 8$ Hz, Aryl CH), 7.37–7.35 (m, 6H, Aryl CH), 7.31 (d, 2H, $J_{HH} = 8$ Hz, Aryl CH), 7.26–7.24 (m, 6H, Aryl CH and triazole CH), 7.07 (dm, 4H, $J_{HH} = 8$ Hz, Aryl CH), 6.97–6.94 (m, 4H, Aryl CH), 5.35 (s, 4H, Benzyl CH), 2.44 (s, 3H, CH_3), 2.32 (s, 6H, CH_3). ^{11}B NMR (128.3 MHz, $CDCl_3$) δ -6.0 (s). $^{13}C\{^1H\}$ NMR (101.6 MHz, $CDCl_3$) δ 153.8, 143.2, 139.4, 139.2, 136.4, 135.6, 130.7, 129.4, 129.2, 129.1, 128.4, 125.7, 125.5, 124.5, 77.2, 52.1, 21.4, 21.2. FT-IR (ATR, cm^{-1}) 3034, 2926, 2855, 1604, 1505, 1355, 1282, 1262, 1211, 954, 821. UV-Vis (Toluene): $\lambda_{max} = 295$ nm ($\epsilon = 29\,750$ $M^{-1} cm^{-1}$), 532 nm ($\epsilon = 13\,100$ $M^{-1} cm^{-1}$). ESI-HRMS (+ve mode) calculated for $[C_{40}H_{37}BN_{10}]^+$: 668.3296, found 668.3314, difference: +2.6 ppm.

3.5 References

1. Yang, H.; Zhou, Z.; Huang, K.; Yu, M.; Li, F.; Yi, T.; Huang, C. *Org. Lett.* **2007**, *9*, 4729–4732.
2. Li, M.; Guo, Z.; Zhu, W.; Marken, F.; James, T. D. *Chem. Commun.* **2015**, *51*, 1293–1296.

3. Baruah, M.; Qin, W.; Basaric, N.; De Borggraeve, W. M.; Boens, N. *J. Org. Chem.* **2005**, *70*, 4152–4157.
4. Dhokale, B.; Gautam, P.; Mobin, S. M.; Misra, R. *Dalton Trans.* **2013**, *42*, 1512–1518.
5. Ziessel, R.; Retailleau, P.; Elliott, K. J.; Harriman, A. *Chem. Eur. J.* **2009**, *15*, 10369–10374.
6. Yin, X.; Li, Y.; Li, Y.; Zhu, Y.; Tang, X.; Zheng, H.; Zhu, D. *Tetrahedron* **2009**, *65*, 8373–8377.
7. Haynes, W. M., CRC Handbook of Chemistry and Physics 96th Edition. Taylor & Francis Group: New York, **2015**.
8. Chang, M. C.; Otten, E. *Chem. Commun.* **2014**, *50*, 7431–7433.
9. Barbon, S. M.; Staroverov, V. N.; Gilroy, J. B. *Angew. Chem. Int. Ed.* **2017**, *129*, 8285–8289.
10. Gilroy, J. B.; Ferguson, M. J.; McDonald, R.; Patrick, B. O.; Hicks, R. G. *Chem. Commun.* **2007**, *2*, 126–128.
11. Prins, R. *Mol. Phys.* **1970**, *19*, 603–620.
12. Barbon, S. M.; Novoa, S.; Bender, D.; Groom, H.; Luyt, L. G.; Gilroy, J. B. *Org. Chem. Front.* **2017**, *4*, 178–190.
13. Bruker-AXS, *SAINT* version 2013.8, **2013**, Bruker-AXS, Madison, WI, 53711, USA.
14. Bruker-AXS, *SADABS* version 2012.1, **2012**, Bruker-AXS, Madison, WI 53711, USA.
15. Sheldrick, G. M. *Acta. Cryst.* **2015**, *A71*, 3–8.
16. Sheldrick, G. M. *Acta. Cryst.* **2015**, *C71*, 3–8.
17. Macrae, C. F.; Bruno, I. J.; Chisholm, J. A.; Edgington, P. R.; McCabe, P.; Pidcock, E.; Rodriguez-Monge, L.; Taylor, R.; van de Streek, J.; Wood, P. A. *J. Appl. Cryst.* **2008**, *41*, 466–470.

Chapter 4

4.1 Conclusions

The work included in this thesis describes the synthesis and characterization of the first alkynyl-substituted boron formazanate complexes. This work began by synthesizing a tri-*p*-tolyl BF₂ formazanate (**2.7**) from the parent formazan (**2.6**) by heating overnight at 80 °C in a toluene solution containing excess BF₃•OEt₂ and NEt₃ under inert atmosphere. The alkynyl-substituted boron formazanate complexes were then synthesized using 2.2 equiv. of the corresponding lithiated terminal acetylenes to afford the final complexes **2.8–2.10** in 17–35% yields. In each case, formation of these complexes was accompanied by a disappearance of the 1:2:1 triplet and appearance of a broad singlet in the ¹¹B NMR spectrum. IR spectra confirmed the presence of an internal alkyne functionality at roughly 2186 cm⁻¹. X-ray crystallography revealed that the parent complex **2.7** was relatively planar, with the boron atom displaced from the plane of the formazanate backbone by 0.094 Å, while the boron atom of **2.8** was further displaced by 0.713 Å. Significant twisting of the 1,5-aryl substituents with respect to the formazanate backbone was also observed in complex **2.8**, which existed in a ‘dragonfly’ conformation. UV-Visible absorption spectra of compounds **2.7–2.10** revealed strong π→π* transitions in both 317–320 and 519–532 nm regions, with λ_{max} values of complexes **2.8–2.10** exhibiting a blue-shift of 11–13 nm relative to the parent complex **2.7**. None of the alkynyl-substituted complexes exhibited any detectable photoluminescence, which was attributed to the non-radiative vibrational and rotational decay pathways relating to the 3-phenyl substituent. Compounds **2.7–2.10** were found to be redox active and possessed two ligand-centred reversible (or quasi-reversible) one-electron reduction waves yielding a radical anion and dianion. One ligand-centred reversible (or quasi-reversible) one-electron oxidation was also observed for each compound, yielding a radical cation. It was found that **2.8–2.10** were more difficult to reduce and easier to oxidize with no fluorine atoms present. **2.10** was found to be the easiest to reduce as a result of the electron withdrawing CF₃ substituent at the *para* position of the substituted phenylacetylene. **2.9** was found to be the most difficult to reduce as a result of the electron donating OMe substituent at the *para* position of the substituted phenylacetylene.

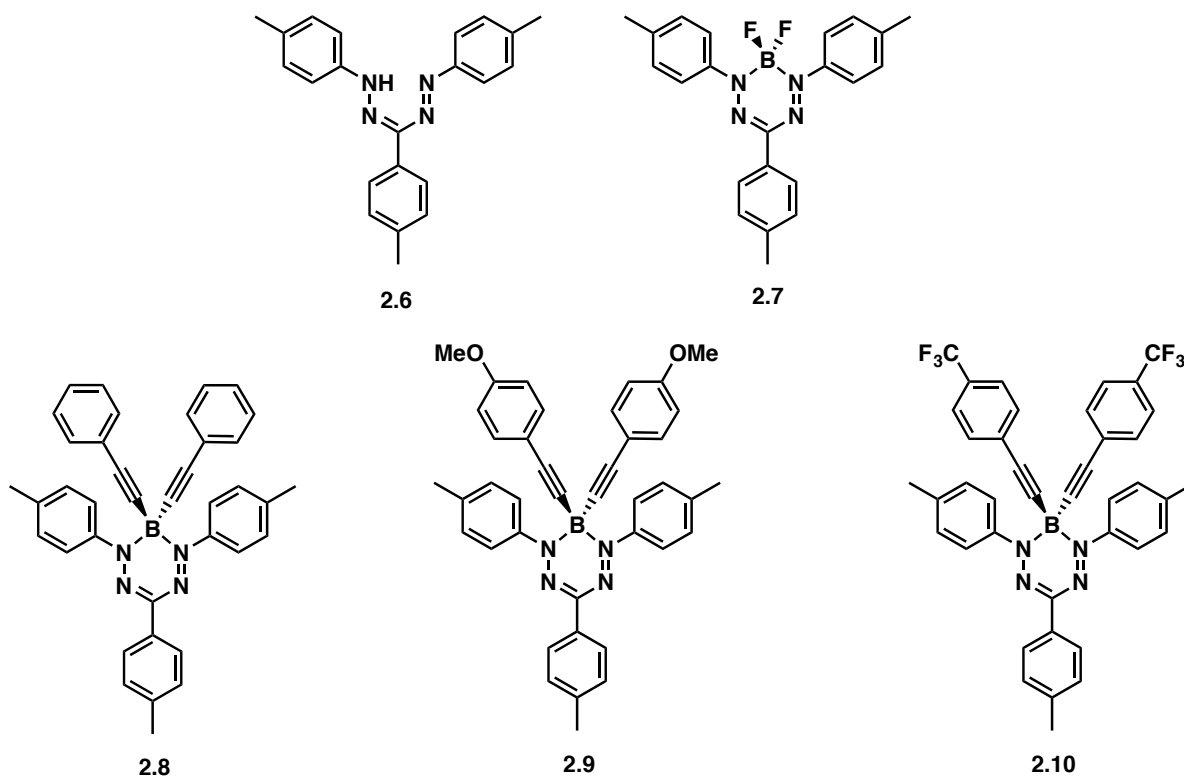


Figure 4.1. Formazanate and boron formazanate complexes studied in Chapter 2.

Chapter 3 focused on the incorporation of a redox-active alkynyl-substituted boron formazanate complex, and explored the chemical oxidation and reduction of the system. Post-synthetic modification of the boron formazanate scaffold was also explored using the alkynyl functionality as a handle for CuAAC chemistry. This chapter began by synthesizing the neutral ferrocene complex **3.5** using the previously described lithiation procedure. Formation of this complex was accompanied by a disappearance of the 1:2:1 triplet and appearance of a broad singlet in the ^{11}B NMR spectrum. IR spectroscopy confirmed the presence of an internal alkyne functionality at 2188 cm^{-1} . X-ray crystallography revealed that the boron atom was significantly displaced from the backbone of the formazanate backbone by 0.755 \AA , more so than the boron atoms of both the parent BF_2 complex **2.7** as well as the phenylacetylene complex **2.8**. More significant twisting of the 1,5-aryl substituents relative to the formazanate backbone was also observed in complex **3.5**, with dihedral angles of 66.9° and 67.9° compared to 54.9° and 60.6° of complex **2.8**, likely due to the increased steric effect of the ferrocene

substituents. Complex **3.5** was found to be redox-active and exhibited two ligand-centred reversible (or quasi-reversible) one-electron reduction waves yielding a radical anion and dianion. One ligand-centred quasi-reversible one-electron oxidation was also observed, with a second reversible oxidation event corresponding to the ferrocene substituents. Interestingly, this oxidation wave was attributed as a two \times one-electron process. The coincidence or near coincidence of the waves indicated that there is little or no communication between the two ferrocene substituents through the boron atom, as both ferrocene moieties oxidize at the same (or nearly the same) potential. Based on the information obtained from the cyclic voltammograms, appropriate oxidants and reductants were selected in order to probe the chemically reduced and oxidized forms of the ferrocene complex **3.5**. CoCp^*_2 was selected to reduce the ferrocene complex, while tris(4-bromophenyl)ammoniumyl hexachloroantimonate (magic blue) was used as the oxidant. In order to provide an accurate basis for comparison, phenylacetylene complex **2.8** was also reduced using CoCp_2 . UV-Vis absorption data revealed that upon reduction with CoCp^*_2 , the UV trace of **3.6** closely matched that of the reduced phenylacetylene complex as well as previously published reports, providing evidence for a singly reduced formazanate backbone. Further supporting the presence of radical complex **3.6** was a broad, featureless EPR signal at $g = 2.0035$. Upon oxidation of the neutral ferrocene complex, **3.8** exhibited a red-shift of 40 nm in the $\pi \rightarrow \pi^*$ region from 501 to 541 nm. Furthermore, complex **3.8** did not produce a signal in the EPR spectrum, as ferrocenium is generally not detectable above 77 K.

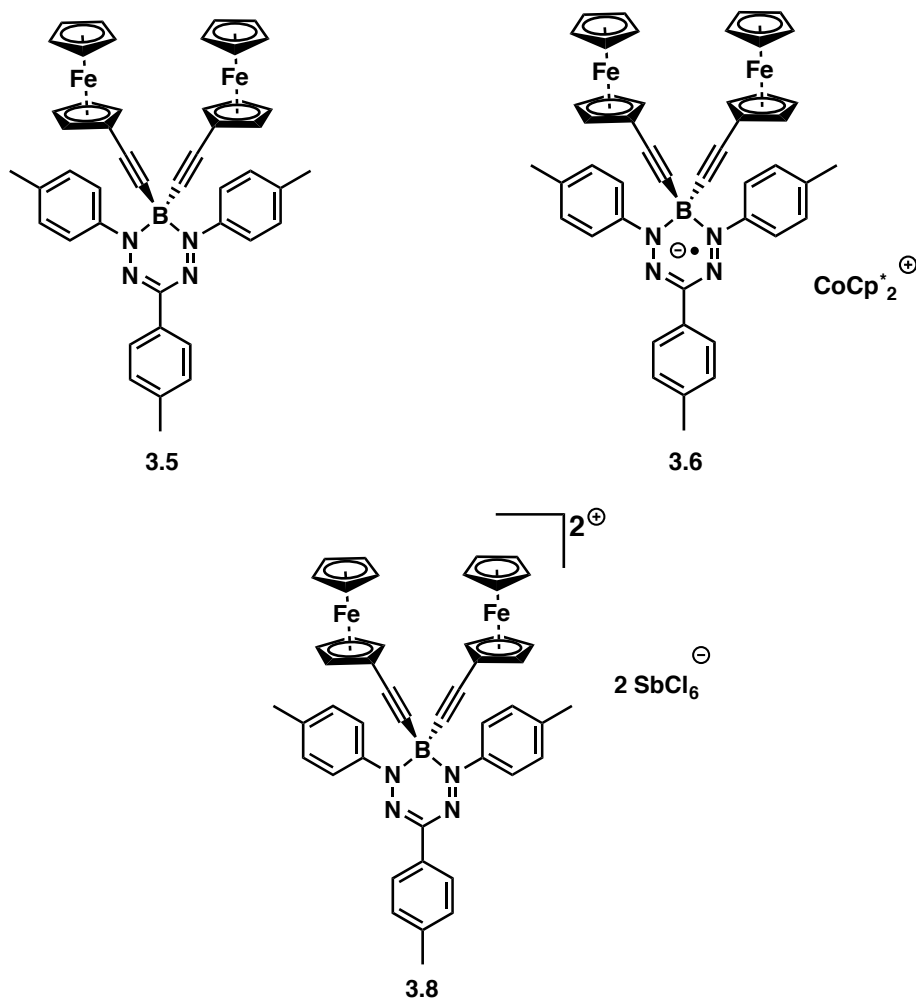
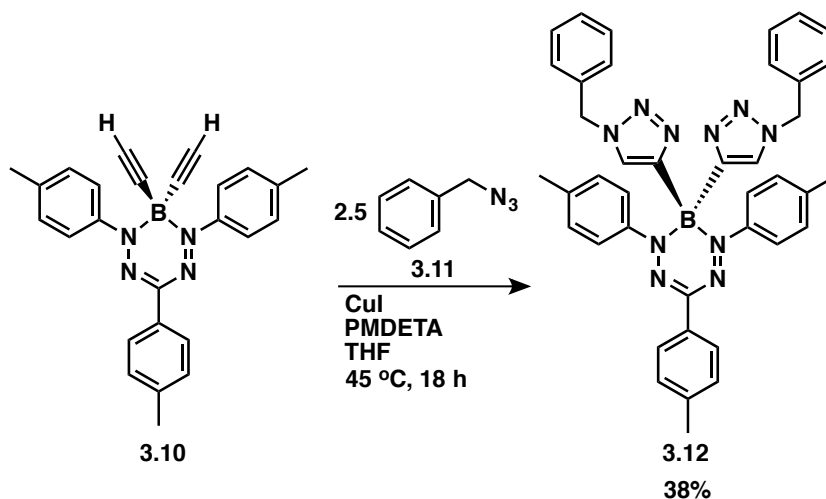


Figure 4.2. Ferrocene complexes studied in Chapter 3.

CuAAC chemistry was explored using terminal acetylenes at the boron centre in order to further expand the scope of boron formazanate chemistry (Scheme 4.1). As a proof of concept, benzyl azide was used as a model reactant for the CuAAC reaction with complex **3.10** to afford the cycloaddition product **3.12** in a 38% yield. ^1H NMR confirmed the disappearance of the terminal acetylene protons at 2.23 ppm and the appearance of the diagnostic benzyl protons at 5.36 ppm as well as the proton signal corresponding to the triazole rings at 8.07 ppm. IR spectroscopy confirmed formation of the cycloaddition product as the terminal acetylene stretch at 2060 cm^{-1} of complex **3.10** disappeared. UV-Vis absorption data revealed a slight red shift in the $\pi\rightarrow\pi^*$ region

from 524 to 532 nm, consistent with other reports for similar cycloaddition complexes of BF_2 formazanate systems.



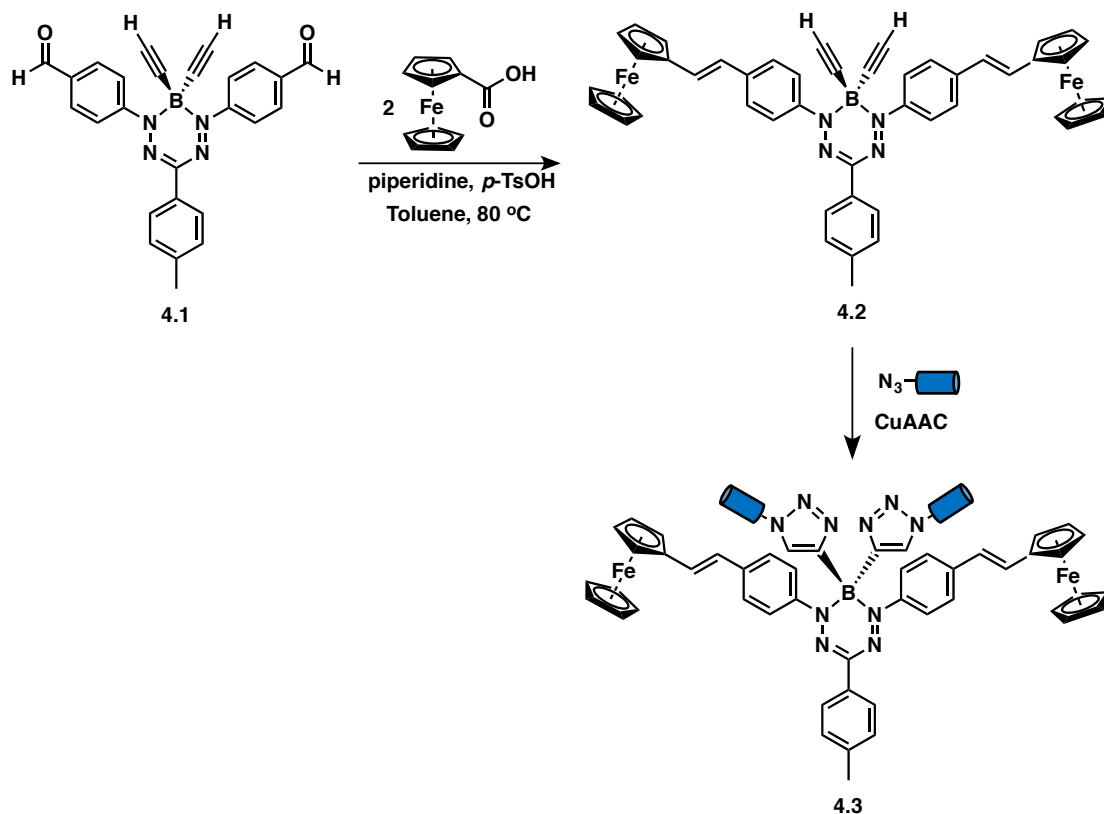
Scheme 4.1. CuAAC chemistry studied in Chapter 3.

In conclusion, a new family of dyes has been synthesized which exploit chemistry at the boron atom of the boron formazanate scaffold. While the impact of electron withdrawing and electron donating substituents don't play a significant role in altering the spectroscopic properties of these complexes, it has been demonstrated that new functionalities can be introduced. This new functionality provides a broader scope of possible reactions that may be explored, and as a result, broaden the scope of possible applications for these dyes.

4.2 Future Work

Taking advantage of chemistry at the boron centre will hopefully allow these molecular systems to find more widespread use in applications. For example, using CuAAC chemistry in order to append the boron formazanate scaffold to other materials through the boron atom instead of through the *N*-aryl substituents would allow for the introduction of functionality at the *N*-aryl positions that would otherwise not be possible. Conjugated ferrocene-containing boron formazanates may exhibit unique electrochromism and provide a handle for sensing. While using the boron atom for

CuAAC chemistry, it may be possible to use the Knoevenagel condensation in order to install conjugated ferrocene units to the *N*-aryl substituents of the formazanate backbone (Scheme 4.2).

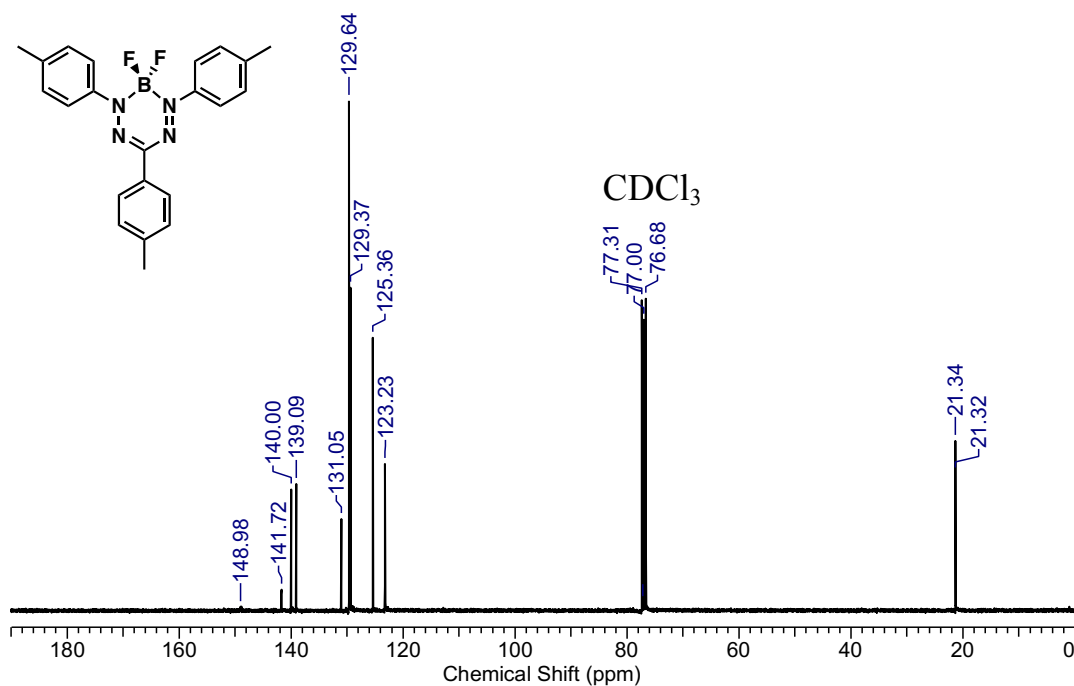
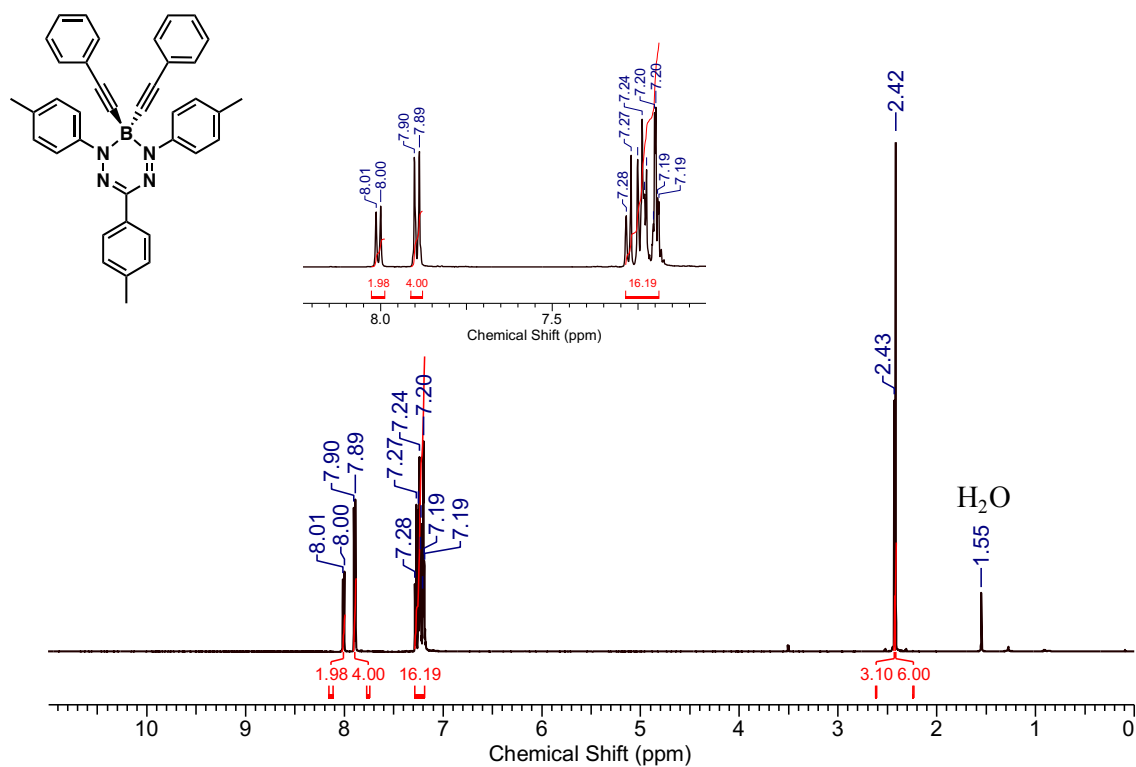


Scheme 4.2. Proposed Knoevenagel condensation and CuAAC toward the synthesis of multifunctional ethynyl-substituted boron formazanate complexes.

The benefit of this molecular system is that the ferrocene units are conjugated to the formazanate backbone and will have a greater impact on the electronics of the system in contrast with ferrocene units at the boron atom. This will greatly affect the spectroscopic properties of the complex upon oxidation (or reduction), while the non-conjugated portion of the scaffold at the boron atom may be used to tether this scaffold to materials, as demonstrated with the cartoon in Scheme 4.2.

Appendices

Appendix A – Supporting Information for Chapter 2

Figure A1.1. $^{13}\text{C}\{^1\text{H}\}$ NMR spectrum of 2.7 in CDCl_3 .Figure A1.2. ^1H NMR spectrum of 2.8 in CDCl_3 .

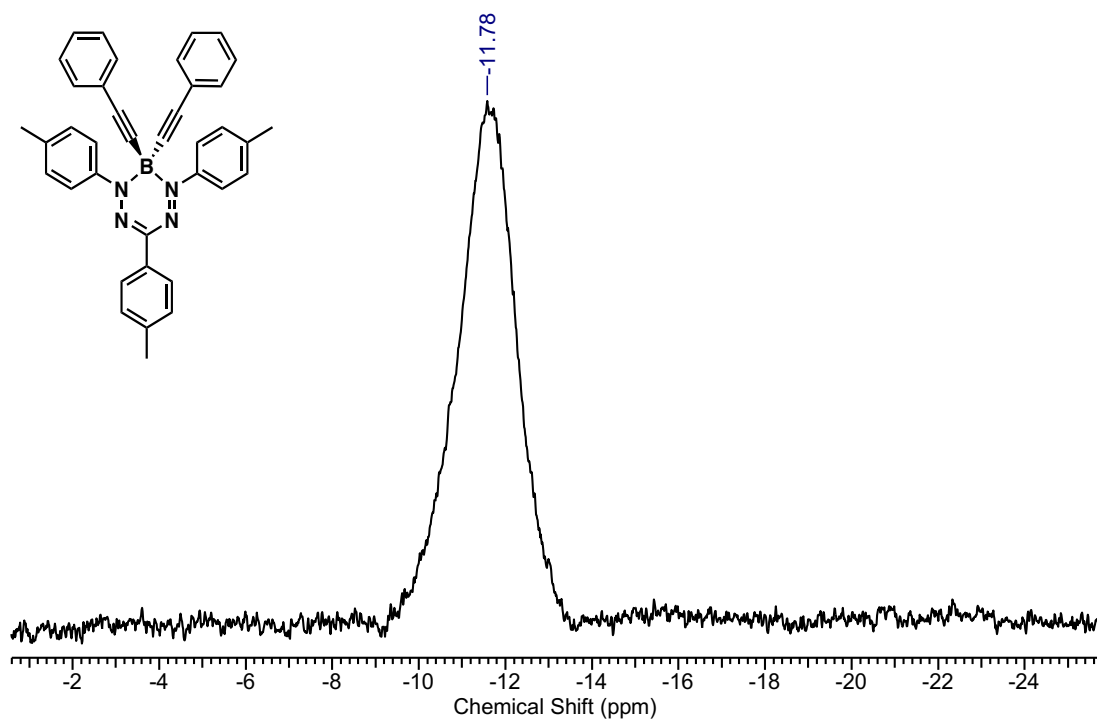


Figure A1.3. ^{11}B NMR spectrum of **2.8** in CDCl_3 .

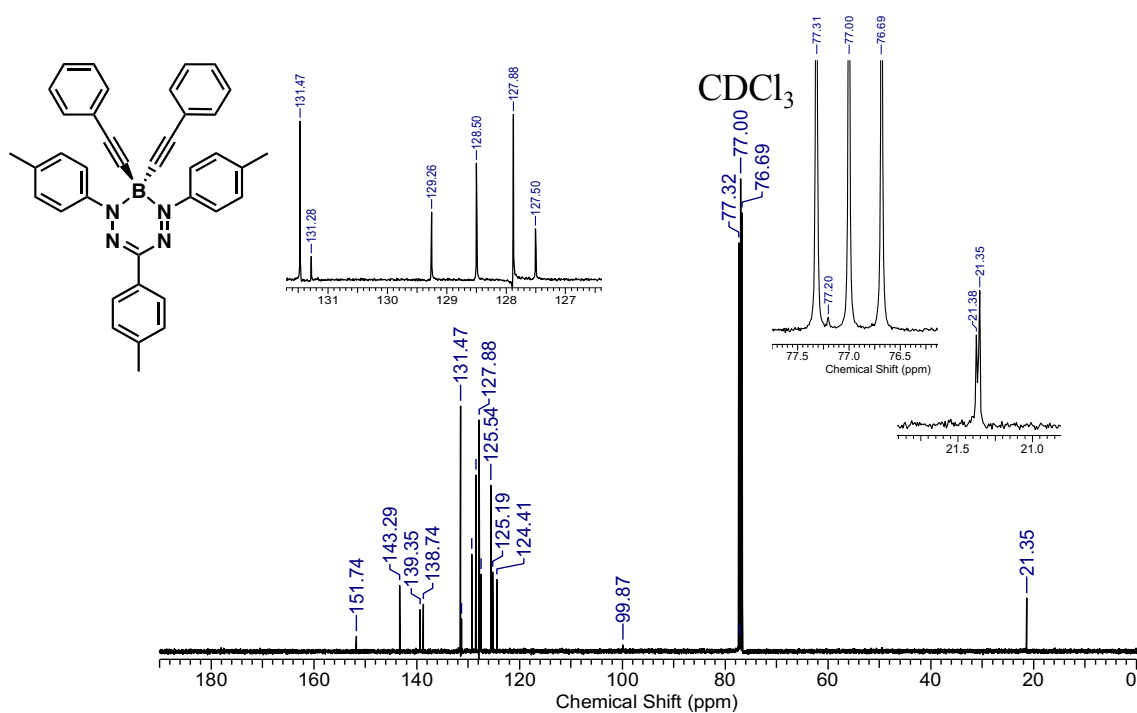


Figure A1.4. $^{13}\text{C}\{^1\text{H}\}$ NMR spectrum of **2.8** in CDCl_3 .

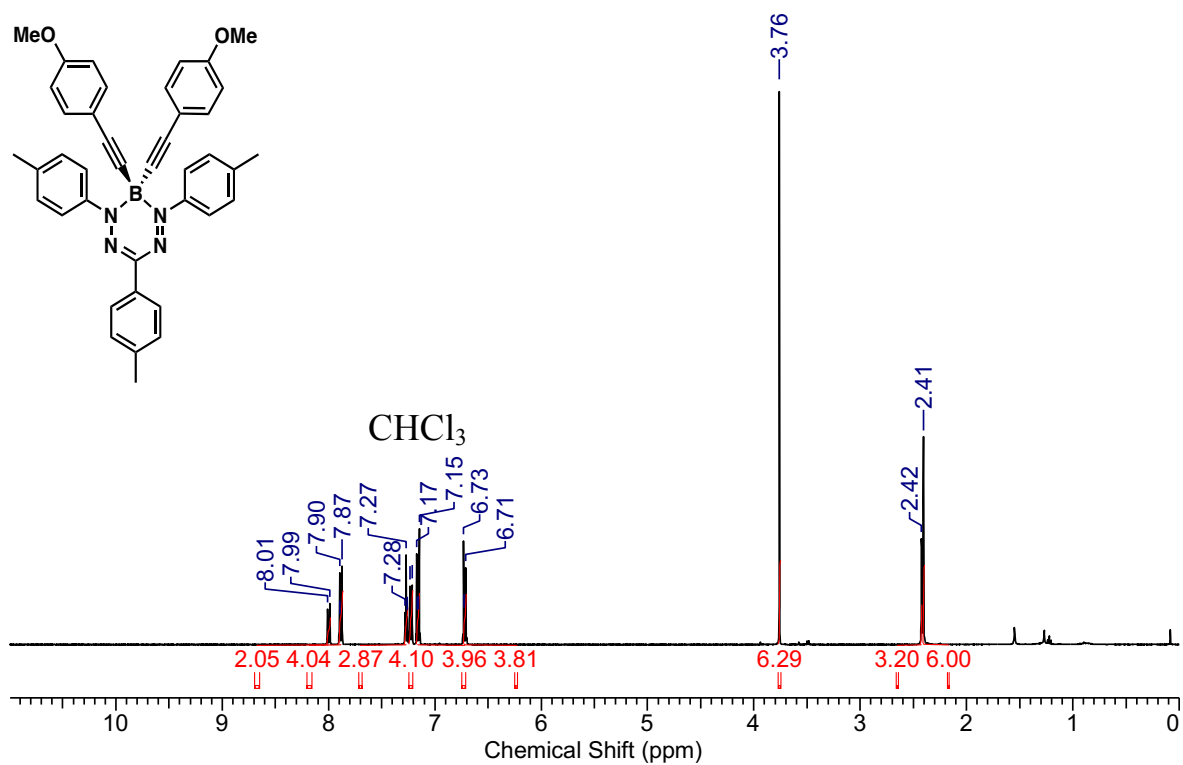


Figure A1.5. ^1H NMR spectrum of **2.9** in CDCl_3 .

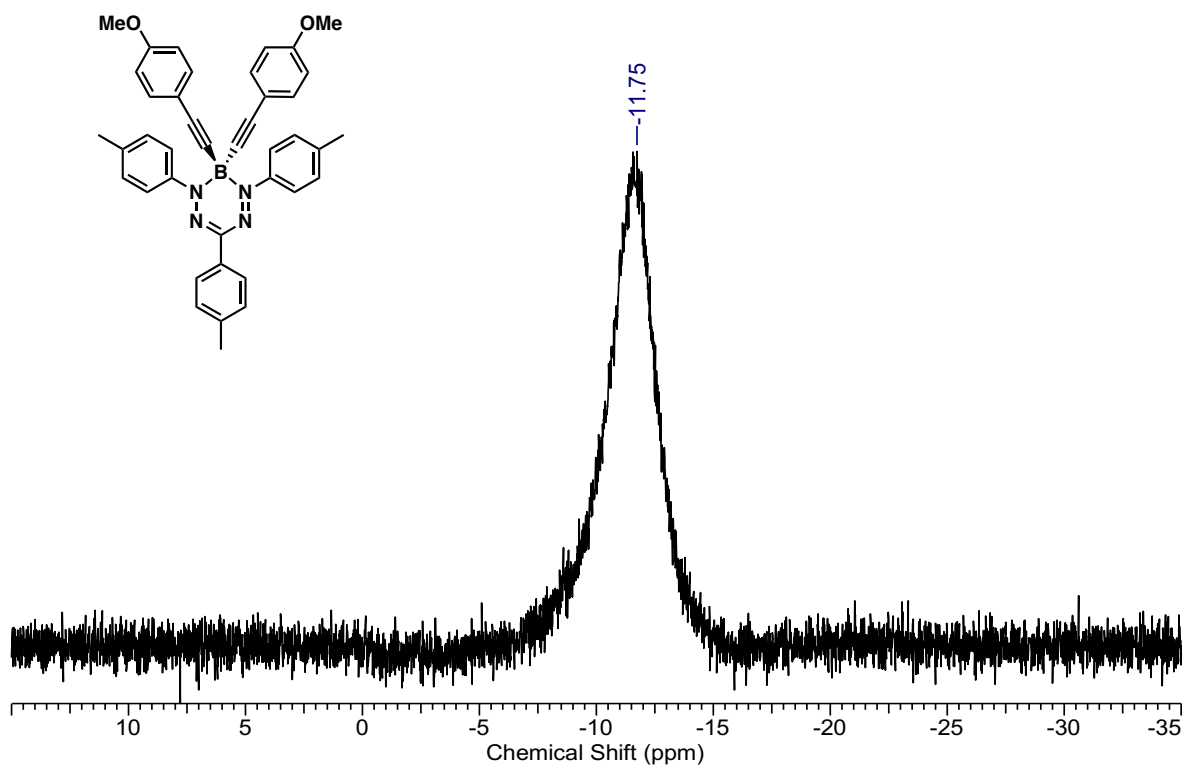


Figure A1.6. ^{11}B NMR spectrum of **2.9** in CDCl_3 .

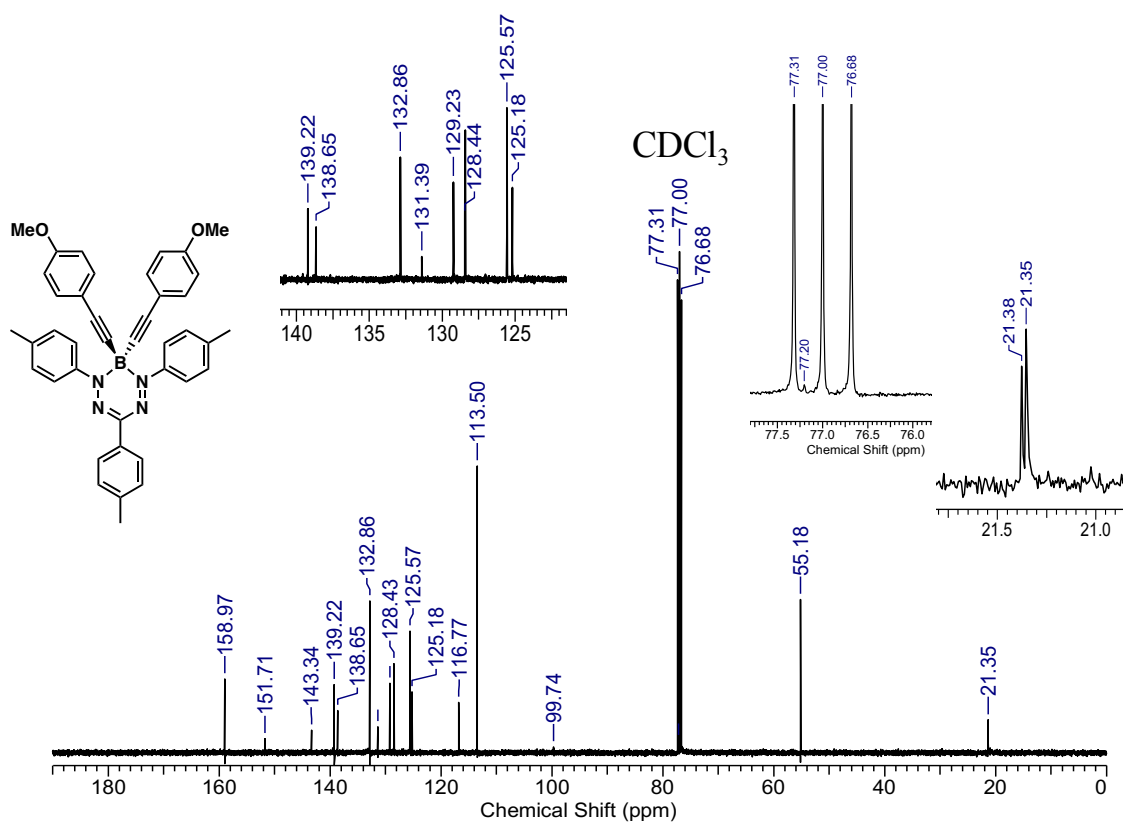


Figure A1.7. $^{13}\text{C}\{^1\text{H}\}$ NMR spectrum of **2.9** in CDCl_3 .

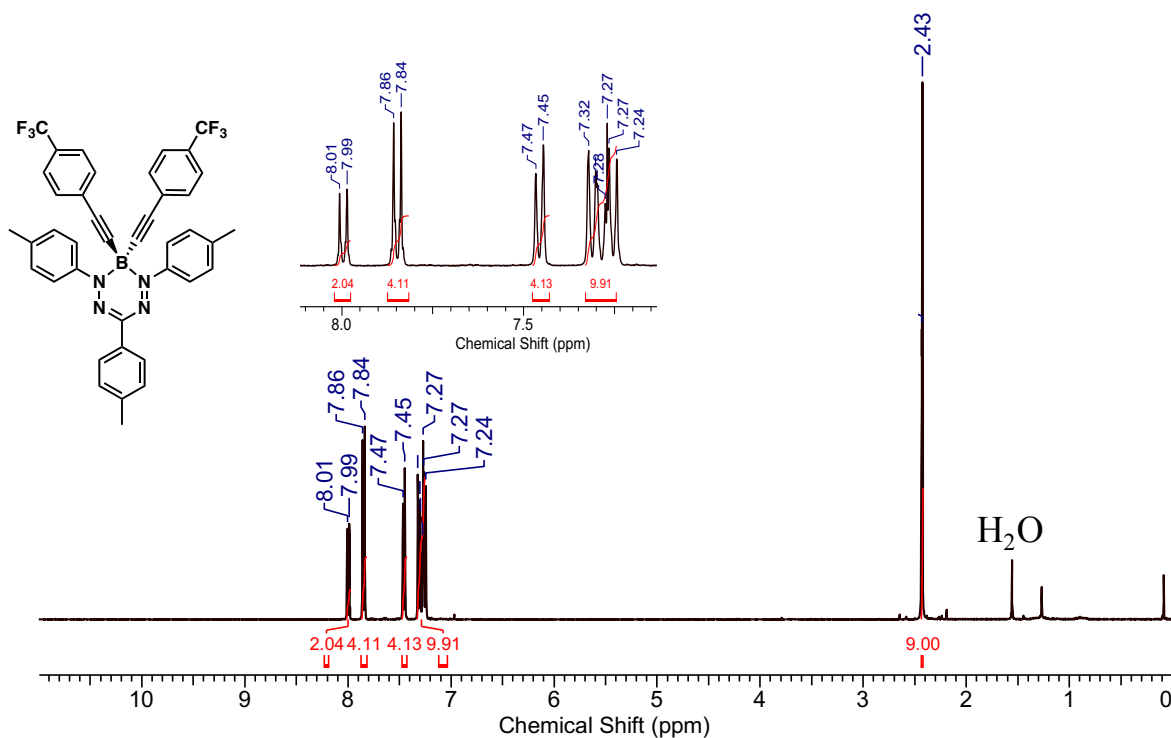


Figure A1.8. ^1H NMR spectrum of **2.10** in CDCl_3 .

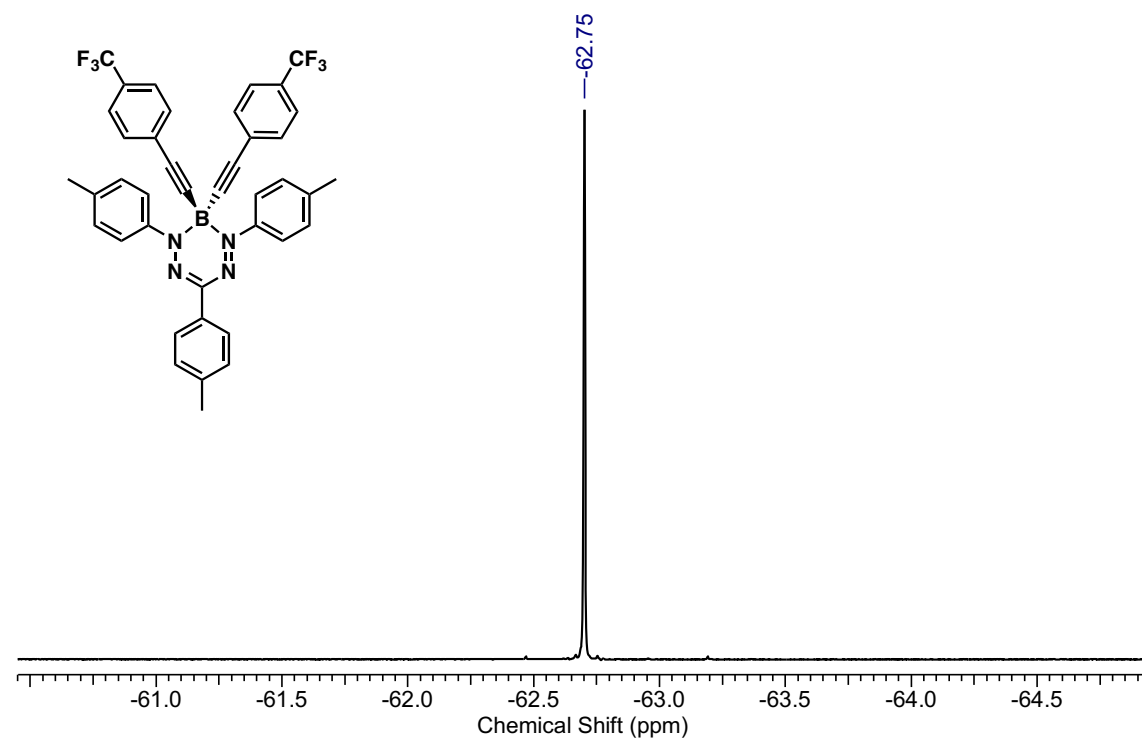


Figure A1.9. ^{19}F NMR spectrum of **2.10** in CDCl_3 .

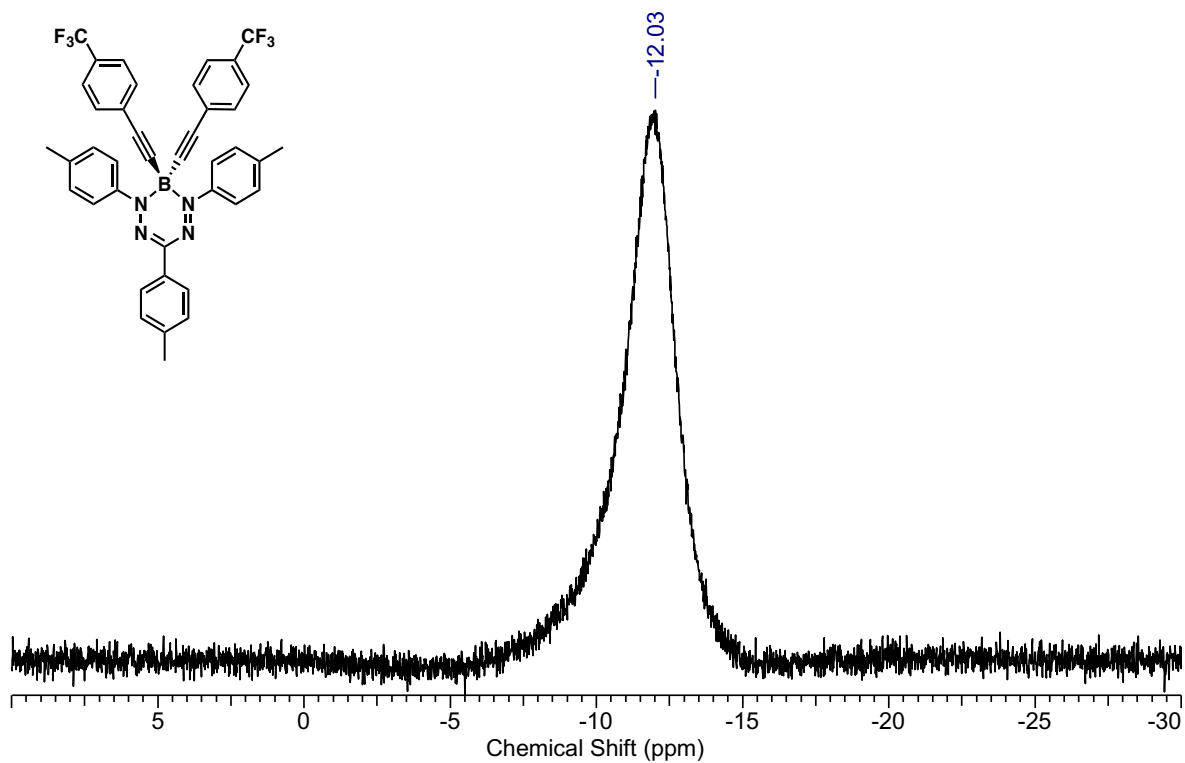


Figure A1.10. ^{11}B NMR spectrum of **2.10** in CDCl_3 .

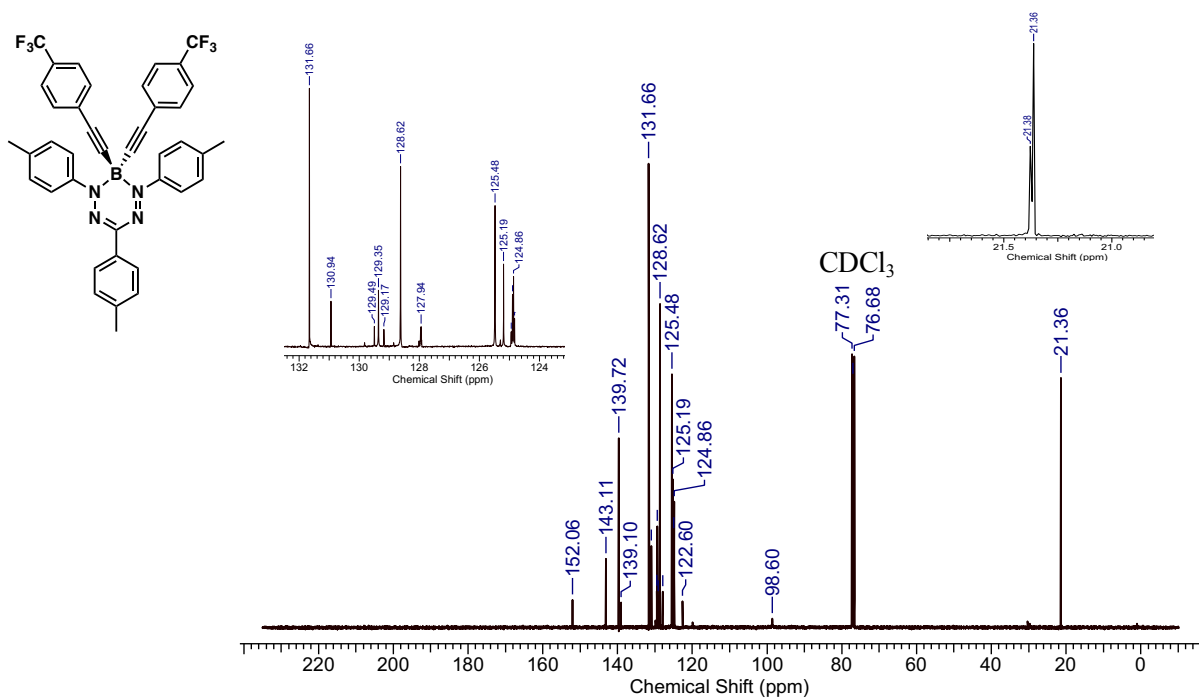


Figure A1.11. $^{13}\text{C}\{^1\text{H}\}$ NMR spectrum of **2.10** in CDCl_3 .

Appendix B – Supporting Information for Chapter 3

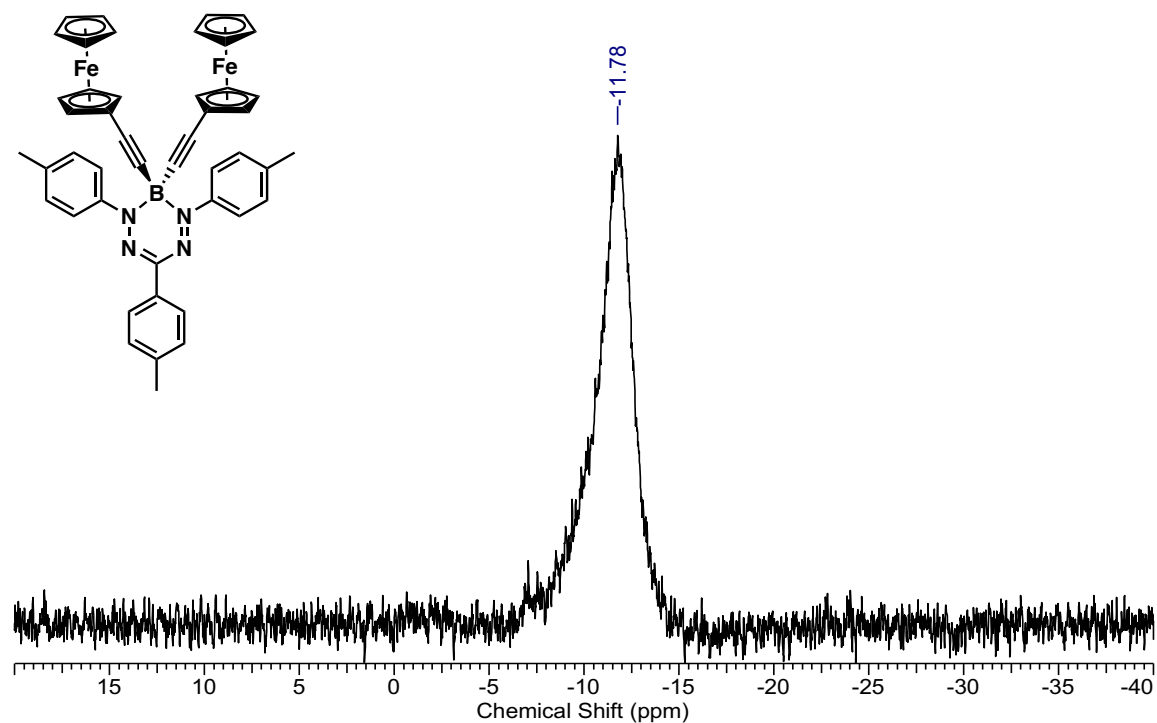
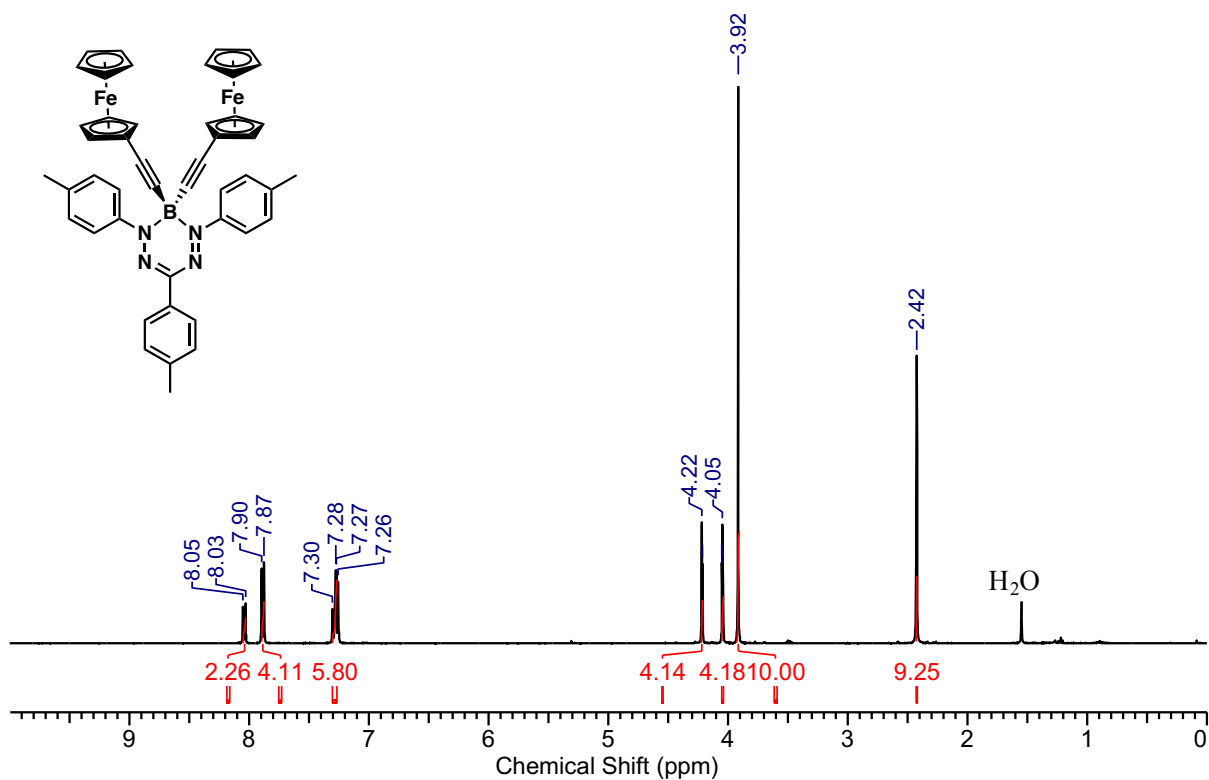
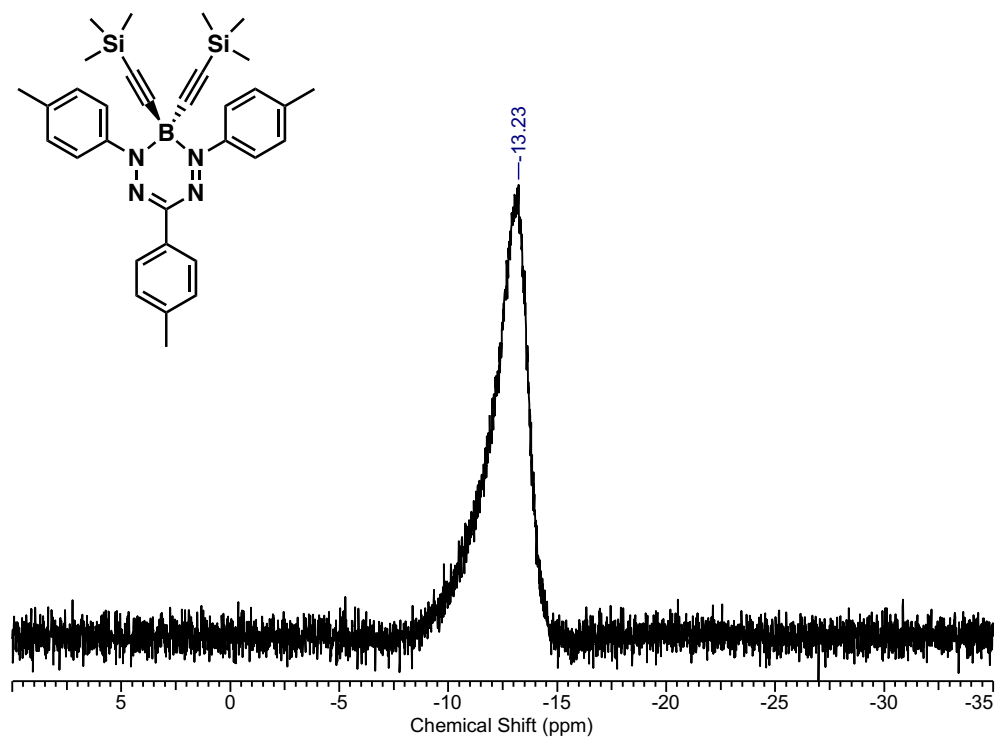
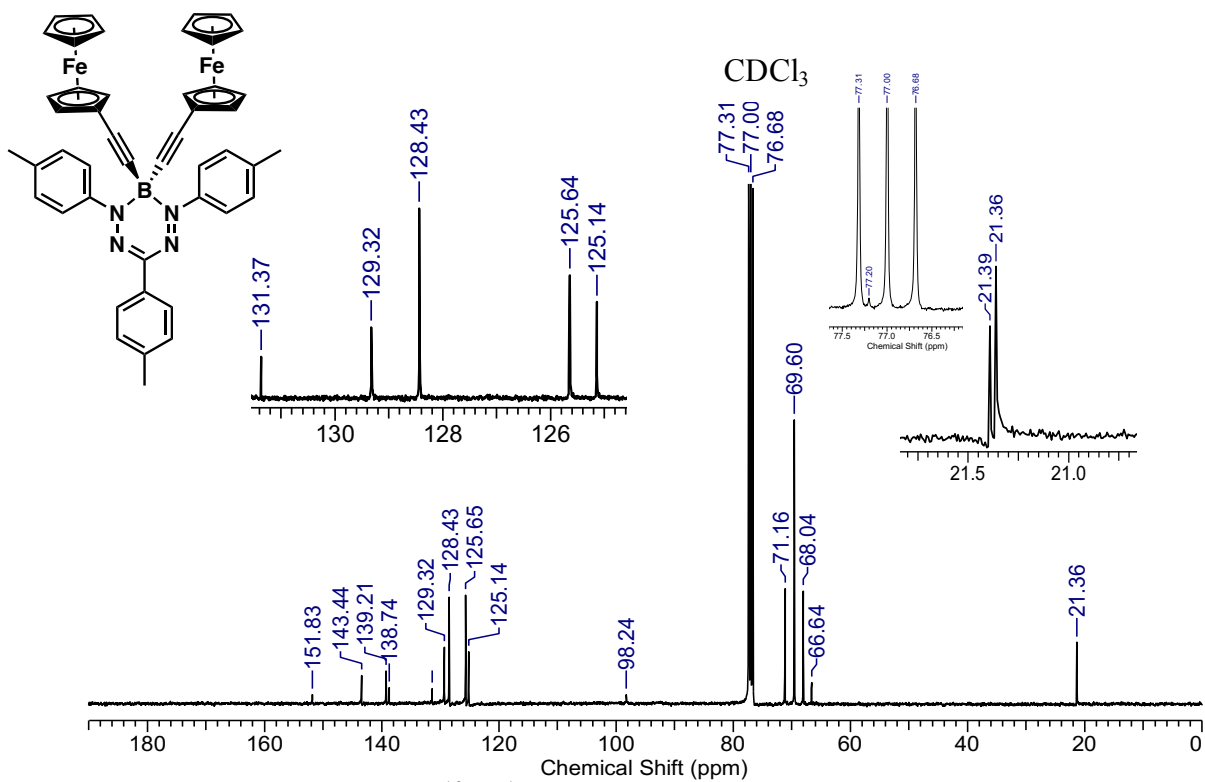


Figure B2. ^{11}B NMR spectrum of **3.5** in CDCl_3 .



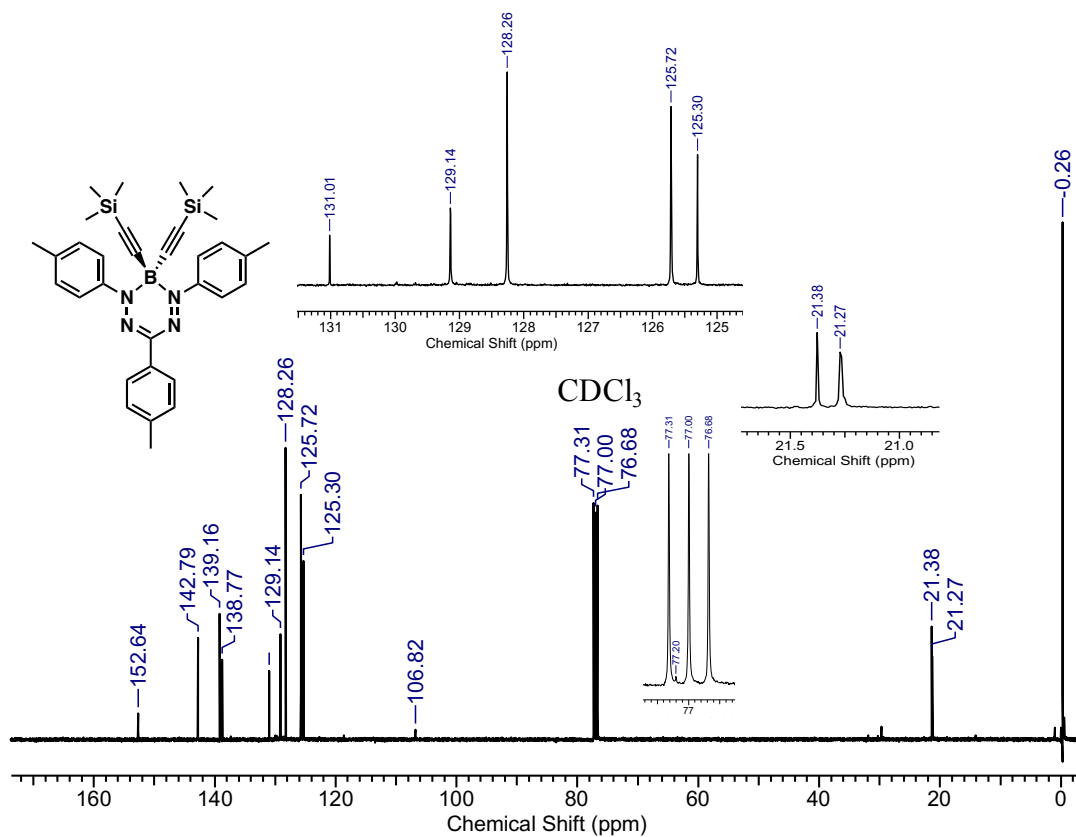


Figure B5. $^{13}\text{C}\{^1\text{H}\}$ spectrum of **3.9** in CDCl_3 .

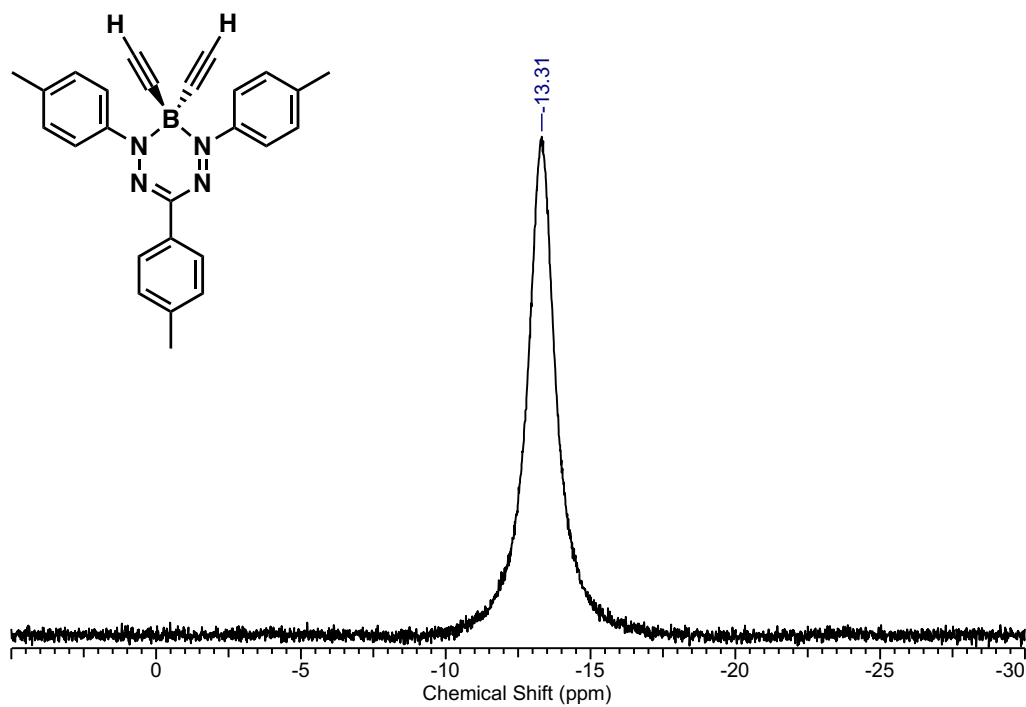


Figure B6. ^{11}B NMR spectrum of **3.10** in CDCl_3 .

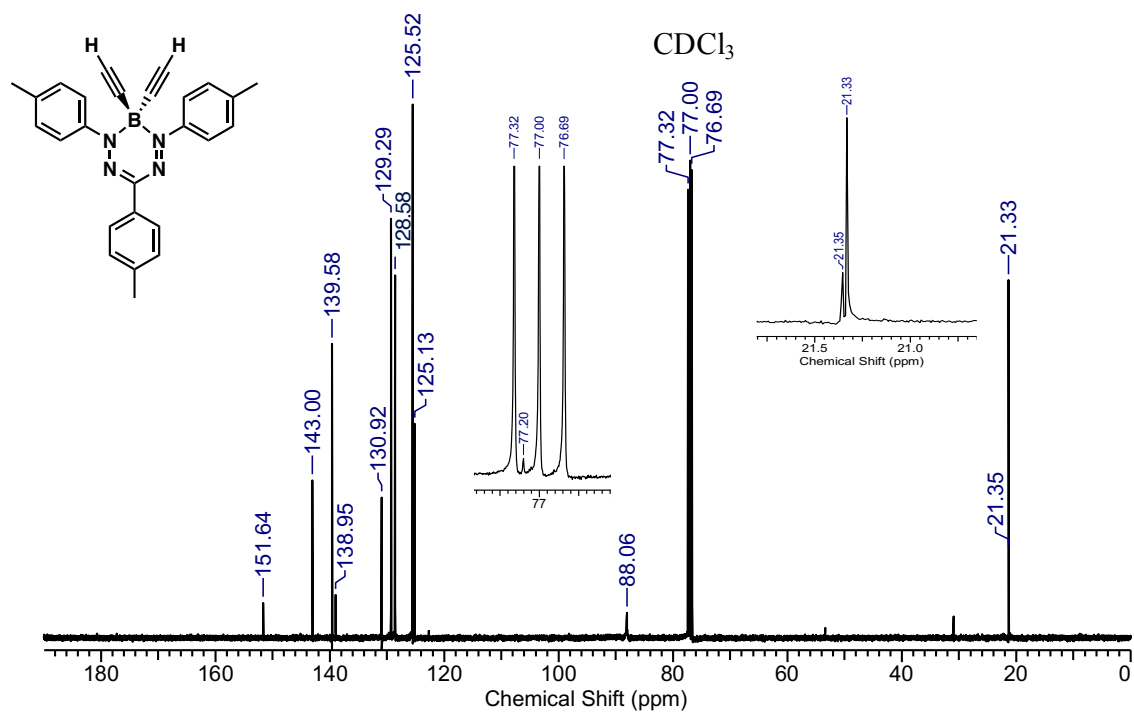


Figure B7. ¹³C {¹H} NMR spectrum of **3.10** in CDCl₃.

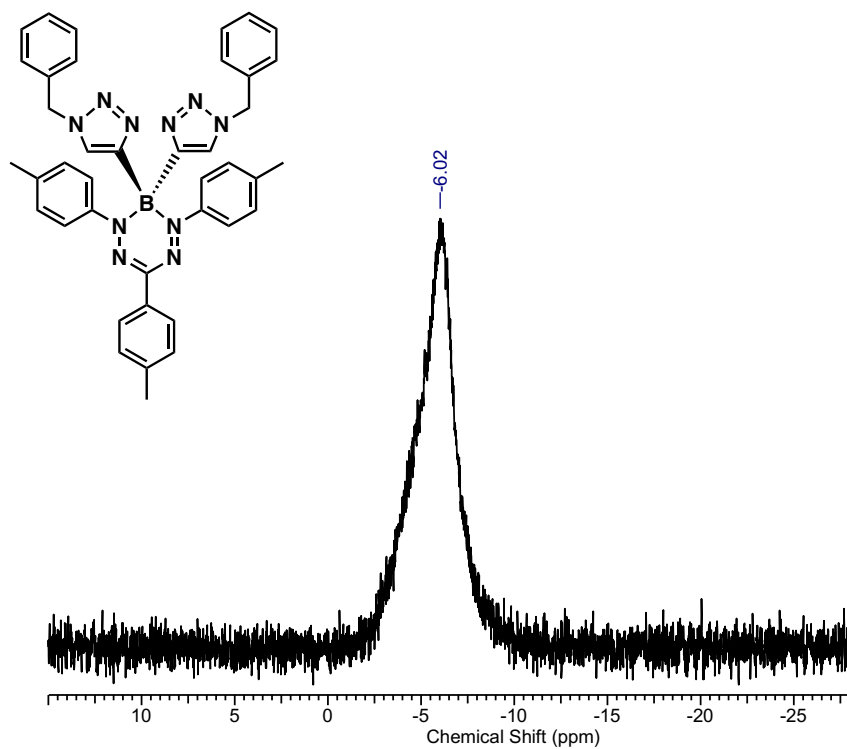


Figure B8. ¹¹B NMR spectrum of **3.12** in CDCl₃.

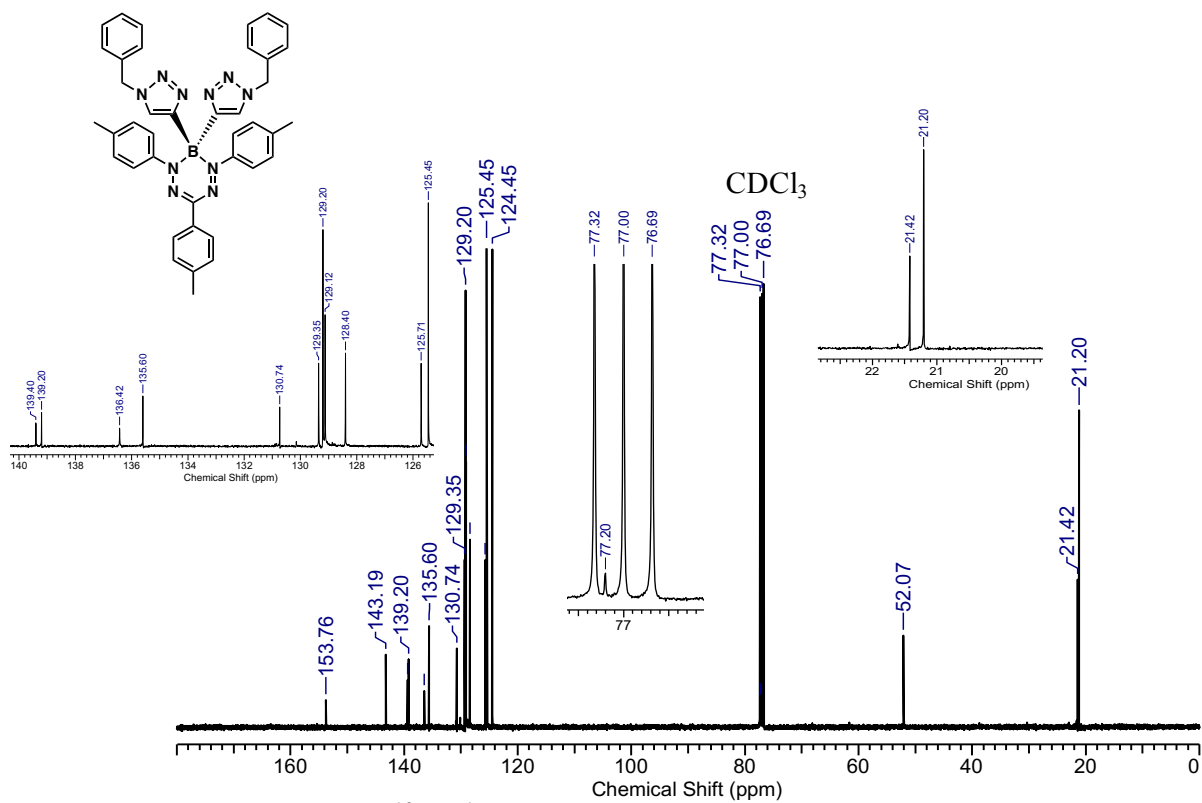


Figure B9. ^{13}C $\{^1\text{H}\}$ NMR spectrum of **3.12** in CDCl_3 .

Curriculum Vitae

Post-Secondary Education – The University of Western Ontario

M.Sc. (Chemistry) September 2016 – Present

B.Sc. – Honours Specialization in Chemistry – Awarded April 2016

Publications

1. Wu, L.; Guo, D.; Van Belois, A.; Noël, J.; Keech, P.; Wren, J. C.* *Corros. Sci.*, *Submitted*.

Work Experience

TA duties: 2213A, 2223B, 2273A, 2283B

Research Experience

Undergraduate Research Thesis Course – 09/2015 to 04/2016

- Supervisor: Dr. Mark Workentin

Undergraduate Research Assistant – 01/2015 to 09/2015

- Supervisor: Dr. Clara Wren

Presentations (Presenting author underlined)

1. Poster Presentation (International): Van Belois, A.; Workentin, M.S.; Gilroy, J.B. *Boron Adducts of Formazanate Ligands*. 36th Chemistry Graduate Student Symposium, Buffalo, NY, USA, May 21 – 23, 2018.
 - Awarded 1st place prize
2. Poster Presentation (International): Van Belois, A.; Workentin, M.S.; Gilroy, J.B. *Boron Adducts of Formazanate Ligands*. 45th Ontario-Quebec Physical Organic Mini-Symposium, Waterloo, ON, Canada, November 10 – 12, 2017.
3. Poster Presentation (International): Van Belois, A.; Workentin, M.S.; Gilroy, J.B. *Towards the Development of Novel Boron-Substituted Formazanate Dyes*, 100th Conference for the Canadian Society for Chemistry, Toronto, ON, Canada, May 28 – June 1, 2017.

4. Oral Presentation (International): Luo, W.; Gobbo, P.; Gunawardene, P.; Van Belois, A.; McNitt, C.; Sutton, D.; Popik, V. V.; Workentin, M.S. *Design and Synthesis of Functional Bioorthogonal Nanomaterials*, 100th Conference for the Canadian Society for Chemistry, Toronto, ON, Canada, May 28 – June 1, 2017.
5. Oral Presentation (International): Wu, L.; Guo, D.; Van Belois, A.; Noël, J.; Keech, P.; Wren, J. C. *Radiolysis-assisted Corrosion of Carbon-Steel Nuclear-Waste Containers at Near-Weld Region*, 17th International Conference on Environmental Degradation of Materials in Nuclear Power Systems – Water Reactors, Ottawa, ON, Canada, August 9 – 13, 2015.

Course Work

- Fall 2016: Chem 9503R – NMR I (88)
- Winter 2017: Chem 9653S – Polymer I (89)
Chem 9651T – Organometallics (90)
- Fall 2017: Chem 9507Q – Chemical Communications (92)

Volunteer Work

Let's Talk Science Outreach Program – 2017 – Present

Western University Outreach Program – 2017 – Present